12-2020

Design of Power Receiving Units for 6.78MHz Wireless Power Transfer Systems

Hoang Phuc Tran Pham
ppham3@vols.utk.edu

To the Graduate Council:

I am submitting herewith a thesis written by Hoang Phuc Tran Pham entitled "Design of Power Receiving Units for 6.78MHz Wireless Power Transfer Systems." I have examined the final electronic copy of this thesis for form and content and recommend that it be accepted in partial fulfillment of the requirements for the degree of Master of Science, with a major in Electrical Engineering.

Daniel Costinett, Major Professor

We have read this thesis and recommend its acceptance:

Daniel Costinett, Leon Tolbert, Bai Hua

Accepted for the Council:
Dixie L. Thompson

Vice Provost and Dean of the Graduate School

(Original signatures are on file with official student records.)

Design of Power Receiving Units for 6.78MHz Wireless Power Transfer Systems

A Thesis Presented for the

Master of Science Degree

The University of Tennessee, Knoxville

Phuc Tran Hoang Pham

December 2020

ACKNOWLEDGMENTS

I would like to express my highest gratitude to Dr. Daniel Costinett and Dr. Leon Tolbert, for their professional advice, engineering knowledge, and guidance throughout my graduate study. I also want to give a special appreciation to my family for supporting me unconditionally. I am grateful to work on the PowerAmerica project with a team of most talented graduate students Jie Li, Jinging Sun, and Spencer Cochran. Thanks to your priceless mentorship and willingness to answer my questions, even at late night.

I also want to extend my gratitude to my friends, who are always on my side. Thanks to Thao Tran, Phuong Bui, and Khoa Dang for all the laughs and continued friendship. Special thanks to my friend and teammate Quillen Blalock for his hard work, personal advice, and laughing at my horrible jokes.

ABSTRACT

In the last decade, the wireless power transfer (WPT) technology has been a popular topic in power electronics research and increasingly adopted by consumers. The AirFuel WPT standard utilizes resonant coils to transfer energy at 6.78 MHz, introducing many benefits such as longer charging distance, multi-device charging, and high tolerance of the coil misalignment. However, variations in coil coupling due to the change in receiving coil positions alter the equivalent load reactance, degrading efficiency.

In recent studies, active full-bridge rectifiers are employed on WPT receivers because of their superior efficiency, controllability, and ability to compensate for detuned WPT networks. In order to take advantage of those characteristics, the rectifier switching actions must be synchronized with the magnetic field. In the literature, existing solutions for synchronizing the active rectifier in WPT systems are mostly not reliable and bulky, which is not suitable for small receivers. Therefore, a frequency synchronous rectifier with compact on-board control is proposed in this thesis. The rectifier power stage is designed to deliver 40 W to the load while achieving full zero-voltage switching to minimize the loss. The inherent feedback from the power stage dynamics to the sensed signal is analyzed to design stable and robust synchronization control, even at a low power of 0.02 W. The control system is accomplished using commercial components, including a low-cost microcontroller, which eliminates the need for bulky control and external sensing hardware. This high power density design allows the receiver to be integrated into daily consumer electronics such as laptops and monitors. Finally, a wide-range and high-

resolution control scheme of the rectifier input phase is proposed to enable the dynamic impedance matching capability, maintaining high system efficiency over wide loading conditions.

In addition, to increase the WPT technology adoption to low-power consumer electronics, a small wireless receiver replacing conventional AA batteries is developed. This receiver can supply power to existing AA battery-powered devices while providing the benefit of WPT technologies to consumers.

TABLE OF CONTENTS

Chapter One Introduction 1

1.1 Wireless Power Transfer Overview 1

1.2 Inductive Power Transfer 2

1.3 Magnetic Resonance Wireless Power Transfer 4

1.4 Magnetic Resonant WPT System Structure 6

1.5 Summary and Outline 8

Chapter Two Literature Review 10

2.1 Impedance Matching 10

2.1.1 Traditional Techniques 12

2.1.2 Phase-shift Control Technique Using Active Rectifiers 15

2.2 Frequency Synchronization of Active Rectifier 17

2.3 Low-power Wireless Power Receiver 21

2.4 Summary and Motivation 23

Chapter Three Wireless Power Receiving Unit for AA-Battery-Powered Devices 25

3.1 Overall Structure and Principle 25

3.2 Receiving Coil 27

3.2.1 Receiver Coil Structure 28

3.2.2 Induced Voltage 30

3.2.3 Coil Inductance 32

3.2.4 Coil Capacitance 33

3.2.5 Coil Resistance 35
3.3 Multiphase Voltage-Doubler Diode Rectifier Modeling 36
3.4 Automatic Tuning Network 41
3.5 Prototype 44
3.5.1 Receiving Coil 44
3.5.2 PCB 44
3.5.3 Housing 47
3.5.4 EMI Shield 48
3.6 Experimental Verification 50
3.7 Summary 54
Chapter Four Synchronous Active Rectifier 56
4.1 Receiving Coil 56
4.2 Power Stage Model and Design 63
4.2.1 Circuit Topology 63
4.2.2 Discrete-time State-space Model of Power Stage 64
4.2.3 Steady-State Efficiency Modeling 67
4.2.4 Optimal Efficiency and Power Component Selection 69
4.3 Synchronization Control 72
4.3.1 Synchronization Control Principle 72
4.3.2 Small-signal Power Stage Model 74
4.3.3 Inherent Zero-Crossing Feedback Model 76
4.3.4 Synchronization Loop Dynamics 77

4.3.5 Compensator Design 78

4.3.6 Dynamic Control of the Rectifier Input Phase 81

4.4 Summary 84

Chapter Five Experimental Verification 86

5.1 Rectifier Prototype 86

5.2.1 Power Stage PCB Layout 86

5.2.2 Component Selection 90

5.2 Experimental Open-loop Operation 93

5.3 Experimental Open-loop Results 97

5.4 Experimental Closed-loop Operation 100

5.5 Dynamic Control of the Rectifier Input Phase 102

5.6 Summary 105

Chapter Six Conclusions and Future Work 108

6.1 Conclusions 108

6.1.1 Wireless Power Receiving Unit for AA-Battery-Powered Devices 108

6.1.2 Frequency Synchronous Active Rectifier 109

6.2 Future Work 112

List of References 114

Vita 123

LIST OF TABLES

Table 3.1. Receiving coil dimensions. 45

Table 3.2. Coil parameter values. 45

Table 3.3. AAPRU prototype circuit components. 46

Table 3.4. Cost breakdown of the AAPRU prototype. 51

Table 3.5. AAPRU operating conditions. 53

Table 3.6. Equipment part numbers. 53

Table 4.1. Compensator and compensated loop gain parameter values. 81

Table 5.1. Prototype circuit parameters. 86

Table 5.2. Prototype component numbers. 87

Table 5.3. Specifications of the WPT system. 94

Table 5.4. Equipment part numbers in the open-loop setup. 94

LIST OF FIGURES

Fig. 1.1. Illustration of the IPT system [1]. 3

Fig. 1.2. Illustration of the magnetic resonant WPT [1]. 4

Fig. 1.3. Structure of a resonant WPT system. 7

Fig. 2.1. AC equivalent circuit of a series-series resonant WPT based on the first harmonic approximation. 10

Fig. 2.2. AC equivalent circuit using two dependent sources to model the coupling two coils. 11

Fig. 2.3. Equivalent circuits of the receiver with (a) the SP IMN, and (b) the PS IMN… 14

Fig. 2.4. Example circuit schematic of the full-bridge active rectifier in resonant WPT systems. 15

Fig. 2.5. Block diagram of the synchronization approach using additional signaling hardware. 18

Fig. 2.6. Block diagram of the synchronization approach using magnetic sensing. 19

Fig. 2.7. Block diagram of the synchronization approach using PLL control. 20

Fig. 3.1. 3D models of (a) an AA battery, (b) complete, and (c) disassembled AAPRU prototype. 26

Fig. 3.2. Simplified block diagram of the power management circuit of the AAPRU..... 27

Fig. 3.3. Dual-coil structure of the receiving coils. 28

Fig. 3.4. Block diagram of the AAPRU power management circuit connected with dual-coil setup. 29

Fig. 3.5. Geometry of the proposed individual coil in (a) top view and (b) side view. 29

Fig. 3.6. Magnetic flux through the coil area. 30

Fig. 3.7. Simulated induced voltage magnitude with varying θ in an example single rectangular coil. 31

Fig. 3.8. Simulated induced voltage magnitude in open-circuited dual coils. 32

Fig. 3.9. Simulated magnetic flux distribution from example coils. 33

Fig. 3.10. Parasitic capacitance model of the rectangular coil. 34

Fig. 3.11. (a) RLC model, and (b) RL model of the Rx coil. 35

Fig. 3.12. Proposed diode rectifier circuit with an automatic tuning network. 36

Fig. 3.13. Example waveforms per switching period. 37

Fig. 3.14. AC equivalent circuit of the diode rectifier in steady-state. 38

Fig. 3.15. Block diagram of the tuning network. 42

Fig. 3.16. AC equivalent circuit when Q_1 is on. 43

Fig. 3.17. Non-inverting Schmitt trigger schematic. 43

Fig. 3.18. A prototype of receiving coils. 45

Fig. 3.19. (a) 3D model and (b) prototype of the PCB containing the power management circuit. 46

Fig. 3.20. 3D models of the plastic (a) inner housing, and (b) outer housing. 48

Fig. 3.21. (a) 3D model, and (b) prototype of the EMI shield. 49

Fig. 3.22. Cross-sectional view of the simulated magnetic field inside (a) the unshielded housing, and (b) the shielded housing. 49

Fig. 3.23. (a) Prototypes of all AAPRU layers, (b) complete AAPRU prototype, and (c) an example application with a wireless mouse. 51

Fig. 3.24. Experimental setup for testing the AAPRU. 52

Fig. 3.25. Block diagram of the experimental setup. 52

Fig. 3.26. (a) Experimental and (b) modeled operating waveforms of the AAPRU. 53

Fig. 3.27. Experimental signals showing the functionality of the AAPRU prototype..... 54

Fig. 4.1. Receiving coil geometry. 57

Fig. 4.2. 3D model of the metal sheet.. 58

Fig. 4.3. (a) Top view of the simulated eddy currents on the metal sheet and (b) side view of the simulated magnetic flux density in the conventional cutting method. 59

Fig. 4.4. 3D model of the slot-cut metal plate. 60

Fig. 4.5. (a) Top view of simulated eddy current on the metal sheet and (b) side view of simulated magnetic flux density in the new shielding method. 61

Fig. 4.6. 3D model of the complete coil setup. 62

Fig. 4.7. Circuit schematic of the proposed rectifier..... 63

Fig. 4.8. Example steady-state rectifier waveforms..... 65

Fig. 4.9. Equivalent circuit schematics in each interval 66

Fig. 4.10. Rectifier power loss chart. 68

Fig. 4.11. Rectifier efficiency optimization process 70

Fig. 4.12. Analytical rectifier efficiency with varying Lr 71

Fig. 4.13. Synchronization control structure. 73

Fig. 4.14. Block diagram of the synchronization loop including the converter dynamics. 78

Fig. 4.15. Bode plots of $Tsync, un(z)$ and $Tsyncz$. 79

Fig. 4.16. Compensator circuit schematic. 80

Fig. 4.17. Implementation of the phase control scheme. 82

Fig. 4.18. Block diagram of the phase angle control scheme. 83

Fig. 4.19. Analytical control range of $\phi vs, is$ with varying Ros 84

Fig. 5.1. Synchronous rectifier prototype. 87

Fig. 5.2. 3D model of the rectifier power stage layout in Altium Designer. 88

Fig. 5.3. Power stage layout in different layers 89

Fig. 5.4. (a) Color-coded example power current path in the 3D PCB layout, and (b) circuit schematic with the same current path. 90

Fig. 5.5. Symmetrical rectifier waveforms at full load with minimal ringings and overshoot. 91

Fig. 5.6. Experimental setup of the open-loop test. 93

Fig. 5.7. Circuit schematic of the ZVS half-bridge inverter. 95

Fig. 5.8. Block diagram of the synchronization scheme in open-loop operations. 96

Fig. 5.9. (a) Open-loop experimental rectifier waveforms, and (b) modeled waveforms. 97

Fig. 5.10. Waveforms from the open-loop WPT systems using (a) an active rectifier, and (b) a diode rectifier. 99

Fig. 5.11. Power loss breakdown comparison of WPT systems consisting of a synchronous active rectifier and a diode rectifier. 99

Fig. 5.12. Comparison of step response of $G\phi z, \phi 1$ between experimental results with different models, including previous work [39]. 100

Fig. 5.13. Closed-loop experimental setup. 101

Fig. 5.14. Block diagram of the closed-loop setup. 102

Fig. 5.15. Experimental rectifier waveforms in closed-loop operation at full load (40W). 103

Fig. 5.16. Experimental rectifier input phase showing the synchronization at 40 W. 103

Fig. 5.17. Experimental closed-loop (a) operating waveforms and (b) rectifier input phase showing the synchronization at 0.02W. 104

Fig. 5.18. Comparison of the experimental and analytical $\phi vs, is$ in the phase control. 106

Fig. 5.19. Control range of $\phi vs, is$ with different Ros values..... 106

Chapter One

INTRODUCTION

1.1 Wireless Power Transfer Overview

Wireless power transfer (WPT) has been a popular topic in research for decades and rapidly developed in recent years. WPT is the technology allowing to transfer electromagnetic energy from the source to the load without the use of cords [1]. The energy can be transferred through an air gap or other non-conductive media over a distance.

Some of the main benefits that wireless charging introduces are the improved consumer experience as the hassle from connecting cables is eliminated and the ability to charge devices at unreachable positions, e.g., body-implanted devices. Because of the increase in consumer preference for wireless connectivity in recent years, WPT technology has been rapidly implemented in various sectors, such as consumer electronics, automotive, and healthcare [2], [3], boosting WPT to a multi-billion dollar industry. Wireless-charging capable devices range from high-power devices, such as smartphones, headphones, or laptops [4], to low-power Internet of Things (IoT) devices [1], [5]. In 2018, the WPT market was worth approximately $5.26 billion and expected to grow to $29.23 billion by 2027 [6]. However, there are some technical problems hampering this technology adoption, including inefficiency in power transfer, inflexible freedom of movement, and a limited number of charged receivers. [1]

There are two types of WPT principles, i.e., radiative wireless charging and non-radiative wireless charging (coupling-based wireless charging). Due to the safety concern,

non-radiative wireless charging is commonly used in consumer electronics instead of radiative ones [1]. This work only discusses the latter principle, which is divided into two categories, i.e., inductive coupling (Qi standard) and magnetic resonance coupling (Airfuel standard).

1.2 Inductive Power Transfer

The inductive power transfer (IPT) technique utilizes the magnetic induction to transfer power from the transmitting coil to the receiving coil. When two coils are placed in proximity to each other, they are magnetically attached and start transferring energy. More specifically, the magnetic field generated by the alternating current in the transmitting coil is coupled with the receiving coil. According to Faraday's law, when the magnetic flux passes through the surface enclosed by the receiving coil varies in time, an electromotive force is produced on the coil. When the receiving coil is terminated by a finite impedance, this force then causes the current to flow through the receiver coil, transferring power to the load. Because the magnetic field is quickly attenuated in the air over distance, the power transfer distance is relatively short, meaning coils have to be tightly coupled [7]. An example of magnetically coupled coils in the IPT system is shown in Fig. 1.1.

The IPT technology is commonly applied in commercial devices complying with the Qi standard, a global standard for wireless charging developed by the Wireless Power Consortium (WPC) in 2011 to ensure the interoperability between Qi-compliant devices, regardless of the manufacture [8]. The operating frequency ranges from 87 kHz to 205 kHz

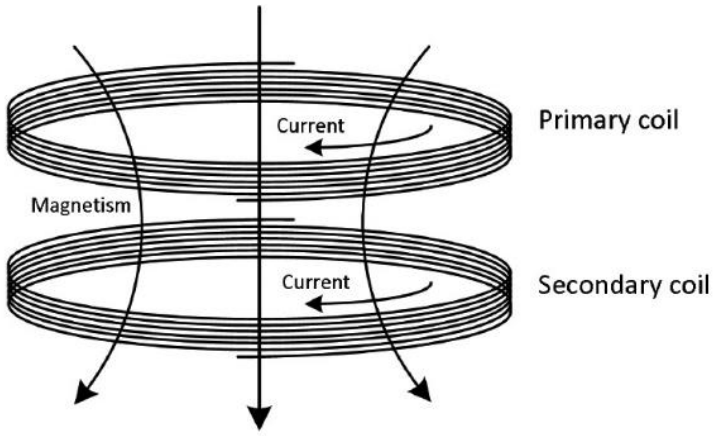

Fig. 1.1. Illustration of the IPT system [1].

for wireless chargers delivering less than 30 W [8]. Qi aims the end-to-end system efficiency to be higher than 70% [1].

One of the advantages of the Qi-compliant IPT system is the ability to adjust the amount of transferred power by changing the operating frequency of the charger. Also, operating at a lower frequency than that of the counterpart standard simplifies the control design. The well-developed communication protocol is used to enable the synchronization and exchange of power level information between the transmitter and receiver [8]. Finally, the WPT technology used in Qi is more matured than that of other standards as it was one of the first standards to be established. Due to its benefits, Qi is now the most common wireless charging standard used in mobile applications, with more than 3700 products manufactured by popular technology companies, e.g., Samsung and Apple. Examples of Qi-compliant products using the IPT technology are smartphones, wireless headphones, and smartwatches.

However, like every other technology, IPT also has some downsides. Because coils are not compensated to achieve high quality factors, charging distance must be within the coil diameter and is typically less than 20 cm [1]. Also, the receiving coil must be strictly aligned with the transmitter coil in the charging pad to achieve tight coupling, reducing the tolerance for spatial movement. In addition, the tight coupling technique only allows one device to be charged at a time, which lengthens the charging time if the user has multiple devices that need to be charged and only a single charging pad.

1.3 Magnetic Resonance Wireless Power Transfer

Another non-radiative coupling-based WPT technique is the magnetic resonance coupling. In this technique, resonant coils are used to transfer and pick up electrical energy through oscillating magnetic fields. The coil resonant frequencies are identical and tuned by adding corresponding capacitors either in parallel or series with the coil, as shown in Fig. 1.2.

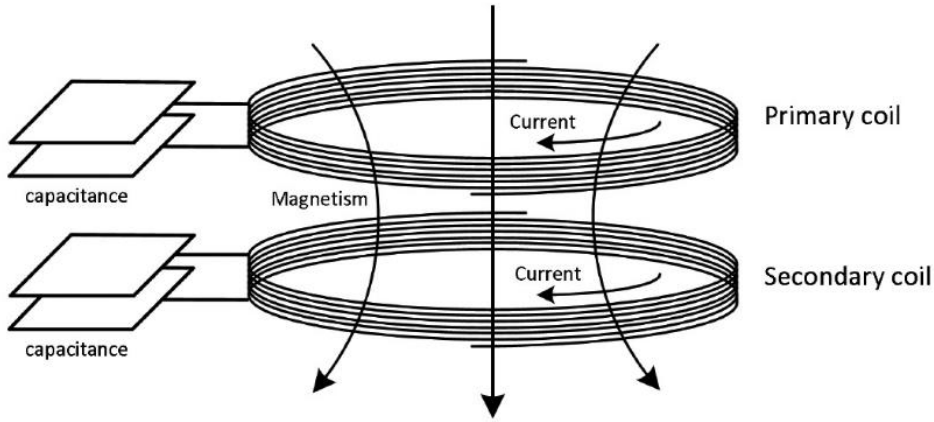

Fig. 1.2. Illustration of the magnetic resonant WPT [1].

The capacitance cancels out the coil positive reactance at the operating frequency, increasing the quality factor [9]. This is one of the impedance matching methods used to reduce the reactance in the power-delivering path in ac circuits. As a result, a vast majority of energy is transferred with minimal resistive losses even at a relatively large air gap, enabling coils to be loosely coupled. This technique was discovered by Nikola Tesla when he used resonant circuits to enhance his wireless transfer efficiency in an experiment more than a century ago [9].

A standard named “Airfuel” has been developed by Alliance for Wireless Power (A4WP) since 2012 to ensure the interoperation between magnetic resonant devices and compete directly with the Qi standard. This standard requires the operating frequency to be at 6.78 MHz, which is much higher than that of the Qi standard. 6.78 MHz is the lowest industrial scientific medical (ISM) band, which means that the electromagnetic radiated emission (EMI) is not limited, leading to fewer regulatory restrictions [10]. At high frequencies, passive components and coil sizes are significantly reduced, allowing designers to build more compact devices. Also, the quality factor tends to increase at higher frequencies, enhancing coupling efficiencies [10].

Due to the superior characteristics of magnetic resonance, it has unlocked numerous benefits for the WPT system, which are not feasible with IPT. The receiver can now be charged with improved spatial freedom, allowing the consumer to continue to use their devices while charging them. More specifically, the charging distance can be increased up to 50 mm, and the charging position does not need to be precisely aligned with the charging coil. This property ultimately increases the user’s experience with WPT technology.

The magnetic field from resonant coils is able to penetrate various non-conductive materials, allowing the transmitter to be mounted underneath of the furniture surface instead of being drilled into surfaces.

The power transfer efficiency is relatively high. Previous demonstrations in [11] and [12] show that magnetic resonant WPT systems at 6.78 MHz can deliver 10W and 300W output power, respectively, over a long charging distance with an end-to-end efficiency of 85%.

Magnetic resonant WPT system can operate at a wide range of output power, ranging from milliwatt applications [13] to kilowatt applications [14]. Since the Airfuel-compliant WPT system operates at a high frequency, the size of passive components is substantially reduced, allowing higher power density. Importantly, the loose coupling mechanism enables multiple devices to be charged concurrently from a single transmitting coil, which has been demonstrated in many studies [15], [16].

Despite the advantageous characteristics of the loosely-coupled WPT system, there are many challenges that need to be addressed before this technique can be widely adopted. One of those challenges is the complexity of the design due to the high operating frequency and varying coil position. Also, in-band communication is not employed in Airfuel systems, which is considered as a shortcoming compared to Qi IPT systems [17].

1.4 Magnetic Resonant WPT System Structure

Due to advantageous characteristics of the magnetic resonant coupling technique, the resonant WPT is investigated and referenced throughout the rest of this thesis. Fig. 1.3 shows a typical structure of the single-receiver resonant WPT. The transmitter is comprised

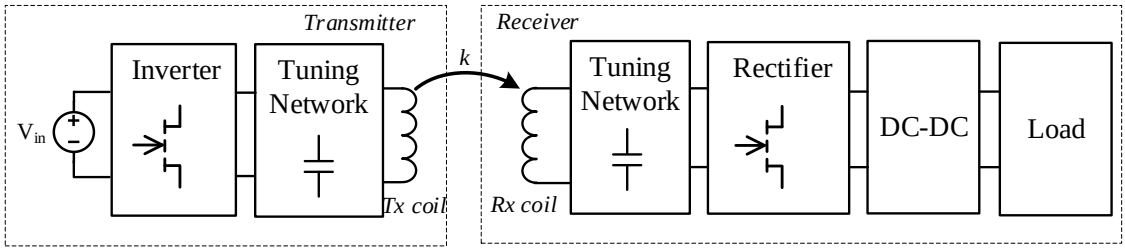

Fig. 1.3. Structure of a resonant WPT system.

of a dc voltage source, inverter, capacitive tuning network, and transmitting (Tx) coil. If the input is an ac voltage source, an additional ac-dc converter, e.g., power factor correction (PFC) and rectifier, is added between the source and the inverter [18]. The receiver consists of a receiving (Rx) coil, capacitive tuning network, rectifier, dc-dc converter, and load. In some mobile electronics applications, the dc-dc is the battery charger connected to the battery. The Rx coil is typically tuned to resonate at the switching frequency to minimize the reactive power for high efficiency. Also, in some topologies, the impedance matching network is used between the power stage and coil to maintain high efficiency over a wide operating range [18], [19]. Thus, there are many possible structures for implementing resonant WPT systems and Fig. 1.3 only shows the example structure that is used in this thesis.

The design of the receiver circuitry, including the rectifier power stage and its control, is the main focus of this thesis. One of the challenges for designing receivers maintaining high efficiency in resonant WPT systems is the varying load condition. The solution addressing this issue by using an active rectifier with impedance control will be analyzed and demonstrated.

1.5 Summary and Outline

Non-radiative wireless power transfer works by transferring energy through the magnetic field between coupled coils. It is divided into two categories: inductive WPT and magnetic resonant WPT. The IPT utilizes the tightly coupled technique that has a short charging distance, restricted spatial movement, and one-to-one charging capability. On the other hand, the resonant WPT uses capacitors to compensate for coil inductance, enabling coils to be loosely coupled. The benefits of this system include long charging distance, flexible coil orientation, and multiple-receiver charging capability. The resonant WPT used in consumer electronics is regulated by the Airfuel standard that requires the system to operate at 6.78 MHz, introducing both advantages and challenges to the design.

Following the introduction is the literature review in Chapter 2 describing the most significant issues in magnetic resonant WPT systems. The pros and cons of previous solutions to these issues are discussed. The benefits and lack of resonant WPT implementation in low-power consumer devices are pointed out. Designs for a highly-efficient GaN-based active rectifier and low-power receiver are proposed to address those issues.

Chapter 3 presents the structure and design process of an AA-battery-sized receiver for low-power consumer electronics. Chapter 4 is focused on designing a GaN-based synchronous active rectifier for high-power applications. It describes the circuit topology, models steady-state operations, and proposes the optimization procedure for designing the power stage. Also, a stable and compact control system is presented. Following this, Chapter 5 details open-loop and closed-loop experiments that are carried out to validate the

proposed highly-efficient rectifier power stage and control scheme. Finally, Chapter 6 concludes research outcomes, summarizes achievements, and provides future work for improving the design.

Chapter Two

LITERATURE REVIEW

2.1 Impedance Matching

Fig. 2.1 and Fig. 2.2 show an ac equivalent circuit of a series-series resonant WPT system shown in Fig. 1.3. $Z_{rec} = jX_{rec} + R_{rec}$ is the equivalent load (rectifier) impedance. The output impedance Z_o denotes the impedance seen by the output. $Z_s = R_s + jX_s = R_s + j(\omega L_s - 1/\omega C_s)$ is the secondary open-circuit impedance. The power transfer efficiency is maximized when the equivalent load reactance X_{rec} cancels out the secondary reactance X_s and the load resistance R_{rec} is set to an optimal value $R_{rec,opt} = \sqrt{R_s^2 + \frac{R_s}{R_p}(\omega_s M)^2}$ [20-22]. Therefore, the impedance matching conditions for maximizing the WPT system efficiency are $X_{rec} = -X_s$ and $R_{rec} = R_{rec,opt}$.

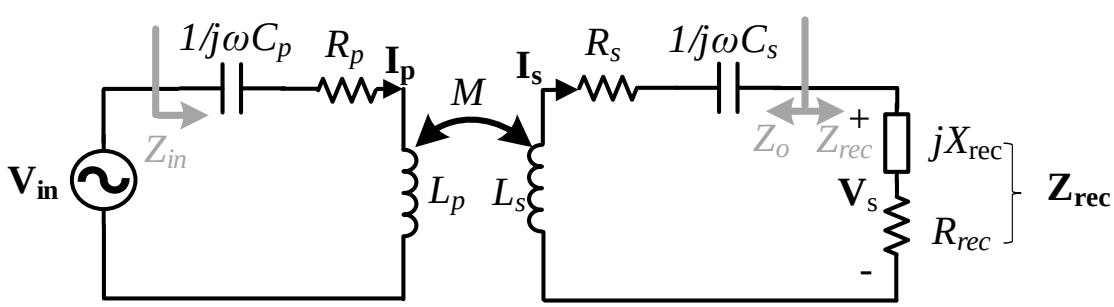

Fig. 2.1. AC equivalent circuit of a series-series resonant WPT based on the first harmonic approximation.

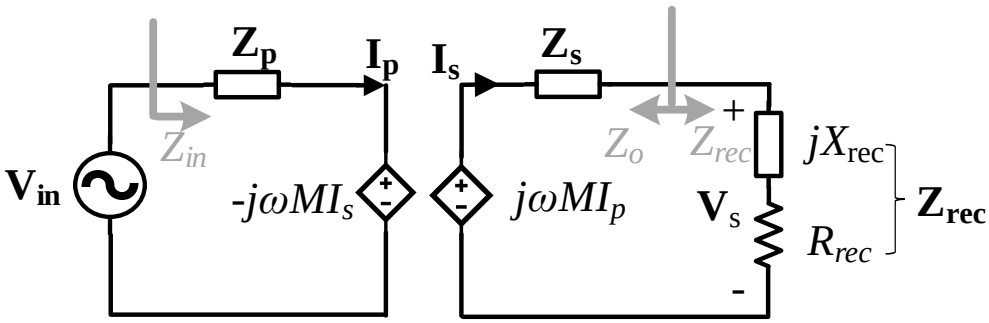

Fig. 2.2. AC equivalent circuit using two dependent sources to model the coupling two coils.

As previously mentioned, one of the advantages of WPT via magnetic resonant coupling is the ability to change the charging distance and coil spatial position due to loosely-coupled coils. However, this benefit introduces a challenge in the system design. When the transmission distance is changed away from the originally designed value the coupling between coils is also changed, leading to different $R_{rec,opt}$ and Z_{rec}. Consequently, the load reactance X_{rec} is not completely canceled out by the secondary reactance X_s and the load resistance R_{rec} is different from $R_{rec,opt}$. Thus, the power transfer efficiency is drastically decreased [23], [24].

In addition, most portable WPT systems are used to charge Li-ion batteries inside mobile devices. These batteries are typically charged at constant current and then charged at constant voltage when the maximum cell voltage is reached [25]. Because of this capacity-dependent charging process, the battery load can be considered as a variable load, which also results in impedance mismatch in the WPT system.

Therefore, in order to improve the overall efficiency of WPT systems under dynamic loading impedance due to varying load and coil coupling, numerous solutions for matching impedance ($X_s = -X_{rec}$, $R_{rec} = R_{rec,opt}$) have been proposed in previous research. These solutions can be divided into four main categories: (1) hardware modification, (2) frequency tracking, (3) impedance matching network, and (4) synchronous active rectifier.

2.1.1 Traditional Techniques

In the first impedance matching approach, hardware modification, the physical hardware of the system is modified to achieve the optimal operating point where the impedance is matched. The work in [26] proposes a transmitter coil consisting of multiple sub-coils with various radii. Depending on the separation distance, the transmitting coil radius resulting in the optimal coupling coefficient is electronically selected to maximize the system efficiency. Verified by experiments, the digital transmitting coil increases the efficiency from 12% to 20% compared to that of the detuned coil with a constant radius when the transfer distance is four times the receiving coil radius [26]. This approach does not require the additional lossy circuitry and complex mathematical analysis. However, the coil system is too bulky to be implemented in portable electronic devices, and the number of available impedance-matching points is limited by hardware.

In the frequency tracking approach, the transmitter operating frequency f_s is the control parameter, which is dynamically swept to find the impedance-matching operating point [27-29]. The work in [27] utilizes a reflection power detector on the primary side to detect the reflection level at the transmitter, facilitating frequency selection. During the

frequency tracking mode, the switching frequency is swept by 10 kHz steps between 6.17 MHz and 6.78 MHz to find the optimal frequency resulting in the minimum reflection ($X_s = -X_{rec}$) [27]. However, changing the transmitter switching frequency is not always practical, especially in an Airfuel-compliant WPT system, where the allowed operating frequency is strictly limited to 6.78 MHz $\pm$ 15 kHz.

Impedance matching network (IMN) is a common circuit used in WPT systems for improving efficiency. The network is implemented using passive components in various configurations and can be divided into two types, adaptive and non-adaptive IMN.

Non-adaptive IMNs do not dynamically change impedance, but they can mitigate the negative effect of varying loading conditions by improving the static design. Capacitive IMNs consisting of parallel and series capacitors are widely used in WPT systems [30]. The series-parallel (SP) IMN on the receiver, shown in Fig. 2.3a, helps increase the system immunity to the load variation. In contrast, the parallel-series (PS), shown in Fig. 2.3b, is more effective in reducing the effect of the cross-coupling between adjacent receiving coils [30]. As a result, non-adaptive IMNs improve the average system efficiency for various loading conditions. Compared to adaptive IMNs, non-adaptive IMNs reduces the number of passive components and eliminates microcontrollers, resulting in more board space and lower loss. The shortcoming of this approach is the lack of ability to achieve optimization at individual operating points across the varying loading impedance.

In the adaptive IMN approach, a tunable impedance matching network consisting of passive components is employed to achieve high efficiency across a wide distance variation [19, 23, 31]. These networks are dynamically reconfigured according to the

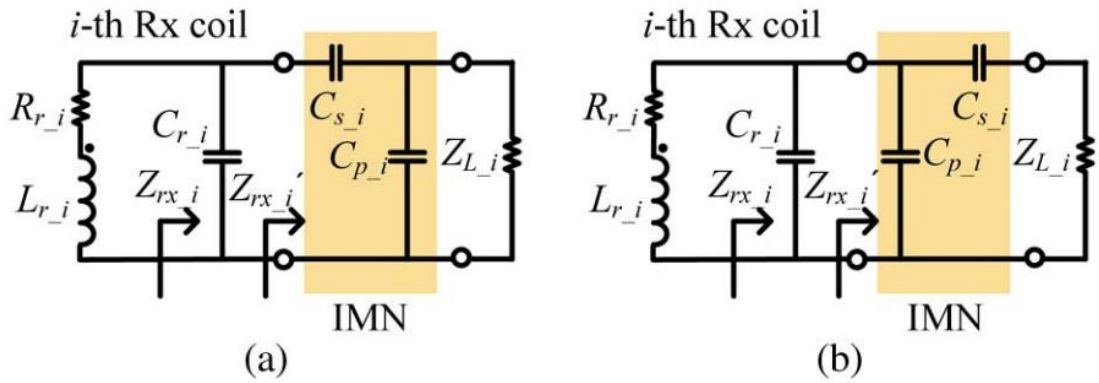

Fig. 2.3. Equivalent circuits of the receiver with (a) the SP IMN, and (b) the PS IMN.

equivalent load impedance using microcontrollers. The algorithm programmed in the controller computes the optimal combination of passive component and selects them by turning on corresponding electric relays. IMNs can be added to only the transmitter or to both sides. References [31] and [19] utilize the L-type matching impedance network on the primary side. Whereas, the work in [23] implements the capacitor matrix circuit in both transmitter and receiver to realize range-adaptive WPT systems. Recently, more complex automatic impedance matching techniques have been studied, including a technique where integrated machine learning is used to control the impedance-matching network automatically [33]. The superior property of adaptive IMNs is the ability to adjust the system impedance precisely. However, the drawback of this approach is the large board space occupied by idle relays and passive components. If inductors are used in IMNs, inductor winding and core losses can be considerable.

All the mentioned approaches have a few similar disadvantages. They require large space (except the non-adaptive IMN), which is not feasible to implement in small consumer

electronics. Although non-adaptive IMNs are not bulky, this impedance matching approach only improves the average efficiency rather than optimizing individual operating points.

2.1.2 Phase-shift Control Technique Using Active Rectifiers

The final approach, which is used in this work, utilizes the synchronous full-bridge active rectifier on the receiver side instead of a traditional diode full-bridge rectifier due to its superior properties, including high efficiency and impedance regulation ability. An example circuit schematic of the full-bridge rectifier used in resonant WPT systems is shown in Fig. 2.4. The rectifier phase angle ϕ_{v_s,i_s} is defined as the phase difference between zero-crossing points of the secondary voltage v_s and secondary current i_s. Since the equivalent load impedance depends on ϕ_{v_s,i_s}, changing ϕ_{v_s,i_s} alters the equivalent load

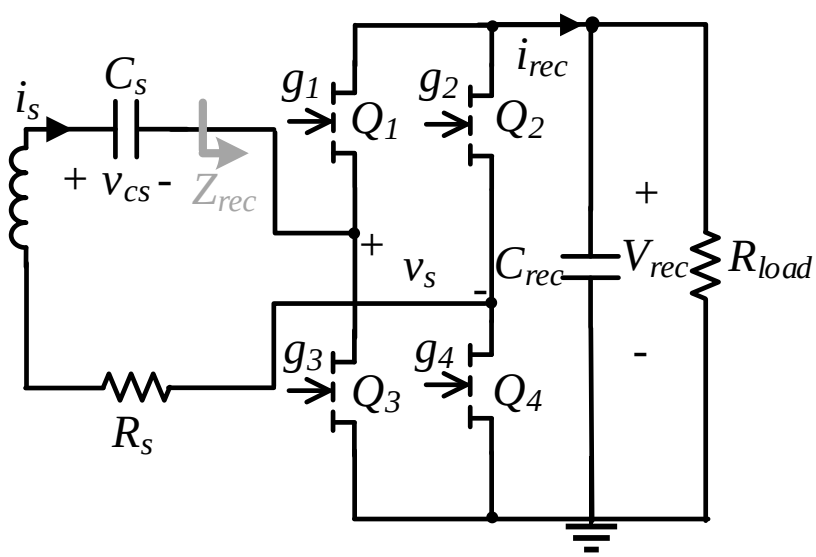

Fig. 2.4. Example circuit schematic of the full-bridge active rectifier in resonant WPT systems.

impedance Z_{rec}. When v_s and i_s are in phase, the equivalent load is purely resistive. In contrast, the non-zero rectifier phase angle introduces a reactive part in the equivalent load. As demonstrated in many studies, using active rectifiers gives designers the ability to control ϕ_{v_s,i_s} by adjusting gate signal timing, leading to controlling the equivalent load impedance [20, 32-34].

In the previous study [34], the input phase of the rectifier is the only control parameter, which cannot be used to control load reactance and resistance separately. Consequently, the maximum efficiency is not reached. The work in [20] utilizes another control parameter, i.e., the rectified voltage V_{rec}, to provide an additional degree of design freedom enabling separate control of the equivalent load impedance. A dc-dc converter is cascaded between the rectifier and the load regulating the output voltage to meet the device voltage requirement. The rectified voltage is adjusted by either changing the rectifier duty cycle or dc-dc converter duty cycle [20]. The benefit of this technique is the impedance matching ability via the phase shift and rectified voltage over a wide range of loading conditions. The work in [35] was able to increase the power transfer efficiency in a 6.78 MHz WPT system by 10% compared to a system using traditional diode rectifiers by using the phase-shift control technique.

At the allowed operating frequency of 6.78 MHz in the Airfuel standard, the rectifier switching loss in the hard-switching mode takes a considerable portion of the total loss hampering the system's overall efficiency because it is directly proportional to the switching frequency. Therefore, the soft-switching technique is preferable to operate active rectifiers in the AirFuel-compliant WPT system to eliminate the vast majority of the

switching loss. This thesis adopts an advanced full-bridge active rectifier proposed in [32], which has a resonant tank at the input assisting the zero-voltage-switching operation of the rectifier.

2.2 Frequency Synchronization of Active Rectifier

Although there are many benefits of using active rectifiers in WPT systems, a challenge arises in controlling the active rectifier, especially in megahertz applications. In order to ensure the proper phase-shift operation of the active rectifier, driving signals of the rectifier must be locked with the receiver current with a constant offset in steady-state. In order words, its switching actions have to be synchronized with the generated magnetic field or, equivalently, synchronized with the inverter switching actions. The gate signals of the rectifier and inverter are locked in phase with a constant phase offset in steady-state, resulting in an equal frequency of 6.78 MHz. However, there is no electrical connection between the transmitter and receiver to facilitate the synchronization requirement, making simple wire synchronization infeasible. Therefore, synchronization of active rectifiers used in WPT systems needs to be solved in order to implement the phase-shift control technique for impedance matching.

At low frequencies, synchronization has been demonstrated using additional signaling hardware [36], magnetic field sensing [37], or phase-locked loops (PLL) [38, 39]. The first synchronization approach is depicted as a block diagram in Fig. 2.5. Additional hardware is added to both sides to sample the primary current i_p and secondary voltage v_s to measure the phase difference between switching actions of the inverter and rectifier. The phase information is then transferred between two sides via ISM RF signals using

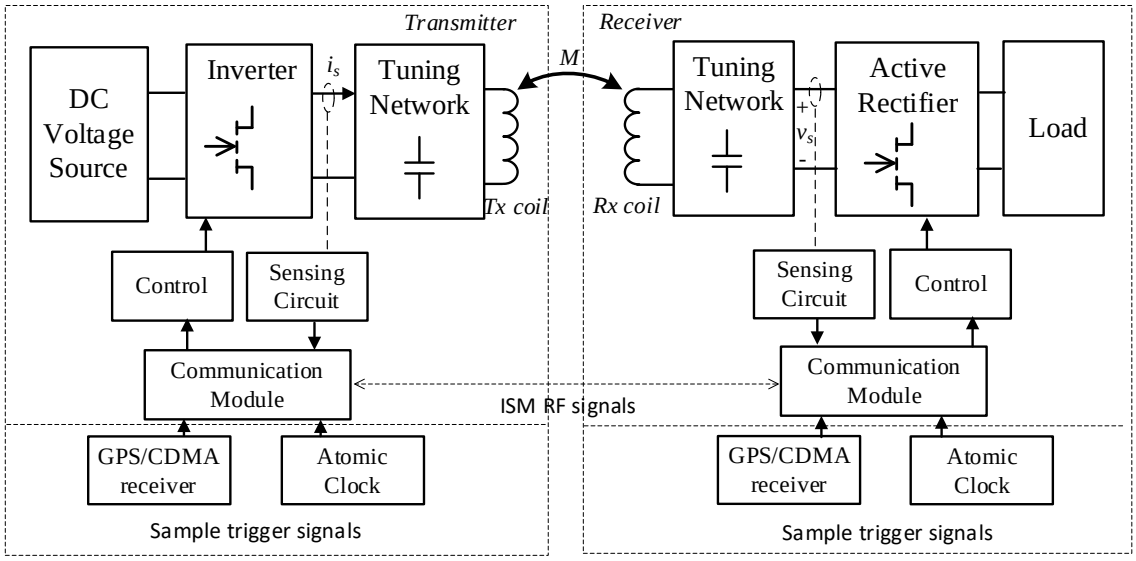

Fig. 2.5. Block diagram of the synchronization approach using additional signaling hardware.

communication modules. Synchronous sampling of i_p and v_s is required to ensure the synchronous operation of the inverter and rectifier. However, samplers cannot be locked from a common source since they are located separately in the transmitter and receiver. To address this issue, [36] utilizes either satellite synchronization signals or on-board atomic clocks as trigger signals for samplers. A GPS/CDMA receiver is required for receiving satellite synchronization signals, and on-board clock sources require periodic calibrations to account for a small discrepancy in frequency [36]. However, this synchronization approach is generally bulky and expensive because of the required additional hardware for sensing, wireless communication, and synchronous sample trigger signals.

In [37], a sensing coil is placed between the transmitting and receiving coils to extract the magnetic field frequency based on the induced voltage, as shown in Fig. 2.6.

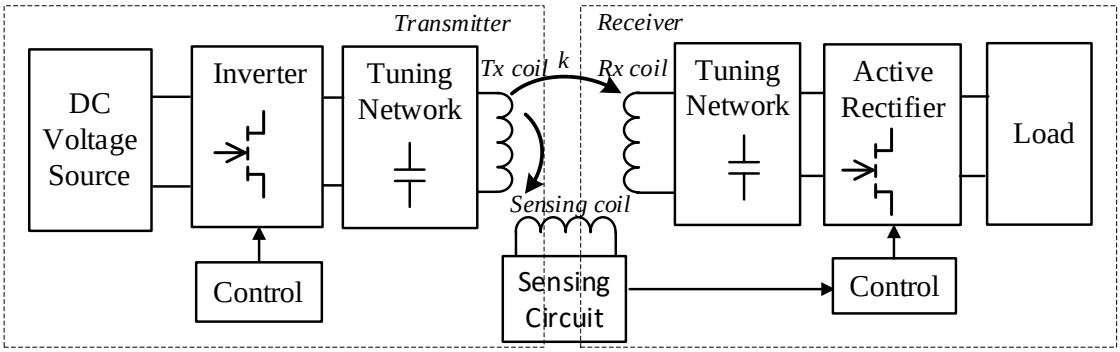

Fig. 2.6. Block diagram of the synchronization approach using magnetic sensing.

This method requires analyzing the sensing coil position and designing a compensator because the secondary current also affects the sensed induced voltage. When the coupling coefficient is reduced by 50%, causing the system to not synchronize accurately, the phase error ramps up to more than 20% [37]. This method depends on a pre-measured coupling coefficient, which defeats the spatial freedom of using the magnetic resonance WPT system. Also, the sensing coil adds an extra cost and may be too large to be installed in consumer electronics.

The third method is to synchronize rectifier switching actions to a local signal depending on the WPT magnetic field, as shown in Fig. 2.7. The PLL-based synchronization controller samples the sensed signal and generates a feedback signal that is phase-locked to the sensed signal, resulting in equal frequencies. That feedback is also used to drive the switching actions of the rectifier, synchronizing the rectifier operation to the magnetic field (transmitter operation). The PLL controller has been successfully demonstrated at low frequencies by employing the commercial FPGA development board or DSP [33, 38, 39].

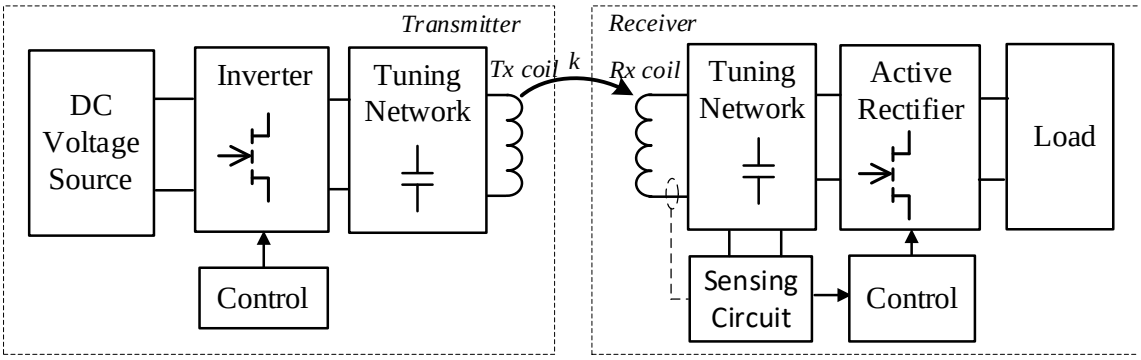

Fig. 2.7. Block diagram of the synchronization approach using PLL control.

In [33], the secondary current i_s is sensed to generate a reference signal fed to an FPGA. The FPGA outputs synchronous PWM signals controlling the power stage. However, the sensed current is relatively small at low power levels, making it susceptible to noise. Furthermore, the zero-crossing point of i_s is in proximity to the rectifier switching time, leading to the undesired interference of switching noise in the signal detection. Thus, the secondary current is not preferred for the sensed signal. Another sensed signal, the voltage across the secondary tuning capacitor v_{cs}, has been used in [38, 39]. The capacitor voltage is typically 90° out of phase with the rectifier switching actions, improving the immunity to the switching noise [39].

Therefore, the synchronization approach based on PLL techniques with the sensed signal v_{cs} is adopted in this thesis due to its robustness in synchronization performance, even at low power. The ultimate goal is to design the first PLL-based synchronization controller for active rectifiers in 6.78 MHz resonant WPT systems by utilizing compact commercial components, including a low-cost microcontroller. The controller must have

an ability to synchronize the rectifier at steady-state and dynamically adjust the rectifier phase angle to regulate the load impedance.

Despite the mentioned benefits, the complex analysis of the control loop gain introduces a challenge of this synchronization technique. The sensed signal v_{cs} not only depends on the transmitter operation but also is impacted by the receiver operation, resulting in an inherent feedback loop from the rectifier power stage to the input of the synchronization system. In other words, the synchronous gate drive signals used to drive the rectifier changes the power stage dynamics, leading to a modification in operating waveforms, including the sensed capacitor voltage. Without considering this inherent feedback in the control design, the system may be unstable. The recent study in [39] addresses this issue by establishing an analytical framework based on discrete-time techniques to model this feedback when designing the dynamic behavior of the synchronization control. However, the method does not include modeling of the effects of ZVS intervals. An extended version of this modeling method is proposed in this thesis, where details of the ZVS dynamics during the converter deadtime are accounted for to improve the model accuracy.

2.3 Low-power Wireless Power Receiver

In addition to tens of watts applications that are the focus of recent WPT studies, the global electronics market consists of a large portion of low-power battery-operated consumer devices. According to [40], there are more than 900 million devices that use household-type batteries. These batteries come in various sizes, of which AA size is the most common. More importantly, 51% of batteries in Europe are made of alkaline

manganese, which is not rechargeable and toxic for the environment [41]. Over three billion batteries end up in landfills each year in the U.S. [42]. Also, non-rechargeable batteries must be replaced frequently, which is a hassle and not feasible in some cases. Consequently, replacing household batteries causes inconvenient consumer experiences and substantial environmental problems. Therefore, the WPT technology becomes a promising solution to solve this issue by extending the battery life or completely replacing them in low-power consumer devices. As a result, the adoption of WPT technology is driven by the predominance of small battery-powered consumer electronics in the electronics market.

There are only a few studies on the implementation of the resonant magnetic WPT technique in AA battery-powered consumer devices. Most of them focus on medical devices implanted in the human body [2] or placed in unreachable positions [13], where WPT is the only feasible option to power those devices. In [43], an AA-battery sized energy transducer is developed to convert mechanical energy into electrical energy by leveraging magnetic induction. The principle of this product is similar to that of the power receiving unit (PRU) in the WPT system, but instead of using the transmitter as the energy source, it uses the resonant mechanical movement of a local permanent magnet. More specifically, a vibrating permanent magnet inside the transducer housing generates an alternating magnetic field passing through the receiving coil wound around the magnet [43]. However, most AA-battery-powered devices operate in a stationary state, meaning the input vibration of the magnet is zero. Also, [43] is designed for RF transmission systems that require only a micro power source, which is not sufficient to supply the power needed for consumer

electronics. The structure and principle of this transducer are worth investigating to design the PRU replacing the standard AA battery in the WPT system.

Another interesting product from Ossia called “Forever Battery” is claimed to be a wireless rechargeable AA battery [42]. Since the product is not available in the market yet, the internal structure remains unknown, but the physical shape and basic principle are revealed. It has the form factor of a standard AA battery and can be charged wirelessly from radio waves at 2.4 GHz. Those waves are transmitted from separate transmitters installed inside the house to antennas mounted inside the product. According to the company, the transmitter can track the receiver position and broadcast RF signals directly to the device, even when the device is moving. Due to the lack of available technical information about this product, its theoretical principle cannot be validated.

2.4 Summary and Motivation

Loosely-coupled WPT systems offer greater spatial freedom of charging location, which is desirable for consumer electronics applications but also introduces a great challenge in design. Variations in coupling due to the spatial location of the receivers, or the presence of conductive elements in the field may alter the transmitter load reactance, degrading efficiency. One of the promising solutions is to use active rectifiers with the impedance-regulation capability to compensate for varying operating conditions and retune the network to maximize end-to-end WPT efficiency. In addition, GaN FETs dissipate less loss than diodes because of their low on-resistance and parasitic capacitance.

In order to regulate the impedance and achieve high efficiency, the rectifier must first synchronize its switching actions to the WPT field, then dynamically vary its phase to

cancel out the reactive impedance. Synchronization techniques using signaling hardware and magnetic field sensing may be too large for daily consumer applications. The PLL technique offers robust synchronization with small required additional hardware but has not been designed in a compact form for Airfuel WPT systems. Also, there exists inherent feedback from the power stage dynamics to the sensed signal that must be analyzed when designing the synchronization control.

In this thesis, an improved modeling approach of the synchronization loop dynamics that accounts for the resonant interval and the state-dependent switching actions is proposed using generalized discrete-time state-space techniques. In addition, the parasitic elements of various power transistors and passive components are included in the converter model to facilitate the component selection process and find the optimal operating condition yielding the highest efficiency. A compact PLL synchronization control network using low-profile commercial components is designed and demonstrated.

A review of WPT applications shows that the magnetic resonant WPT has not been widely adopted in low-power consumer electronics. Implementing WPT technologies into those devices will potentially accelerate the WPT adoption and unlock many benefits for customers and the environment. This thesis proposes an innovative design of the AA-battery-sized PRU that can be used to replace standard AA batteries and enable wireless charging capability for existing consumer low battery-powered applications.

Chapter Three

WIRELESS POWER RECEIVING UNIT FOR AA-BATTERY-POWERED DEVICES

In this chapter, an AA-battery-sized wireless power receiving unit (AAPRU) is developed to replace conventional AA batteries. The design goal is to build a compact wireless PRU that can fit in the existing AA battery holder and supply enough power to the device. For protecting the AAPRU from overvoltage and extending the operating range, an automatic tuning scheme is added to the circuit. The detailed structure and power stage model are discussed in this chapter.

3.1 Overall Structure and Principle

The proposed AAPRU is used to store the energy received from the transmitter in a small rechargeable battery and supply power to the electronic device. Fig. 3.1b illustrates the 3D model of the assembled AAPRU prototype in the similar shape of the AA battery model shown in Fig. 3.1a. Fig. 3.1c shows the exploded view of the AAPRU structure consisting of four main components: 1) receiving coils, 2) power management circuit, 3) electromagnetic interference (EMI) shield, and 4) inner and outer housings.

The fundamental principle of the AAPRU is described as follows. When the alternating magnetic flux passes through the coil's closed area, an ac voltage is induced in the loop, according to Faraday's law of electromagnetic induction. The induced voltage forces an alternating current to flow through the Rx coil. The power management circuit,

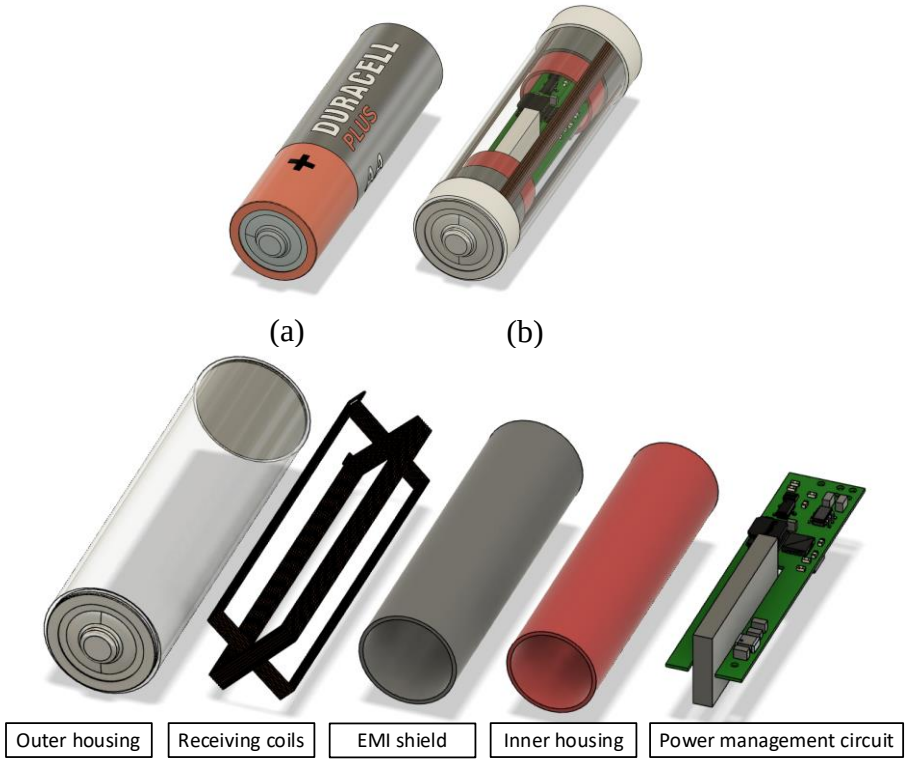

(a) (b)

(c)

Fig. 3.1. 3D models of (a) an AA battery, (b) complete, and (c) disassembled AAPRU prototype.

shown in Fig. 3.2, consists of the tuning network, diode rectifier, and battery charging IC, back-up battery, and dc-dc converter. The tuning network sets the resonance frequency of the Rx coil, which is near the operating frequency. The diode rectifier is used to convert ac currents into dc currents supplying power to the load. The IC regulates the charging characteristics of a small rechargeable battery. The back-up battery is used to ensure a well-regulated voltage and continuous power supply to the load when the consumer device is moved out of the magnetic field. Finally, the dc-dc converter steps down the battery voltage to the required value, which typically is 1.5V for AA batteries. Inner and outer housings are used for protecting electronic components, supporting the coil structure, and creating

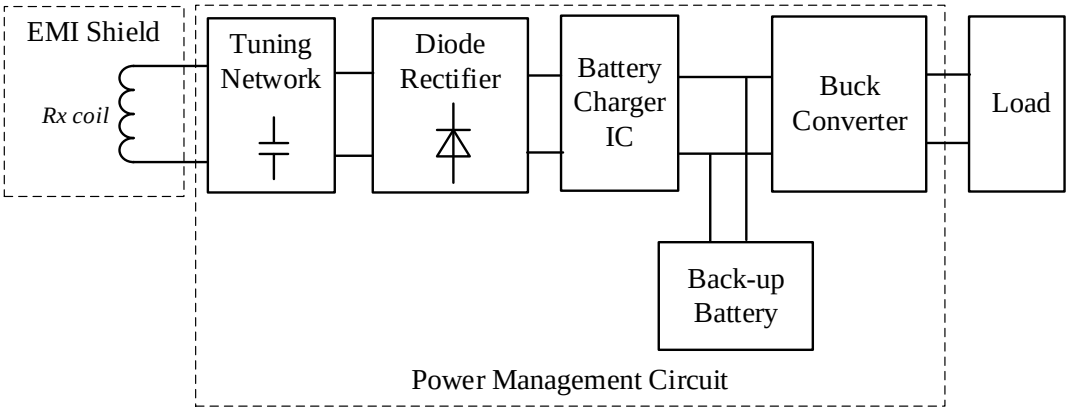

Fig. 3.2. Simplified block diagram of the power management circuit of the AAPRU.

the overall cylindrical shape for the AAPRU. A flexible ferrite sheet is wrapped around the inner housing to protect the circuit from the EMI by redirecting stray magnetic flux away from the printed circuit board (PCB).

3.2 Receiving Coil

Typical consumer electronics applications like smartphones are generally wirelessly charged while placed flat on the charging pad. That means the magnetic flux flows through embed receiving coils predominately at an angle of 90°, which favors the planar-spiral coil structure. However, the proposed AAPRU has a cylindrical shape allowing it to be placed in the battery holder at any angle. This physical structure provides great convenience for users but also introduces a challenge in designing a coil that must maintain strong coupling in the full rotational range. A dual-coil structure is proposed to address this issue.

3.2.1 Receiver Coil Structure

Fig. 3.3 shows the proposed dual-coil structure consisting of two identical rectangular coils placed perpendicular to each other. These coils have overlapped longitudinal x-axes and separate leads. They are connected to two different diode rectifiers on the PCB, as shown in Fig. 3.4, allowing ac in each coil to be rectified separately. As a result, the combined output current stays nearly constant when the AAPRU is rotated around the x-axis. The position where the AAPRU's x-axis is placed perpendicular to the ground is not considered in this work as it is not common in consumer devices.

The close-up geometry of an exemplary individual coil is shown in Fig. 3.5, where w, l, and h are the width, length, and height of the coil, respectively. N_{turn} is the number of turns, p is the pitch between adjacent turns, and d is the diameter of the wire. The rectangular shape is chosen to maximize the coil's enclosed area by utilizing the outer boundary of the battery volume. Without magnetic cores, there is a substantial space in the

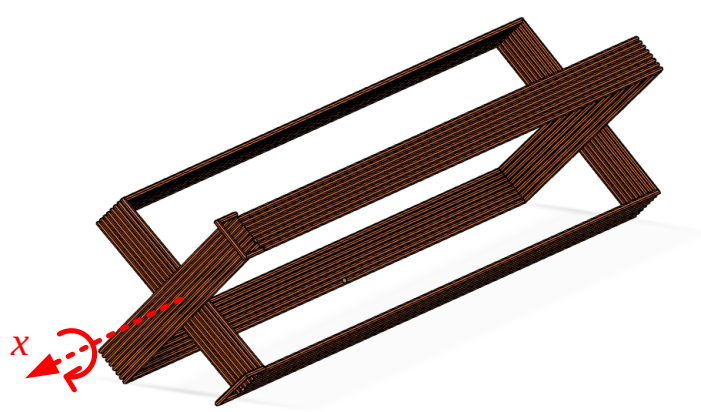

Fig. 3.3. Dual-coil structure of the receiving coils.

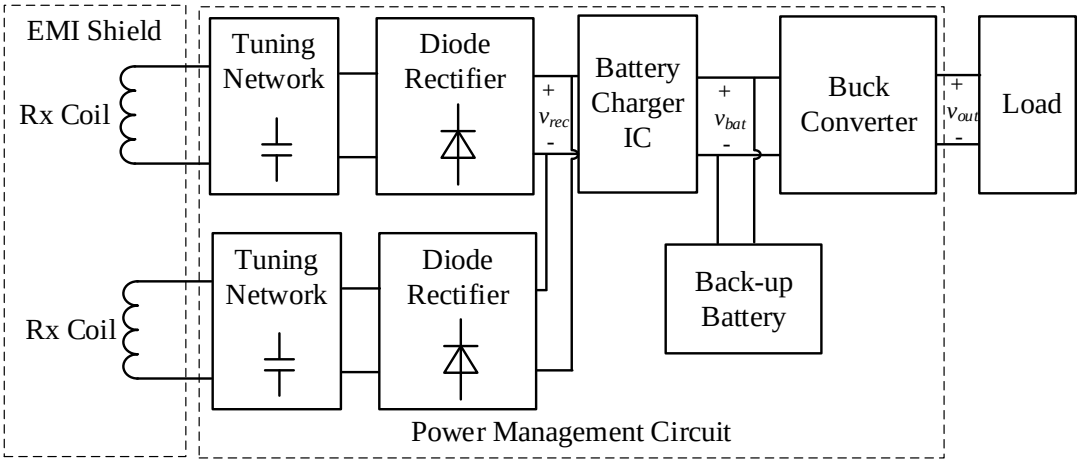

Fig. 3.4. Block diagram of the AAPRU power management circuit connected with dual-coil setup.

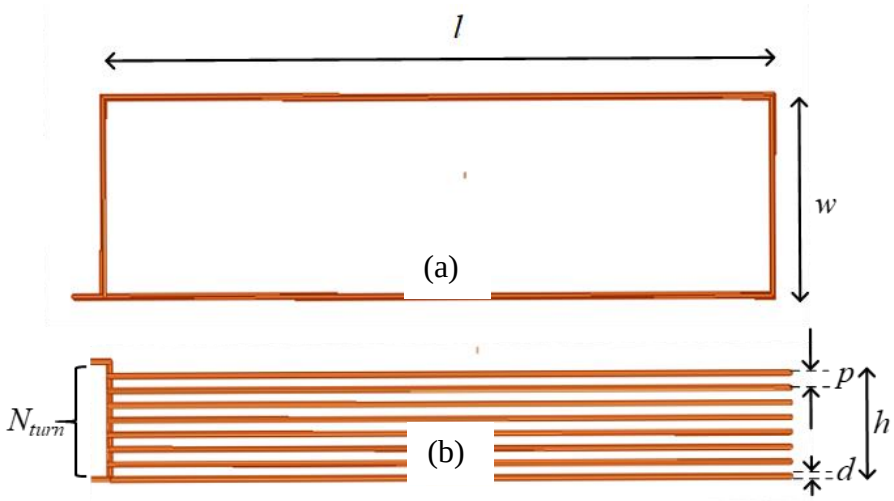

Fig. 3.5. Geometry of the proposed individual coil in (a) top view and (b) side view.

center for placing the power management system. The windings are made of one layer of round copper wire uniformly wound around a cylindrical housing. The windings are coated with a thin enamel insulation layer. For simplicity, the coil curvature on the side is neglected. This assumption is justified when the coil height is much smaller than the housing diameter.

3.2.2 Induced Voltage

The magnetic field generated from the transmitter coil is assumed to be uniform over the coil winding area $A = wl$. According to Faraday's law of induction, the induced voltage v_m of the individual Rx coil is dependent on the rate of change of magnetic flux passing through the loop interior

$$v_m(t) = -N_{turn}\frac{d\Phi_B(t)}{dt}. \tag{3.1}$$

The magnetic flux Φ_B is

$$\Phi_B(t) = \vec{B} \cdot \vec{A} = BAcos\theta, \tag{3.2}$$

where B is the magnetic flux density, A is the coil area, and θ is the angle between $\vec{B}$ and the normal area vector, $\vec{A}$, as labeled in Fig. 3.6.

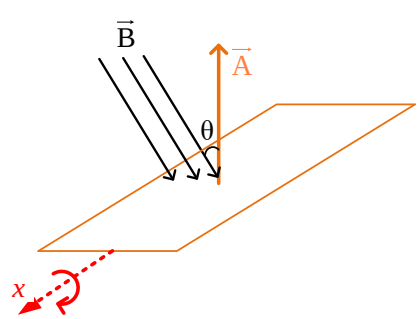

Fig. 3.6. Magnetic flux through the coil area.

For a single rectangular coil, when the coil is positioned so that $\vec{A}$ is parallel to the charging surface, $\theta = 90°$ or $270°$, the magnetic field normal to the coil surface is zero. As a result, there is no magnetic flux flowing through the receiver coil enclosed area, leading to zero induced voltage. That means the AAPRU with a single rectangular coil does not work in the full range of θ. The plot in Fig. 3.7 demonstrates zero induced voltage magnitude at $\theta = 90°$ and $270°$.

Adding the second coil in the dual-coil setup helps maintain the substantial total flux going through the coil enclosed surface at these "dead angles." Fig. 3.8 shows the magnitude of $v_m(t)$ in two example coils with varying θ. At $\theta = 90°$ or $270°$, where $|v_{m1}(t)|$ is zero, $|v_{m2}(t)|$ is maximum, indicating that the total induced voltage from two coils at these operating angles is non-zero.

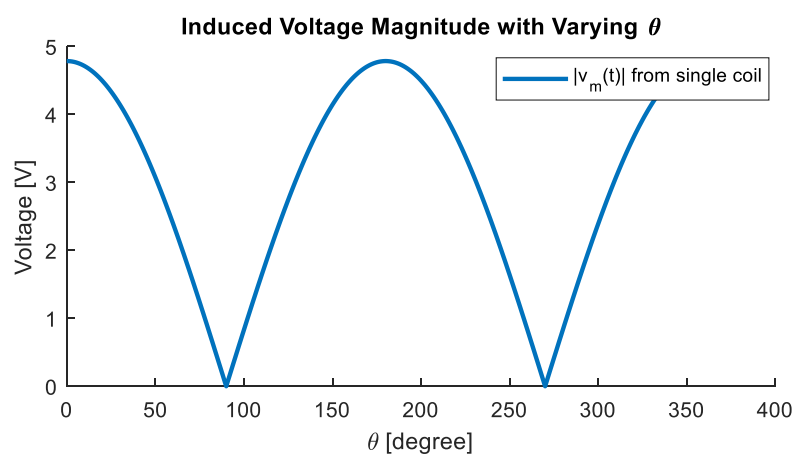

Fig. 3.7. Simulated induced voltage magnitude with varying θ in an example single rectangular coil.

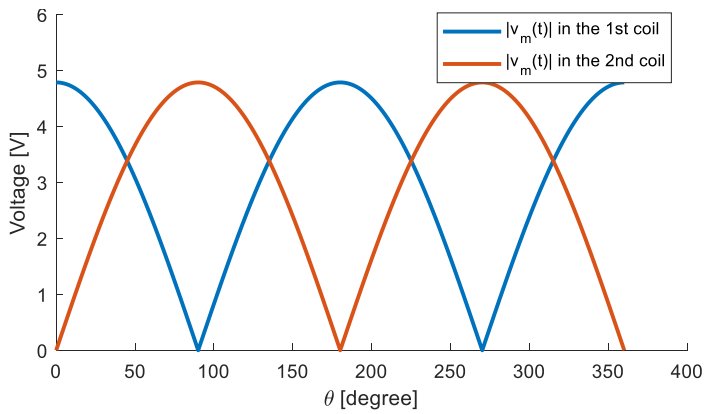

Fig. 3.8. Simulated induced voltage magnitude in open-circuited dual coils.

3.2.3 Coil Inductance

The self-inductance of a coil is affected by nearby conductive objects [44]. Since two coils are placed close to each other, the presence of the other coil needs to be taken into account when calculating the coil inductance. The finite-element method (FEM) simulation is utilized to examine this effect. Fig. 3.9a and Fig. 3.9b show the simulated magnetic flux distribution from two identical example coils excited with the same current. Coil A (Fig. 3.9a) is placed in free space, and coil B (Fig. 3.9b) is placed in the dual-coil setup. The simulated magnetic flux distribution from two coils is nearly identical, indicating that their inductance values are the same.

The equation in [45] is used to calculate the inductance of the rectangular coil

$$L = N_{turn}^2 \frac{\mu_o \mu_r}{\pi} \left[-1.75(w+l) + 2\sqrt{l^2+w^2} - l\, ln\left(\frac{l+\sqrt{l^2+w^2}}{w}\right) - w\, ln\left(\frac{w+\sqrt{l^2+w^2}}{l}\right) + l\, ln\left(\frac{2l}{d/2}\right) + w\, ln\left(\frac{2w}{d/2}\right)\right], \tag{3.3}$$

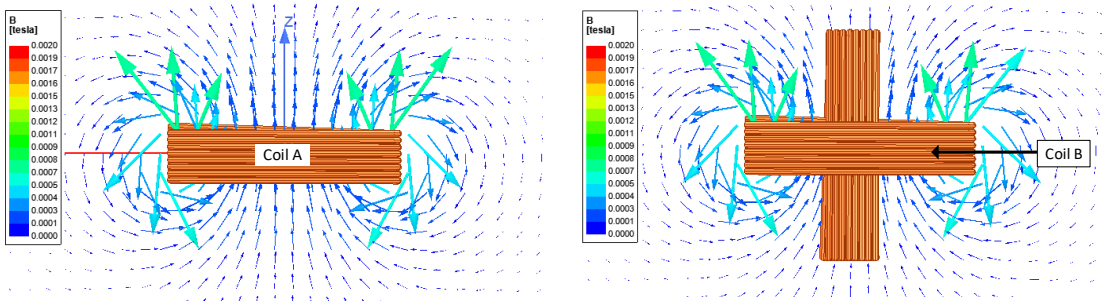

(a) (b)

Fig. 3.9. Simulated magnetic flux distribution from example coils.

where $\mu_o = 4\pi \times 10^{-7}\mathrm{H/m}$ is the permeability of free space and $\mu_r = 1$ is the relative permeability.

3.2.4 Coil Capacitance

The receiving coil is designed with a minimal pitch to minimize the coil volume, meaning that coil turns are in proximity to each other. Consequently, the parasitic capacitance between adjacent turns must be modeled to accurately calculate the equivalent impedance of the coil at 6.78 MHz. The capacitance model of a single-layer rectangular coil is shown in Fig. 3.10, where C_t is the turn-to-turn capacitance. Note that the parasitic capacitances between nonadjacent turns are neglected in the model.

An analytical approach established in [46] is used to calculate C_t where the effect of the insulation coating on windings is also taken into account,

$$C_t = \frac{2\pi\epsilon_0(w+l)}{\ln\left(F + \sqrt{F^2 - (1+t/r)^{2/\epsilon_r}}\right)}, \tag{3.4}$$

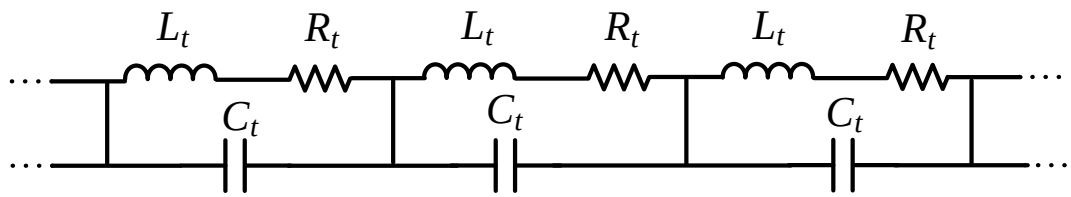

Fig. 3.10. Parasitic capacitance model of the rectangular coil.

where,

$$F = \frac{p/d}{\left(1 + \frac{t_{coat}}{r}\right)^{1-1/\epsilon_r}} \tag{3.5}$$

t_{coat} is the thickness of the insulation coating, ϵ_0 is the permittivity of free space, ϵ_r is the permittivity of the coating, and r is the wire radius.

From the circuit in Fig. 3.10, the equivalent RLC model of the Rx coil is shown in Fig. 3.11a. From that, an equivalent RL model shown in Fig. 3.11b is obtained, which is the final model used to calculate the coil equivalent inductance L_s at 6.78 MHz. Equivalent parameters are calculated as follows,

$$L = N_{turn} L_t, \tag{3.6}$$

$$R = N_{turn} R_t, \tag{3.7}$$

$$C = \frac{C_t}{N_{turn} - 1}. \tag{3.8}$$

$$L_s = L - \frac{1}{\omega^2 C}. \tag{3.9}$$

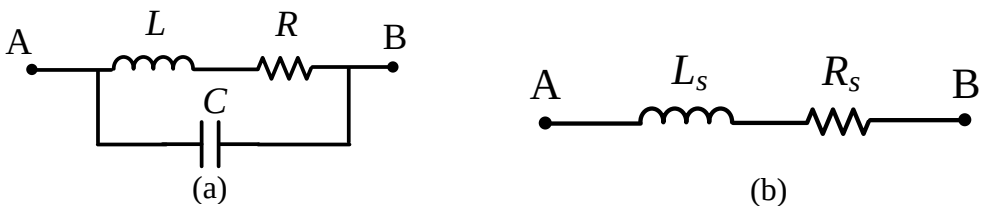

Fig. 3.11. (a) RLC model, and (b) RL model of the Rx coil.

3.2.5 Coil Resistance

At 6.78 MHz, the winding resistance of coils with a small wire cross-sectional area is large, and significantly increased due to the skin and proximity effect, deteriorating the system efficiency. The skin effect is the phenomenon where the alternating current concentrates on the conductor surface instead of uniformly distributing the entire conductor cross-section, resulting in a smaller effective conducting area and increased copper resistance. The skin depth δ is defined as the distance measured from the conductor's outer layer to an inner level, where most of the alternating current is constrained [47],

$$\delta = \sqrt{\frac{\rho}{\pi f_s \mu_r \mu_0}}. \tag{3.10}$$

Proximity effect occurs in an array of closely-placed conductors carrying ac currents, e.g., the proposed coil. The magnetic field generated from an alternating current in one turn induces eddy currents on adjacent turns, altering the current distribution. Consequently, the ac copper resistance R_{ac} is increased significantly and proportional to the current frequency. Based on Dowell's approximation approach for finding R_{ac} [48], which has been validated in many studies [49], [50], the inductor ac resistance due to the skin and proximity effect is obtained

$$R_{ac} = R_{dc}\alpha\left\{\frac{e^{2\alpha} - e^{-2\alpha} + 2\sin(2\alpha)}{e^{2\alpha} + e^{-2\alpha} - 2\cos(2\alpha)} + \frac{2(m^2-1)}{3}\frac{e^{\alpha} - e^{\alpha} - 2\sin(\alpha)}{e^{\alpha} + e^{\alpha} + 2\sin(\alpha)}\right\}. \quad (3.11)$$

The factor α is

$$\alpha = \left(\frac{\pi}{4}\right)^{\frac{3}{4}} \frac{d^{\frac{3}{2}}}{\delta\sqrt{p}}, \quad (3.12)$$

where $R_{dc} = \rho l_w / A$ is the coil dc resistance, l_w is the winding length, A is the cross-sectional area of the coil, and m is the number of layers of the winding.

3.3 Multiphase Voltage-Doubler Diode Rectifier Modeling

A two-phase voltage-doubler diode rectifier is used to convert ac flowing through each Rx coil into dc to supply power to the battery charger IC. Fig. 3.12 shows the circuit schematic of the proposed rectifier. Diode rectifiers are preferred over active rectifiers in this application because of their small volume, and simple design as gate drivers are not needed. The second phase leg of the rectifier is connected to an additional transistor Q_1

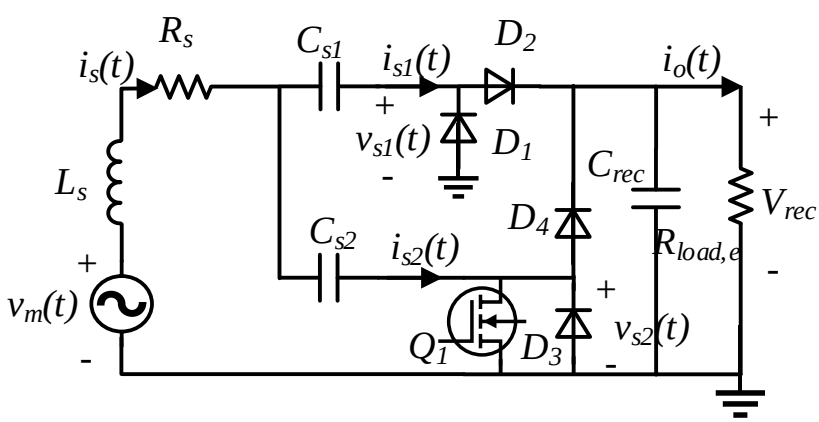

Fig. 3.12. Proposed diode rectifier circuit with an automatic tuning network.

used for the tuning mechanism, which is discussed in the next section. During normal operation, Q_1 is turned off, allowing both phase legs to deliver power to the load. The induced voltage $v_m(t)$ from a constant-current transmitter [18] is modeled as the input source for the rectifier circuit. L_s, R_s, and $C_{s,i}$ are Rx coil inductance, equivalent series resistance (ESR), and tuning capacitance in phase leg i. $i_s(t)$ is the secondary (input) current, $v_{s1}(t)$ and $v_{s2}(t)$ are the switch node voltages.

To simplify the design, tuning capacitors C_{s1} and C_{s2} are set to be equal. Also, diodes used in each rectifier are identical, resulting in similar switch node voltages $v_{s1}(t)$ and $v_{s2}(t)$. Leveraging this similarity, only the top phase leg is analyzed. The example waveforms in the top phase leg are shown in Fig. 3.13. There are four intervals per period. Intervals I and III are switching transitions, where $i_{s1}(t)$ charges and discharges the diode parasitic capacitance. As a nature of the voltage-doubler diode rectifier, interval II is the

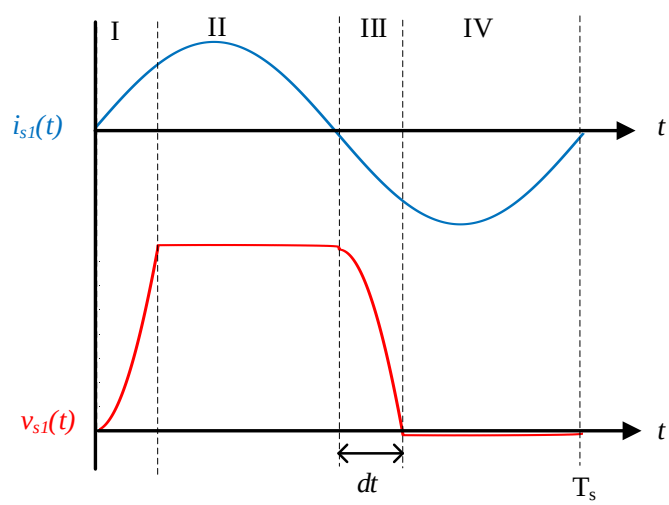

Fig. 3.13. Example waveforms per switching period.

only power-delivery interval where D_2 conducts, allowing the current to deliver power to the load.

The proposed circuit at steady state can be modeled by the ac equivalent circuit shown in Fig. 3.14. Capital bold letters, e.g., $\mathbf{I}_s$, $\mathbf{V}_m$, $\mathbf{V}_{s1}$, and $\mathbf{V}_{s1}$ represent phasor quantities of the first-order harmonic of the corresponding waveforms.

The equivalent rectifier (load) impedance $Z_{rec,i} = jX_{rec,i} + R_{rec,i}$ is not purely resistive. At 6.78 MHz, the switching transition can take a large portion in the total switching period, resulting in a substantial capacitive load, so $X_{rec,i}$ has a non-negligible negative value. If the rectifier is modeled as purely resistive $X_{rec,i} = 0$, the load reactance $X_{rec,i}$ is not fully compensated, causing a significant degradation in the power transfer efficiency [51]. The analytical approach proposed in [52], where the diode capacitance is taken into account, is applied to find $Z_{rec,i}$. For clarification, the following analysis refers to only the top phase leg of the rectifier.

During switching transitions, the total charge supplied to diode capacitance is

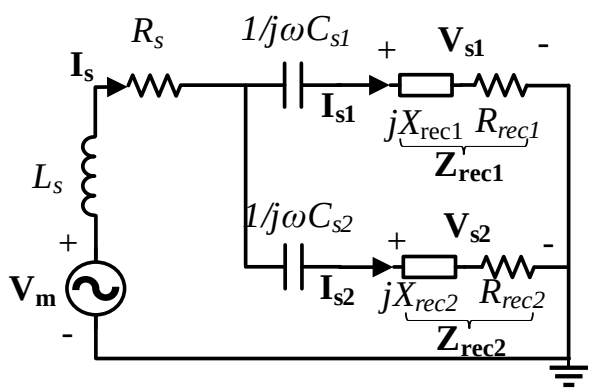

Fig. 3.14. AC equivalent circuit of the diode rectifier in steady-state.

$$Q_{d,total} = 2C_d V_{rec} = \int_0^{dt} I_{s1} \sin(\omega_s t)\, dt, \tag{3.13}$$

where C_d is the parasitic capacitance of a single diode, V_{rec} is the steady-state rectified voltage, and dt is the transition time. Since there are two diodes per phase leg, $Q_{d,total}$ equals two times the charge supplied to each diode $Q_d = C_d V_{rec}$. The delivered power from the top phase leg in interval II is

$$P_{rec1} = \frac{1}{T_s} \int_{dt}^{T_s/2} V_{rec} I_{s1} \sin(\omega_s t) dt. \tag{3.14}$$

The power loss due to the voltage drop on the diode in intervals II and III is

$$P_{loss1} = 2\frac{2}{T_s} \int_{dt}^{T_s/2} v_f(t) I_{s1} \sin(\omega_s t) dt. \tag{3.15}$$

The voltage drop v_f on the diode is modeled as

$$v_f(t) = V_{d,o} + R_d I_{s1} \sin(\omega_s t), \tag{3.16}$$

where $V_{d,o}$ is the diode barrier voltage and R_d is the diode internal resistance. Then the total input power is

$$P_{in1} = P_{rec1} + P_{loss1}. \tag{3.17}$$

From (3.13) and (3.14), the analytical expressions of I_{s1} and dt are

$$I_{s1} = \frac{Q_{d,total}\omega_s}{2} + \frac{\pi P_{rec1}}{V_{rec}}, \tag{3.18}$$

$$dt = \frac{\cos^{-1}\left(\frac{I_{s1} - \omega_s Q_{d,total}}{I_{s1}}\right)}{\omega_s}. \tag{3.19}$$

The piecewise switch node voltage $v_{s1}(t)$ in each interval is

$$v_{s1}(t) = \begin{cases} \int_0^t \frac{I_{s1}\sin(\omega_s t)}{2C_d}\,dt & 0 < t \le dt \\ V_{rec} + V_{d,o} + R_d I_{s1}\sin(\omega_s t) & dt < t \le T_s/2 \\ V_{rec} + \int_{T_s/2}^{T_s/2+dt} \frac{I_{s1}\sin(\omega_s t)}{2C_d}\,dt & T_s/2 < t \le T_s/2 + dt \\ -V_{d,o} + R_d I_{s1}\sin(\omega_s t)\,dt & T_s/2 + dt < t \le T_s \end{cases}. \quad (3.20)$$

Fourier analysis is employed to obtain the fundamental component of $v_{s,eq}(t)$

$$v_{s1}^{(1)}(t) = a_o + a_1\cos(\omega_s t) + b_1\sin(\omega_s t), \quad (3.21)$$

where

$$a_o = \frac{1}{T_s}\int_0^{T_s} v_{s1}(t)dt, \quad (3.22)$$

$$a_1 = \frac{2}{T_s}\int_0^{T_s} v_{s1}(t)\cos(\omega_s t)dt, \quad (3.23)$$

$$b_1 = \frac{2}{T_s}\int_0^{T_s} v_{s1}(t)\sin(\omega_s t)dt. \quad (3.24)$$

Then the root mean square (RMS) value of $v_{s1}^{(1)}(t)$ is calculated

$$V_{s1,rms} = \sqrt{a_o^2 + \frac{1}{2}(a_1^2 + b_1^2)}. \quad (3.25)$$

The input power is also calculated using RMS values

$$P_{in1} = V_{s1,rms} I_{s1,rms}\cos(\phi_{rec1}) = \frac{I_{s1}^2}{2}|\mathbf{Z}_{rec1}|\cos(\phi_{rec1}). \quad (3.26)$$

$\phi_{rec1} = \phi_{v_{s1}} - \phi_{i_{s1}}$ denotes the phase difference between $i_{s1}(t)$ and $v_{s1}(t)$, which is also derived from (3.17) and (3.26)

$$\phi_{rec1} = \arccos\left(\frac{\sqrt{2}(P_{rec1} + P_{loss1})}{V_{s1,rms} I_{s1}}\right). \quad (3.27)$$

Substituting (3.17) into (3.26) also yields the rectifier equivalent impedance Z_{rec}

$$Z_{rec1} = R_{rec1} + jX_{rec1} = \frac{2(P_{rec1} + P_{loss1})}{I_{s1}^2}\left(\frac{\cos\phi_{rec1} - j\sin\phi_{rec1}}{\cos\phi_{rec1}}\right). \quad (3.28)$$

After the rectifier impedance per phase leg is found, the total equivalent impedance in both phases is

$$C_{s,eq} = 2C_{s1} = 2C_{s2}, \quad (3.29)$$

$$R_{rec,eq} = \frac{R_{rec1}}{2} = \frac{R_{rec2}}{2}, \quad (3.30)$$

$$X_{rec,eq} = \frac{X_{rec1}}{2} = \frac{X_{rec2}}{2}. \quad (3.31)$$

In order to compensate for the equivalent load reactance $X_{rec,eq}$, the total reactance on the receiver is nulled,

$$j\omega L_s + \frac{1}{j\omega C_{s,eq}} + jX_{rec,eq} = 0. \quad (3.32)$$

Then $C_{s,1}$ and $C_{s,2}$ are derived from (3.29) and (3.32),

$$C_{s1} = C_{s1} = \frac{1}{2(\omega^2 L_s + \omega X_{rec,eq})}. \quad (3.33)$$

Using the analysis above, the tuning capacitance C_{s1} and C_{s2} are accurately selected to compensate for both coil inductance L_s and load reactance $X_{rec,eq}$, resulting in improved power transfer efficiency.

3.4 Automatic Tuning Network

The automatic tuning network is designed to protect the battery charging IC from overvoltage and increase its input operating range. The simplified block diagram of this tuning scheme is shown in Fig. 3.15 and its principle is described as follows. A Schmitt

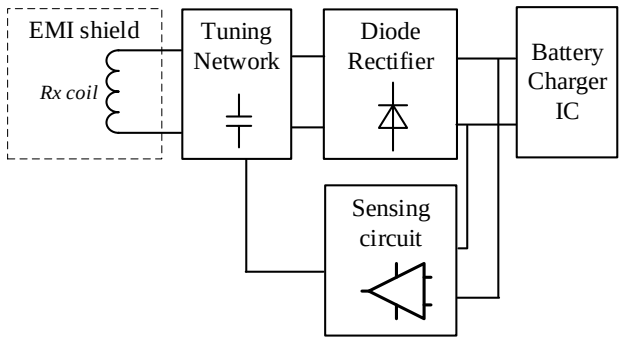

Fig. 3.15. Block diagram of the tuning network.

trigger is employed to sense the IC input voltage. When the sensed voltage exceeds the trigger value, the trigger turns on the switch Q_1, shunting the second tuning capacitor C_{s2} to the ground. As a result, the equivalent tuning capacitance $C_{s,eq}$ is changed, meaning the total reactance is no longer zero ($X_s \neq -X_{rec,eq}$). Thus, the amplitude of $i_s(t)$ is reduced, decreasing the output voltage of the rectifier, which is also the input voltage of the IC. Fig. 3.16 shows the ac equivalent circuit when Q_1 is on.

The Schmitt trigger is an active comparator that converts an analog signal to a digital signal. Its inherent hysteresis is leveraged to make the comparator more tolerant to slow and noisy inputs. This characteristic is useful for preventing false triggering when the comparator's input signal is impacted by the triggering actions, as in this circuit. Fig. 3.17 shows the configuration of the non-inverting Schmitt trigger used in this circuit.

The upper and lower trigger points at the input, V_{UTP} and V_{LTP}, are set by selecting appropriate resistance values

$$V_{UTP} = V_{ref}\frac{R_1 + R_2}{R_2} - V_{OL}\frac{R_1}{R_2}, \tag{3.34}$$

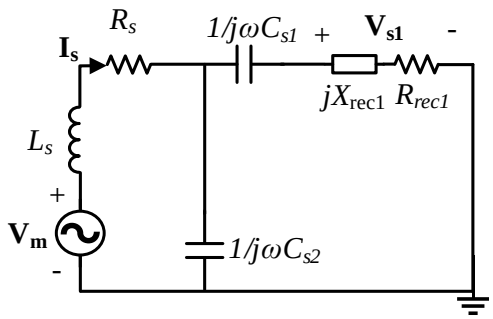

Fig. 3.16. AC equivalent circuit when Q_1 is on.

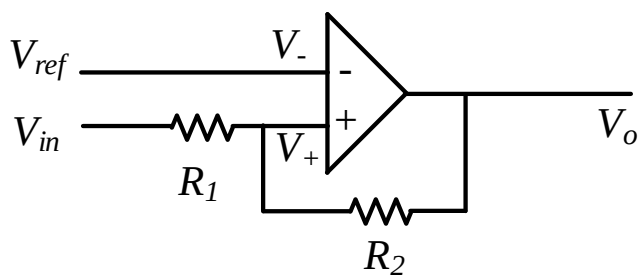

Fig. 3.17. Non-inverting Schmitt trigger schematic.

$$V_{LTP} = V_{ref}\frac{R_1 + R_2}{R_2} - V_{OH}\frac{R_1}{R_2}, \tag{3.35}$$

where V_{OH} and V_{OL} are high and low output voltage levels of the trigger, respectively. Using equations (3.34) and (3.35), R_1 and R_2 are chosen to set the trigger value of V_{rec} (close to the IC's maximum input votlage) where Q_1 is turned on detuning the circuit to protect the IC from overvoltage.

3.5 Prototype

A functional prototype of the 6.78 MHz AAPRU is built to validate the coil model, rectifier design, and tuning scheme operation.

3.5.1 Receiving Coil

The prototype of the dual-coil structure is shown in Fig. 3.18. They are fabricated in the lab by wrapping a small magnetic wire around a 3D-printed rectangular mold. Dimensions of a single Rx coil are listed in Table 3.1. The coil prototype is connected to the E4990A impedance analyzer to measure L_s and R_s values at 6.78 MHz. Table 3.2 lists prototype parameter values, showing a good agreement between the measurement and calculation. The calculated L_r is off by 8 % from the measured value.

3.5.2 PCB

Fig. 3.19 illustrate the 3D model and prototype of the PCB. Components used in the prototype circuit are given in Table 3.3.Because the existing battery holder in consumer

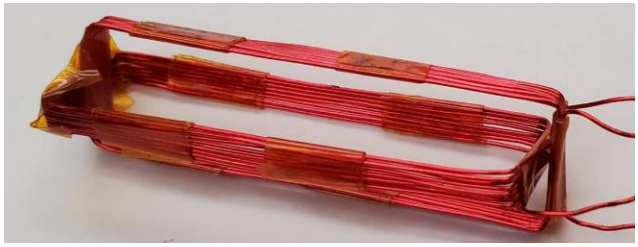

Fig. 3.18. A prototype of receiving coils.

Table 3.1. Receiving coil dimensions.

Parameters	**Symbol**	**Value**
Number of turns	N_{turn}	8
Coil width	w	13 mm
Coil length	l	46 mm
Coil height	h	2 mm
Distance between adjacent turns	p	0.1 mm
Winding AWG	AWG	28
Winding diameter	d	0.321 mm

Table 3.2. Coil parameter values.

Parameters	**Symbol**	**Measured value**	**Calculated value**
Rx coil inductance	L_s	5.4μH	5.83 μH
Rx coil resistance	R_s	1.815Ω	2.02 Ω
Rx tuning capacitance	C_{s1}, C_{s2}	68pF	
Transmitter coil inductance	L_p	16.194 μH	
Primary tuning capacitance	C_p	53 pF	
Transmitter coil resistance	R_p	1.05 Ω	
Coupling coefficient	k	0.0291	
Distance between coils	d_c	2 cm	

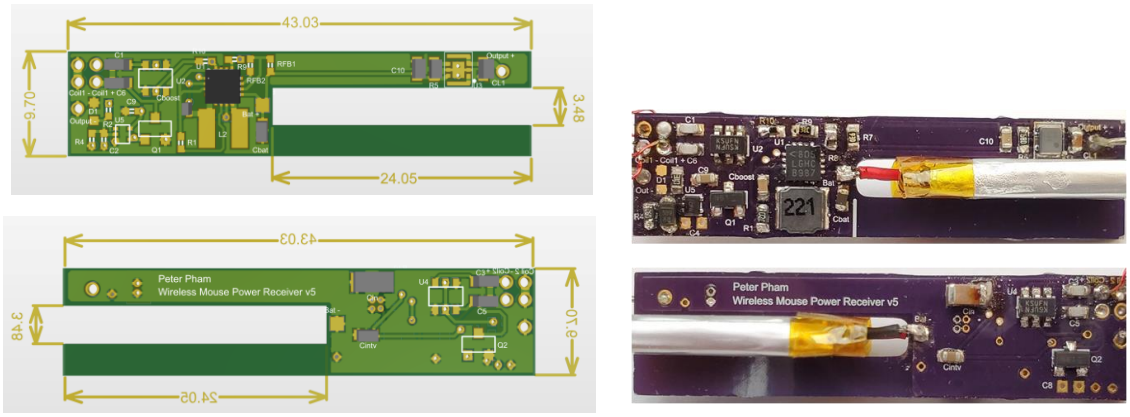

(a) (b)

Fig. 3.19. (a) 3D model and (b) prototype of the PCB containing the power management circuit.

Table 3.3. AAPRU prototype circuit components.

Component	Part
Diode array	SD103ASDM
Battery charger IC	LTC4121
Buck converter	XCL206B153AR-G (1.5V)
Schmitt trigger	SN74LVC1G14
Switch Q_1	DMN6140L-7

applications strictly limits the allowable area of the PCB, it must be designed to have a compact size. One of the strategies for reducing the PCB size is to utilize both top and bottom layers for placing rectification components connected to each Rx coil. Specifically, two sets of the multiphase diode rectifiers, tuning capacitors, tuning switches, and Schmitt triggers are placed on opposite sides of the board.

To further reduce the PCB size, two SD103ASDM rectifier array ICs are selected instead of eight single diodes. Furthermore, all selected components are surface mount components with small footprints, e.g., 0402 and 0603 packages. Another size-saving design is the cut slot on the right side of the PCB serving as a battery holder, where the battery is placed perpendicular to the PCB surface, saving more space and allowing a bigger back-up battery.

3.5.3 Housing

Fig. 3.20a and Fig. 3.20b show 3D models of the inner and outer cylindrical housing with labeled dimensions. The inner housing has a similar shape to the standard AA battery, but with a slightly smaller diameter. To enable rapid prototyping and provide design flexibility, the inner housing is 3D printed using the Lulzbot Taz 6 3D printer.

The outer housing (cover) is fabricated using the stereolithography (SLA) Form 2 3D Printer. There are some advantageous features of SLA printing that makes it suitable for fabricating the outer housing. First, the smooth surface finish is desirable for commercializing the product and improving the consumer’s experience. Second, transparent and flexible SLA material is used for visualization purposes.

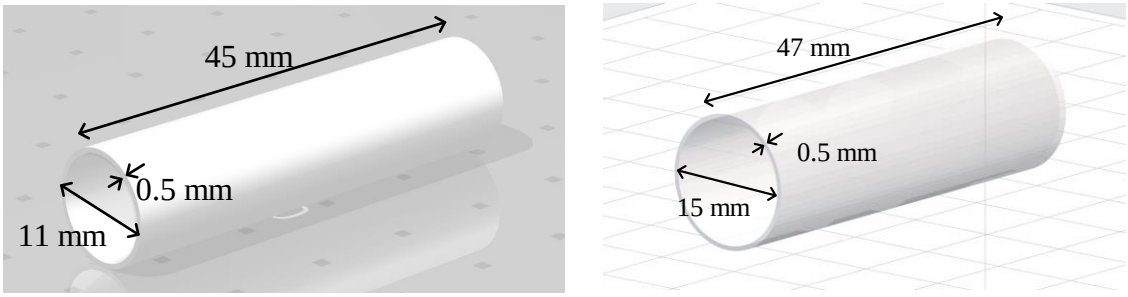

Fig. 3.20. 3D models of the plastic (a) inner housing, and (b) outer housing.

3.5.4 EMI Shield

In order to protect electronic components from the EMI, a magnetic shield is required to block the magnetic flux from interfering with those components. Typically, a shielding layer is added to the bottom of the PCB. However, since the PCB is placed at the coil center, this shielding layer also blocks the magnetic flux from passing through coils, leading to the significant degradation in the coil coupling. Therefore, a shielding technique is used, where a flexible ferrite sheet is wrapped around the plastic inner housing, underneath the coil layer. The 3D model and prototype of the proposed EMI shield are shown in Fig. 3.21a and Fig. 3.21b.

Because ferrite material is highly permeable, it absorbs and redirects the magnetic flux around the housing's outer surface. As a result, the magnetic flux can pass through receiving coils without penetrating electronic components. Furthermore, by concentrating more magnetic flux through the coil, this shielding technique also increases the coil coupling coefficient. Fig. 3.22 demonstrates that the simulated magnetic field inside the shielded plastic housing is much lower compared to that of the unshielded housing, which

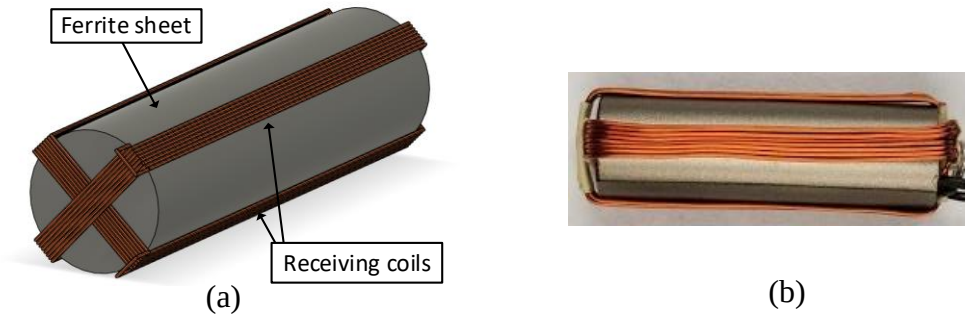

Fig. 3.21. (a) 3D model, and (b) prototype of the EMI shield.

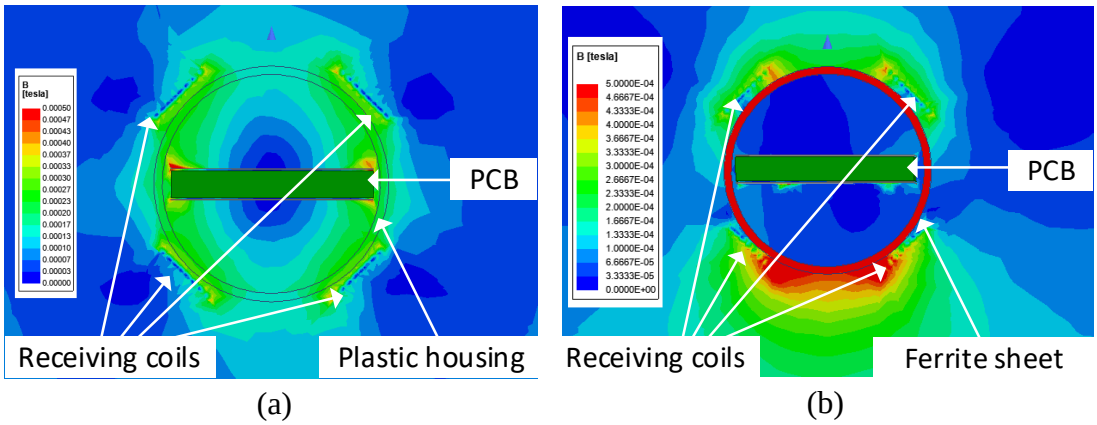

Fig. 3.22. Cross-sectional view of the simulated magnetic field inside (a) the unshielded housing, and (b) the shielded housing.

validates the effectiveness of this shielding technique. The selected sheet for the prototype is the FFAM10, which has a thickness of 0.25 mm and low imaginary permeability for reducing the hysteresis loss. Fig. 3.23 shows the final product consisting of all layers and an example setup with the wireless mouse. The cost breakdown of the AAPRU prototype is given in Table 3.4. The total cost is estimated to be $17.25, which is higher than a standard AA. However, the higher price can be justified since it has a longer life span and wireless charging capability.

3.6 Experimental Verification

In order to validate the proposed design and model of the AAPRU, experiments are carried out for testing the prototype. The actual and block diagram of the experimental setup are shown in Fig. 3.24 and Fig. 3.25, respectively. The operating conditions and equipment part numbers are listed in Table 3.5 and Table 3.6, respectively.

The transmitting coil is excited by the current generated from the power amplifier, which is driven by the function generator. The function generator is used to output a 6.78 MHz sinusoidal signal to the power amplifier. The signal amplitude is then increased depending on the gain setting of the power amplifier. The AAPRU is placed on top of the transmitting coil, where energy is wirelessly transferred via the magnetic field. An electronic load is connected to the output terminal of the AAPRU and set to be constant resistance. Experimental operating waveforms of the diode rectifier in the prototype are captured by the oscilloscope (Fig. 3.26a) and compared with modeled waveforms (Fig. 3.26b) generated in MATLAB. $v_{s1}(t)$ and $v_{s2}(t)$ are seen to be lagging $i_s(t)$ by a considerable phase, implying the equivalent rectifier impedance is capacitive due to the

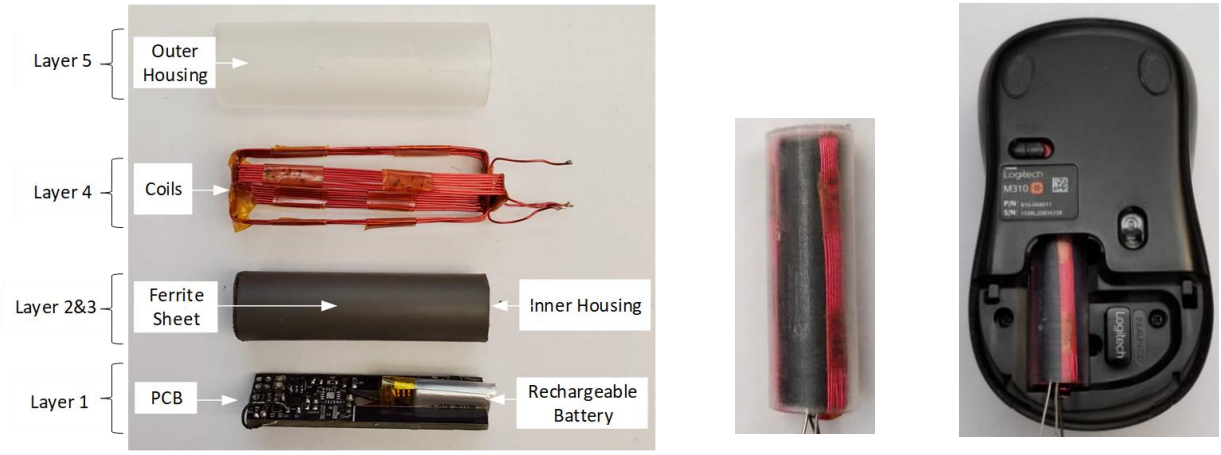

(a) (b) (c)

Fig. 3.23. (a) Prototypes of all AAPRU layers, (b) complete AAPRU prototype, and (c) an example application with a wireless mouse.

Table 3.4. Cost breakdown of the AAPRU prototype.

Component	Cost
3D printed housing	$1
PCB	$1.5
Receiving coils	$0.25
Electronics components	$5
Back-up battery	$4.5
EMI shield	$5
Total	$17.25

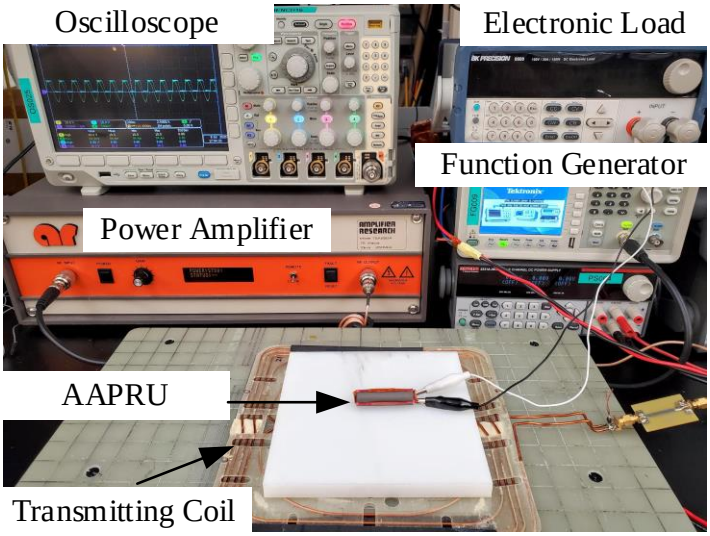

Fig. 3.24. Experimental setup for testing the AAPRU.

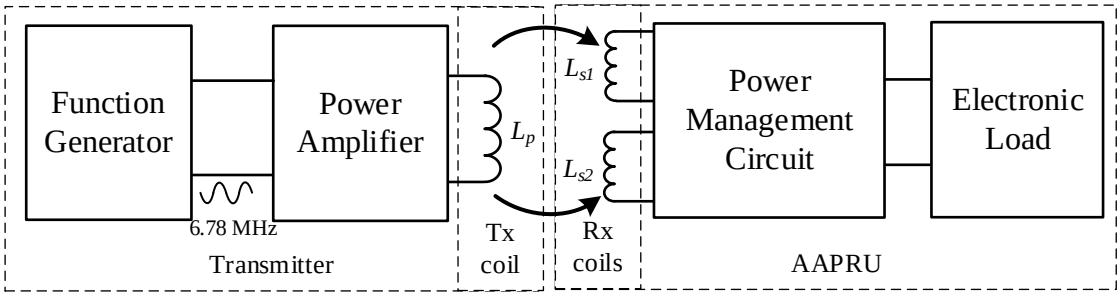

Fig. 3.25. Block diagram of the experimental setup.

Table 3.5. AAPRU operating conditions.

Parameter	Value
Rectifier output voltage/IC input voltage	10 V
Battery voltage	3.7 V
Battery charge current	50 mA
Output voltage	1.5 V

Table 3.6. Equipment part numbers.

Equipment	Part number
Power amplifier	75A250A
Function generator	AFG1062
Electronic load	BK Precision 8600
Oscilloscope	MDO3104

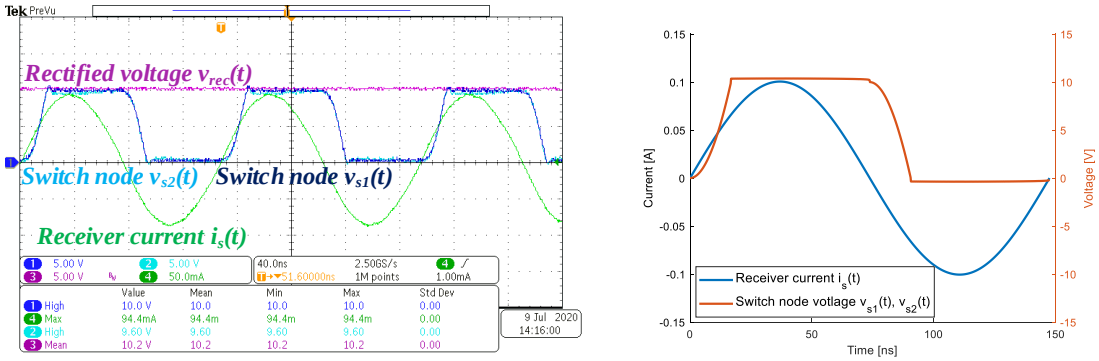

Fig. 3.26. (a) Experimental and (b) modeled operating waveforms of the AAPRU.

diode parasitic capacitance. The agreement between these waveforms verifies the accuracy of the presented modeling approach for the multiphase diode rectifier.

In the second test, the transmitting current is increased from 0 A to nearly 900 mA. Measured voltages, including the rectified voltage v_{rec}, back-up battery voltage v_{bat}, and the output voltage v_{out}, are recorded by the oscilloscope and shown in Fig. 3.27. All of these voltage levels are well regulated at expected values listed in Table 3.5, which validates the functionality of the AAPRU.

3.7 Summary

A wireless power receiving unit used to replace AA batteries in low-power consumer electronics applications is proposed in this chapter. A functional prototype with the proposed structure is built to validate the design. The dual-coil structure is utilized to maintain the output current over a full rotational range. The multiphase voltage-doubler

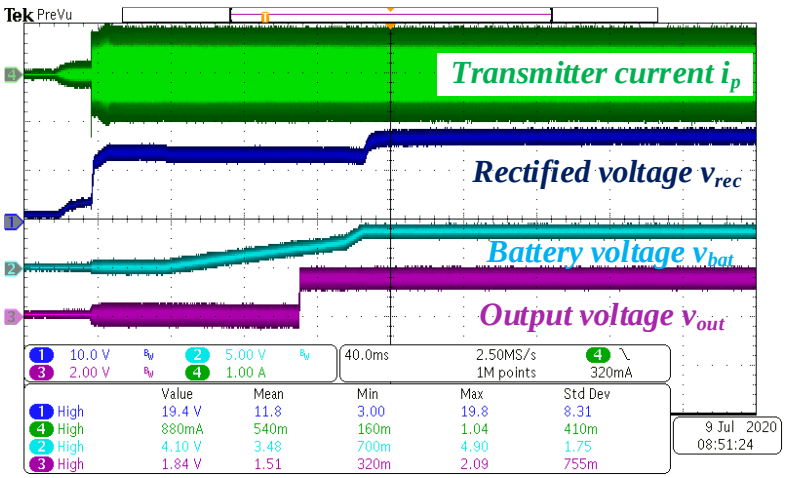

Fig. 3.27. Experimental signals showing the functionality of the AAPRU prototype.

diode rectifier is accurately modeled to find the equivalent load impedance and facilitate the compensation process.

Chapter Four

SYNCHRONOUS ACTIVE RECTIFIER

This chapter is focused on designing a ZVS GaN-based active rectifier used in 6.78 MHz WPT systems. From the literature review, the PLL-based synchronization controller has never been used for high-frequency active rectifiers, and there is a potential improvement in modeling the synchronization loop. A compact synchronization controller using commercial components is implemented to synchronize rectifier switching actions and regulate the load impedance at 6.78 MHz. The synchronization loop is analyzed by using discrete-time small-signal models accounting for the switching transient time. A process of finding the optimal operating point using discrete-time state-space techniques is described. Additionally, an EMI shielding technique improving the coil coupling is also investigated in this chapter.

4.1 Receiving Coil

In WPT systems, planar coils are commonly used in both primary and secondary sides because of their low-profile geometry, large charging surface, and compact volume. These properties make planar coils ideal to be integrated into consumer electronics that have horizontal flat surfaces such as laptops and monitors. Thus, a rectangular planar coil designed by Intel is utilized for this application. Its labeled dimensions and geometry are shown in Fig. 4.1.

Some consumer electronics like laptops whose outer housing is made of metal introduce a challenge on integrating the wireless receiver. Due to the eddy current effect,

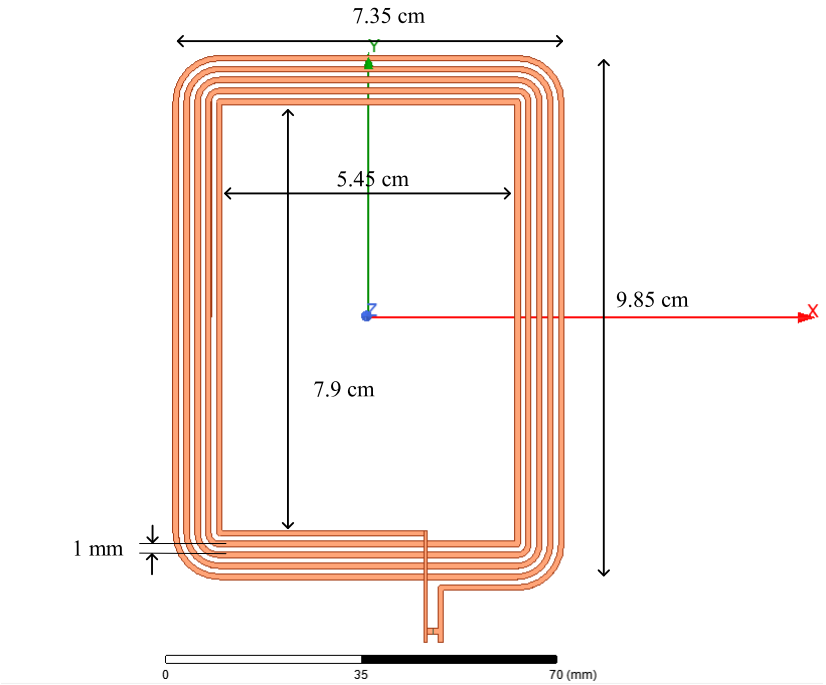

Fig. 4.1. Receiving coil geometry.

the magnetic flux cannot pass through the metal housing. A rectangular window at the center of the housing is cut to place the receiving coil, allowing the magnetic flux to bypass the housing and flow through the coil enclosed area. The 3D model of a rectangular metal plate representing the laptop housing is shown in Fig. 4.2. This method is simple and low-cost. However, the induced magnetic flux from the eddy current effect on the metal case still deteriorates the magnetic flux flowing through the receiving coil, reducing the coupling coefficient significantly**.** Fig. 4.3a and Fig. 4.3b illustrate the simulated eddy current vectors on the metal sheet and the side view of the simulated magnetic flux vectors generated from the transmitting coil in Maxwell software. The flux density passing through the receiving coil is reduced because of the eddy current effect.

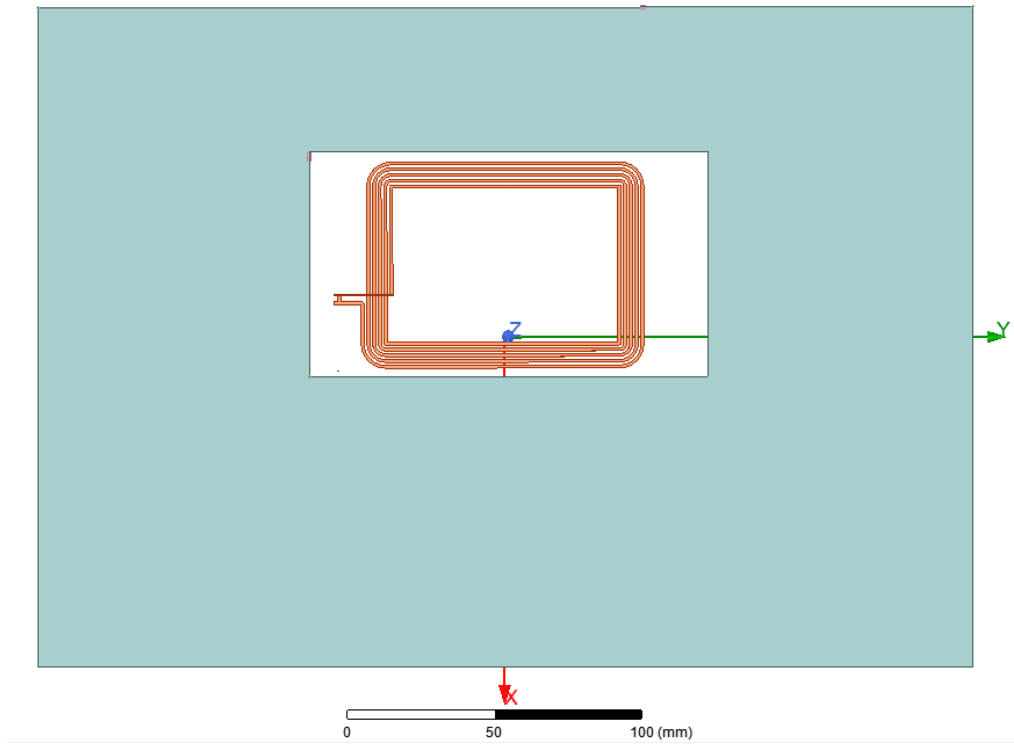

Fig. 4.2. 3D model of the metal sheet..

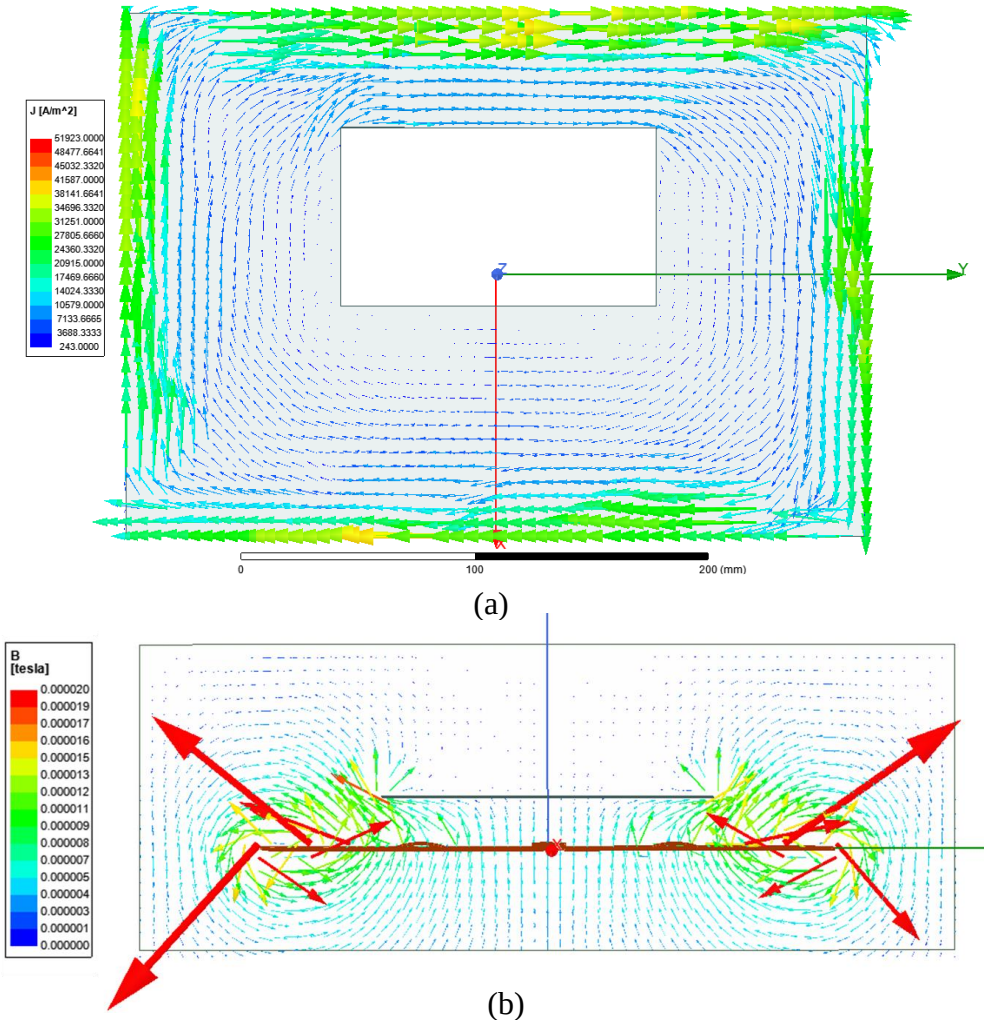

Fig. 4.3. (a) Top view of the simulated eddy currents on the metal sheet and (b) side view of the simulated magnetic flux density in the conventional cutting method.

To prevent this detrimental phenomenon, Intel has proposed a simple and effective approach that is to cut a small slot on the metal plate running from the central window to the outer edge, as shown in Fig. 4.4 [53]. Fig. 4.5a shows that, by cutting the metal plate, the simulated eddy current around the window is redirected to flow in the opposite direction. As a result, the induced magnetic field from the eddy current changes its polarity, leading to magnifying the total magnetic flux going through the receiving coil enclosed area and increasing the coil coupling coefficient. Fig. 4.5b illustrates a much higher magnetic flux density going through the receiving coil in the simulation, validating the proposed shielding technique. The complete coil setup is shown in Fig. 4.6, including the transmitting coil at the bottom.

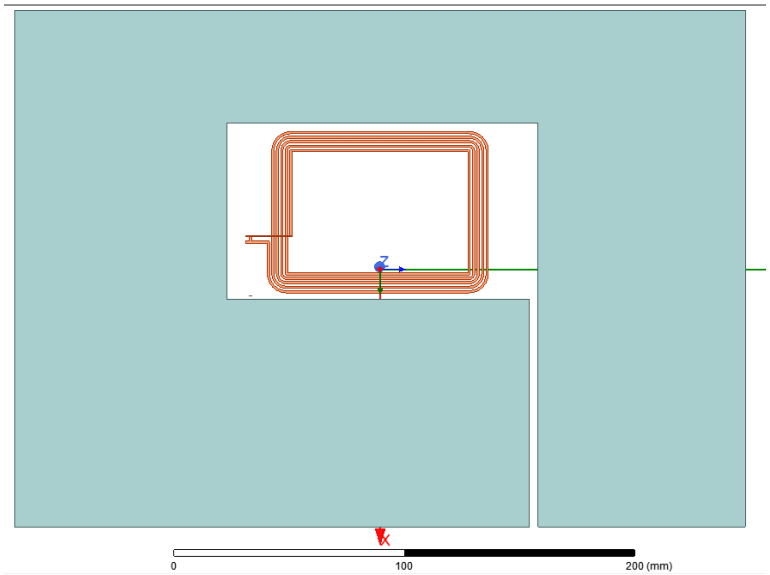

Fig. 4.4. 3D model of the slot-cut metal plate.

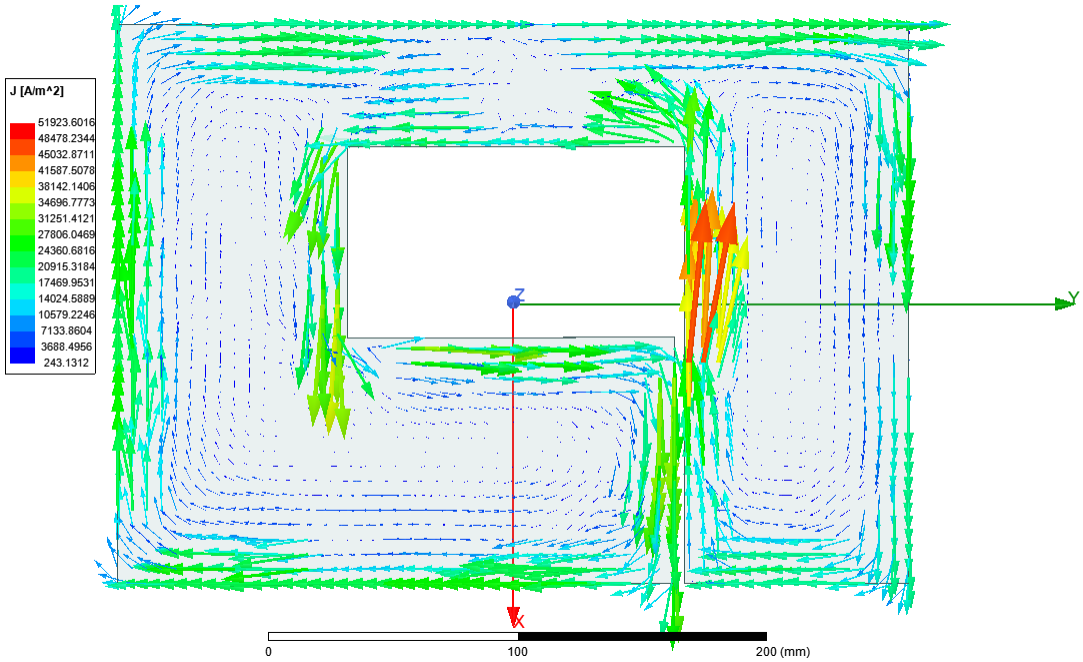

(a)

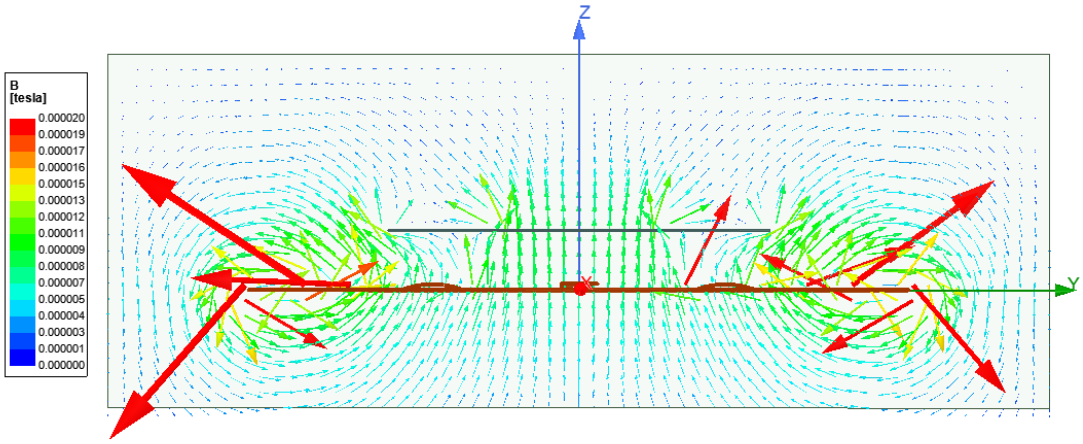

(b)

Fig. 4.5. (a) Top view of simulated eddy current on the metal sheet and (b) side view of simulated magnetic flux density in the new shielding method.

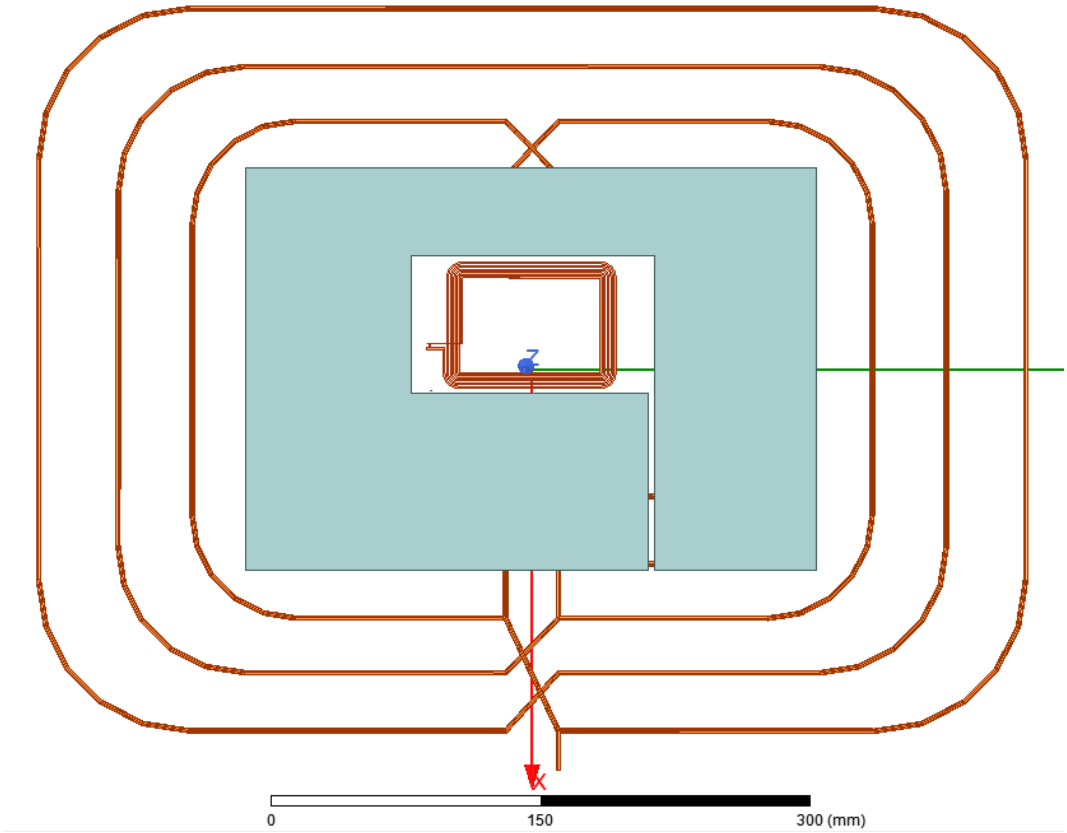

Fig. 4.6. 3D model of the complete coil setup.

4.2 Power Stage Model and Design

4.2.1 Circuit Topology

Fig. 4.7 shows the schematic of the full-bridge active rectifier in a series-series resonant WPT system. The circuit is comprised of a resonator, auxiliary resonant tank, active rectifier, and buck converter. The receiver coil L_s, capacitor C_s and equivalent series resistor R_s are connected in series forming a resonant network that has a resonant frequency $f_o = 1/(2\pi\sqrt{L_s C_s})$, which is near the operating frequency f_s. An auxiliary resonant tank consisting of L_r and C_r in parallel is added at the rectifier input to assist with ZVS achievement and keep the THD of the secondary voltage $v_s(t)$ low [23]. C_r is the equivalent parasitic capacitance of switches and any additional capacitance in the circuit. $Z_{rec} = R_{rec} + jX_{rec}$ is the equivalent load impedance seen by the resonator. $Z_s = R_s + jX_s$ denotes the open-circuit impedance of the resonator.

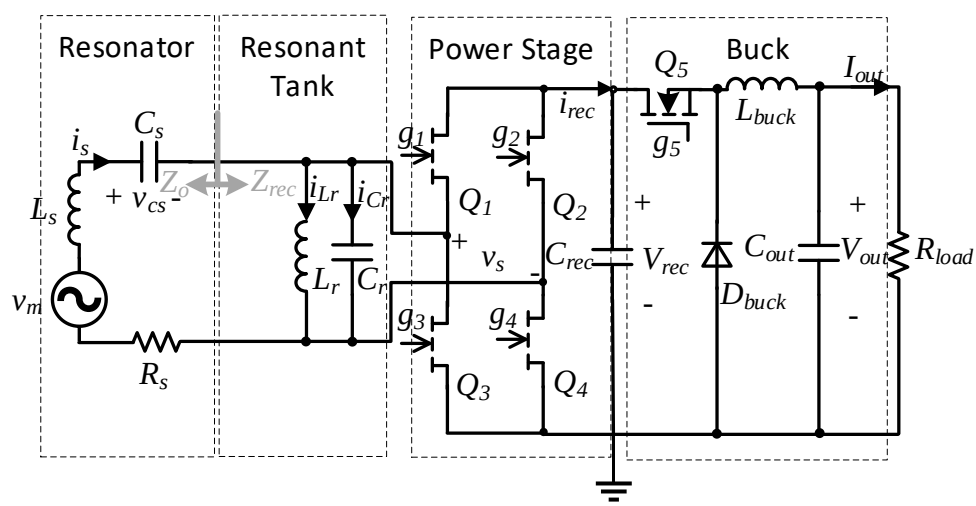

Fig. 4.7. Circuit schematic of the proposed rectifier.

In order to maximize coil-to-coil efficiency, the total reactance must be nulled ($X_{rec} = -X_s$) and R_{rec} must be set to the optimal value [20]. As mentioned, the active rectifier can alter Z_{rec} by controlling its switching timing to adjust the input phase ϕ_{v_s,i_s}. However, having ϕ_{v_s,i_s} as the only control parameter is not sufficient to separately change both reactive and resistive parts of the equivalent load impedance. A dc/dc buck converter is cascaded at the rectifier output to provide an additional control parameter, the rectified voltage V_{rec}, while maintaining the desired output voltage V_{out} at the load. In mobile electronics applications, this additional stage could be replaced by the battery charger.

The transmitter is designed to keep the sinusoidal current amplitude constant [18], which induces a constant ac voltage $v_m(t)$ on the secondary side, serving as the input source of the receiver. Since the induced voltage frequency f_m is identical to the transmitter switching frequency f_s with a phase offset, f_m is equal to the reference frequency for the synchronization control.

4.2.2 Discrete-time State-space Model of Power Stage

Operating waveforms of the rectifier are modeled using a time-varying state-space description. To find the steady-state operation, the discrete-time technique is employed, requiring the input $v_m(t)$ to be constant during each switching interval. Therefore, $v_m(t)$ is approximated as a square waveform, as shown in Fig. 4.8. The error induced by this approximation is minimal as long as a high-Q resonance between L_s and C_s at 6.78MHz is achieved.

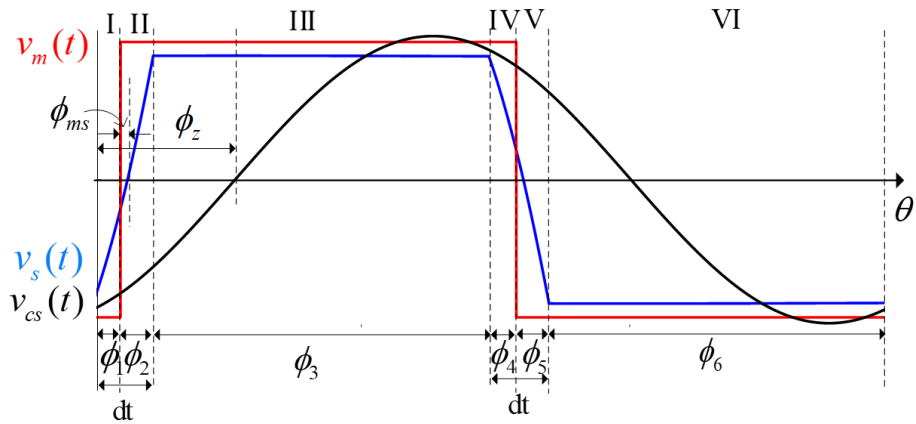

Fig. 4.8. Example steady-state rectifier waveforms.

Fig. 4.9 shows equivalent circuit schematics in six intervals per period. Regarding the first half of the waveform, intervals I and II are transition times where the drain-to-source capacitor is discharged by the resonant tank inductor current i_{Lr} before the switch is turned on to achieve full ZVS. The boundary of these two intervals is set when the piecewise constant dc V_m changes its polarity at the zero-crossing point of the actual ac induced voltage $v_m(t)$. Interval III is the power-delivery duration where two switches are on, forming a path to deliver current from V_m to the load.

The state-space representation of the rectifier circuit during the ith interval is

$$\dot{\mathbf{x}}(t) = \mathbf{A}_{\mathrm{i}}\mathbf{x}(t) + \mathbf{B}_{\mathrm{i}}\mathbf{u}(t), \tag{4.1}$$

where $\mathbf{x}(t)$ is the state vector consisting of five states $[v_{cs}(t)\ i_{Lr}(t)\ v_{rect}(t)\ v_s(t)\ i_{Ls}(t)]^T$ and $\mathbf{u}(t) = [v_m(t)\ \ I_{rec}]^T$ is the input vector. I_{rec} is the average value of the rectified current flowing through the rectifier, which is used to model the equivalent load, including the dc load and the buck converter, in the state space. PLECS [54] is used for extracting system and input matrix, $\mathbf{A}_i$ and $\mathbf{B}_i$, of the linear equivalent circuit during each interval.

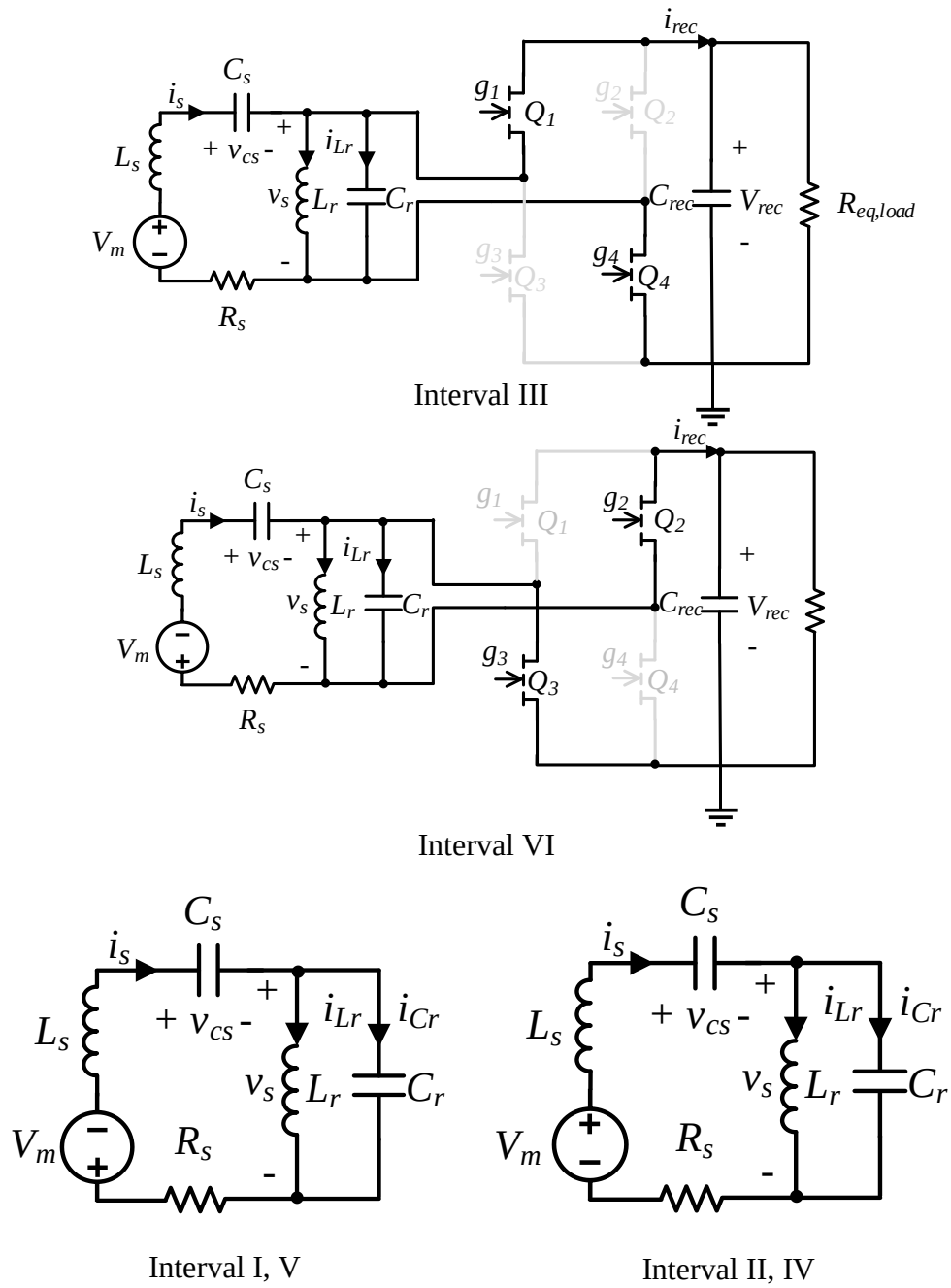

Fig. 4.9. Equivalent circuit schematics in each interval

For invertible $\mathbf{A}_i$, by leveraging asymmetric rectifier waveforms, and using a sampling frequency of $f_s/2$, the steady-state state vector $\mathbf{X}_0$ at the beginning of the period and the continuous state vector expression within each interval $\mathbf{x}(t)$ are [55]

$$\mathbf{X}_0 = \left(\mathbf{I}_{\mathrm{HC}} - \prod_{i=3}^{1} e^{\mathbf{A}_i t_i}\right)^{-1} \sum_{i=1}^{3} \left(\prod_{j=3}^{i+1} e^{\mathbf{A}_j t_j}\right) \mathbf{A}_i^{-1}(e^{\mathbf{A}_i t_i} - \mathbf{I})\mathbf{B_i}\mathbf{u}_i, \tag{4.2}$$

$$\mathbf{x}(t) = e^{\mathbf{A}_i t}\mathbf{x}_{i-1} + \mathbf{A}_i^{-1}(e^{\mathbf{A}_i t} - \mathbf{I})\mathbf{B}_i\mathbf{u}_i, \tag{4.3}$$

where $\mathbf{u}_i$ is input vector during interval i, and $\mathbf{x}_{i-1}$ is the state vector at the end of interval $i-1$. $\mathbf{I}_{\mathrm{HC}} = \mathrm{diag}(-1,-1,\ 1,-1,-1)$ is the square diagonal matrix accounting for the opposite polarity of ac waveforms in the second half of T_s. From (4.2) and (4.3), complete steady-state waveforms of the rectifier are constructed for any given operating conditions.

4.2.3 Steady-State Efficiency Modeling

Because the rectifier is designed to achieve full ZVS, the hard-switching loss is eliminated. The power loss then consists of the resonant tank inductor conduction loss $P_{L_r,cond}$, core loss $P_{L_r,core}$, and transistor conduction loss P_{cond}. Since the gate driver is powered by an auxiliary source, the gate loss is not included in the model. Fig. 4.10 is the chart showing power loss elements in the rectifier.

In this topology, the resonant tank inductor current $i_{Lr}(t)$ has a high-frequency ac waveform with a large RMS value, causing a significant loss. The resonant tank inductor L_r is fabricated in the lab by wrapping the magnetic wire around a low-profile high-frequency toroid core [56]. The core loss on the inductor is calculated using the empirical data provided by the manufacturer,

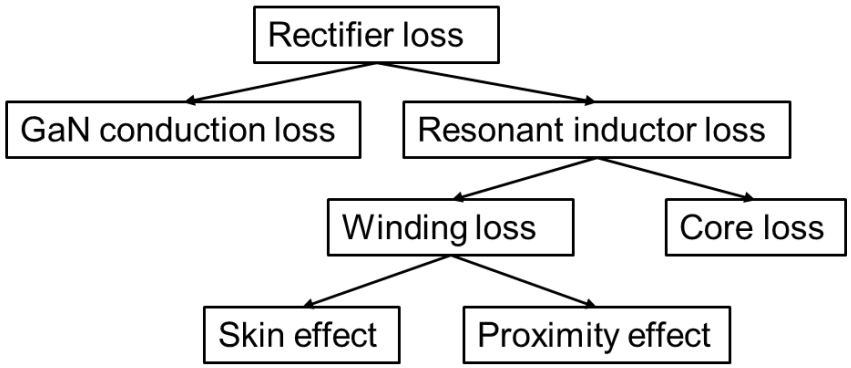

Fig. 4.10. Rectifier power loss chart.

$$P_{core} = \left(\frac{f_s}{\frac{a}{B_{pk}^3} + \frac{b}{B_{pk}^{2.3}} + \frac{c}{B_{pk}^{1.65}}} + dB_{pk}^2 f_s^2 \right) V_e, \tag{4.4}$$

where *a*, *b*, *c*, and *d* are coefficients of the core material provided by the manufacturer. The peak ac magnetic flux density B_{pk} is

$$B_{pk} = \frac{E_{rms} 10^8}{4.44 A_e N_{turn} f_s}, \tag{4.5}$$

where *a*, *b*, *c*, *d* are coefficients predefined in the inductor core datasheet, $A_e$is the cross-sectional area of the core, V_e is the core volume, and E_{rms} is the RMS value of the sinusoidal inductor voltage.

As the coil resistance varies with frequency, the inductor ac resistance R_{ac} needs to be derived as a function of f_s in order to compute the inductor conduction loss at 6.78 MHz. At high frequencies, R_{ac} drastically increases due to the skin and proximity effects. Using (3.10)-(3.12), R_{ac} is calculated and incorporated directly in the state-space model to find

the inductor conduction loss because no dc component is present in the inductor current. The input power is the power supplied from v_m subtracting the coil conduction loss since the coil is separately designed from the converter power stage

$$P_{in} = f_s \int_0^{T_s} (v_m(t) i_s(t) - i_s(t)^2 R_s) dt, \tag{4.6}$$

Then, the output power and converter efficiency are

$$P_{out} = f_s \int_0^{T_s} (v_{rec}(t) i_{rec}(t)) dt, \tag{4.7}$$

$$eff = \frac{P_{out}}{P_{in} + P_{core}}. \tag{4.8}$$

4.2.4 Optimal Efficiency and Power Component Selection

The process of finding the rectifier steady-state optimal operating condition and selecting components is shown in Fig. 4.11 and described as follows. A group of low R_{on} GaN FETs with rated blocking voltage ranging from $1.2V_{rec}$ to $4V_{rec}$ are pre-selected.

Since the transistor drain-to-source capacitance C_{ds} is nonlinear and dependent on the drain-to-source voltage v_{ds}, the charge-equivalent linearized C_{ds} at a given V_{rec} value is used,

$$C_{ds,eq} = \frac{1}{V_{rec}} \int_0^{V_{rec}} C_{ds}(v_{ds}) dv_{ds}. \tag{4.9}$$

In this optimization process, L_r is the sweeping parameter, and the amplitude of $v_m(t)$ stays constant. At any L_r value, inductor ac resistance R_{ac} are calculated using (3.10)-(3.12). Then R_{ac}, $C_{ds,eq}$ and R_{on} are incorporated in the state-space model to

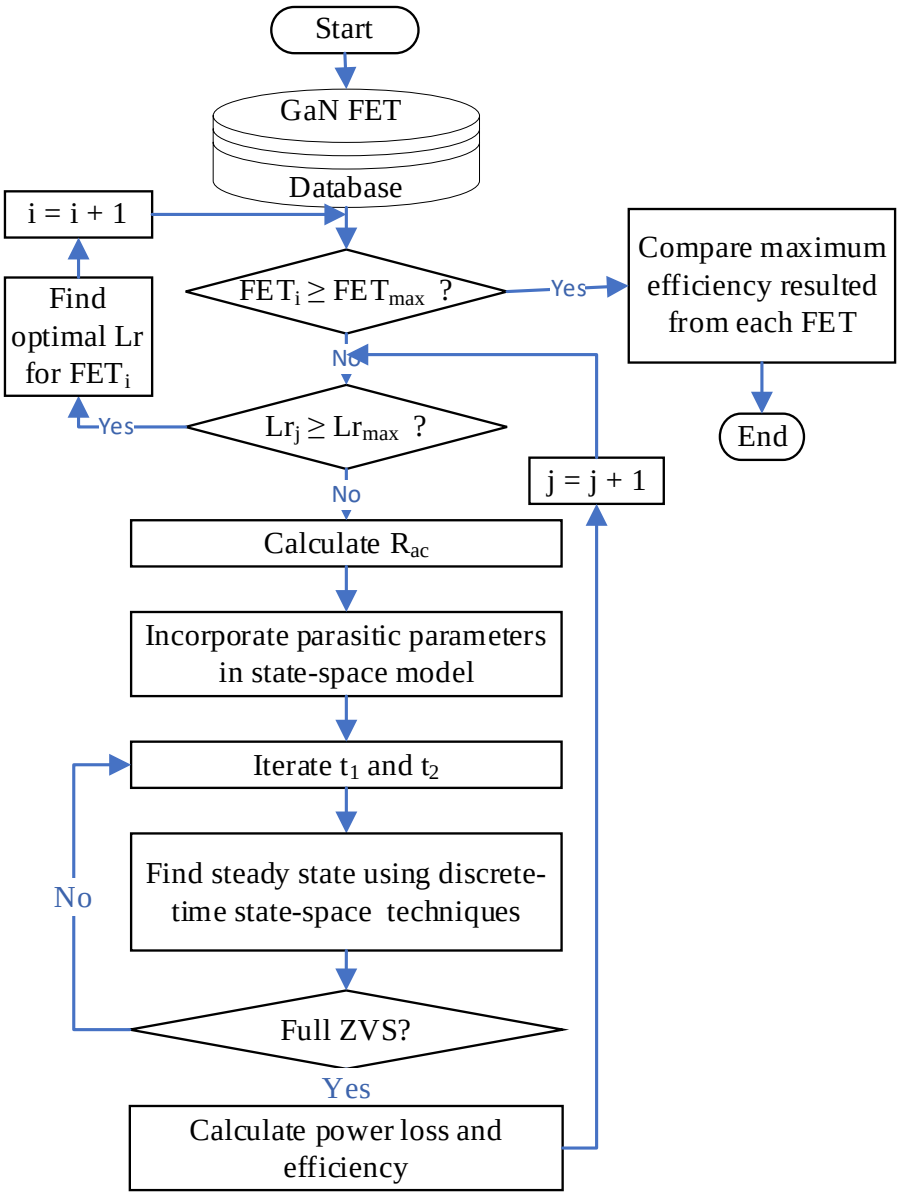

Fig. 4.11. Rectifier efficiency optimization process

evaluate the rectifier power loss. Furthermore, t_1 and t_2 are simultaneously iterated until full ZVS and the desired output power are achieved at the equilibrium point, which is found by applying discrete-time state-space techniques mentioned in Section 4.2. The rectifier efficiency is then computed by using (4.6)-(4.8), and compared with that at other operating points to find the maximum efficiency.

Fig. 4.12 shows the rectifier efficiency and input phase resulting from a single GaN FET with varying L_r. The efficiency increases at higher L_r due to reduced current i_{Lr}, resulting in lower core and conduction loss. However, reducing i_{Lr} results in less available current to assist in obtaining ZVS, leading to a reduced range of phases over which the converter can maintain ZVS. To prevent the design from requiring excessive reactive loading of the transmitter to obtain ZVS, the rectifier input phase is limited to $\pm 15°$ in this application. The red circle in Fig. 4.12 indicates the optimal operating point for the given GaN device.

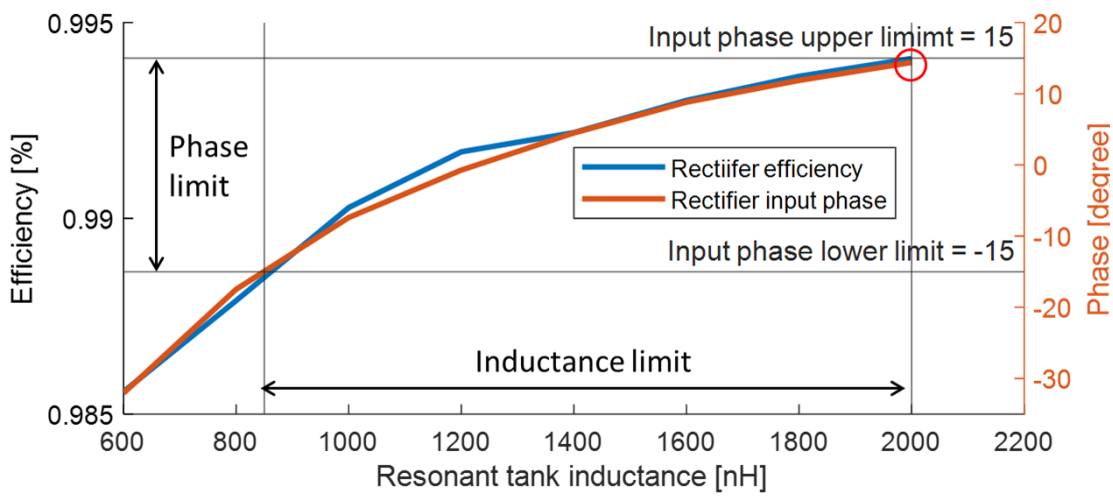

Fig. 4.12. Analytical rectifier efficiency with varying L_r

Finally, the EPC2007C GaN FET and 2μF L_r resulting in the highest efficiency are selected for building the converter. Selected components and parameter values are listed in Table 5.1 and Table 5.2 in Section 5.1. In conclusion, the rectifier power stage is designed to achieve ZVS, and has 15° phase angle and 99.4% efficiency.

4.3 Synchronization Control

4.3.1 Synchronization Control Principle

The principle of this PLL-based synchronization control is to sense a periodic signal related to the input $v_m(t)$ and generate an output signal that is phase-locked to the input signal, resulting in equal frequencies. The PLL output signal is then used to drive the switching actions of the rectifier. Fig. 4.13 shows the structure of the on-board PLL-based synchronization control consisting of a phase-frequency detector (PFD), a charge pump (CP), a compensating loop filter $G_c(z)$, a microcontroller (MC), and a digitally controlled oscillator (DCO).

Improved from work in [33], which senses the noise-susceptible secondary current $i_s(t)$, the receiver-side tuning capacitor voltage $v_{cs}(t)$ being sensed in this work is relatively large and out of phase with the rectifier switching actions when the rectifier load is nearly resistive. As a result, the PLL has a high immunity to switching noise, even at low power, ensuring the proper functionality in wide loading conditions. This advantage is also demonstrated in [57], [39].

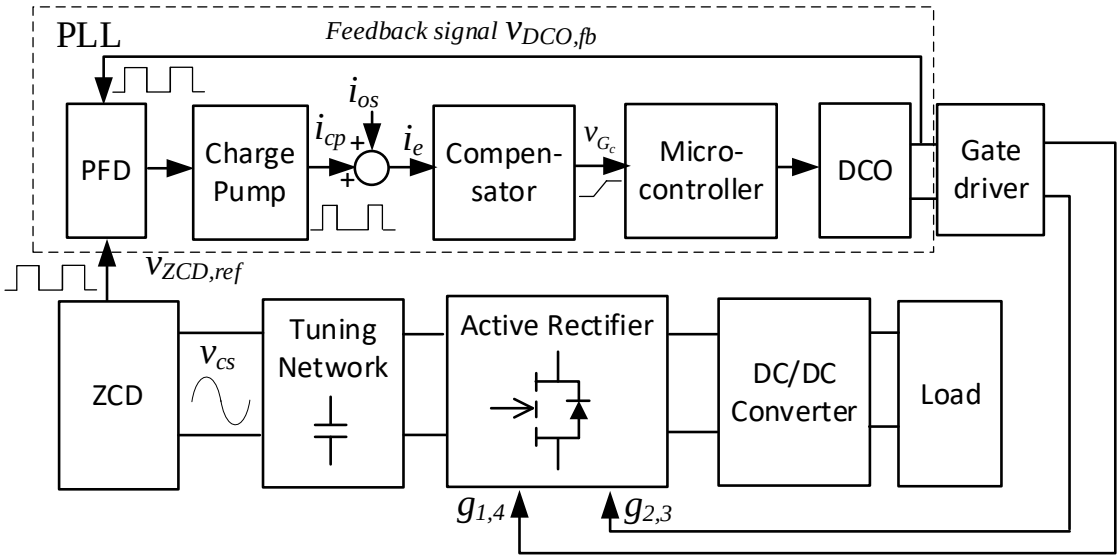

Fig. 4.13. Synchronization control structure.

The phase information of $v_{cs}(t)$ is extracted by detecting its zero-crossing point using a zero-crossing detector (ZCD) to generate a reference signal $v_{ZCD,ref}(t)$. This signal is then fed to the PFD, along with the PLL output signal $v_{DCO,fb}(t)$, to measure their phase difference ϕ_{PFD}. The PFD controls the charge pump to output current pulses $i_{cp}(t)$ whose average value is proportional to ϕ_{PFD}. The phase between $v_{ZCD,ref}(t)$ and $v_{DCO,fb}(t)$ can be locked but separated by a phase offset ϕ_{os} by either injecting or withdrawing an amount of current i_{os} at the CP output. The resultant current pulse i_e, whose average value is proportional to the phase error ϕ_e, is fed to the analog compensator/loop filter $G_c(z)$ to convert to a voltage level v_{G_c} corresponding to ϕ_e. The compensator $G_c(z)$ is designed to stabilize the loop and achieve a target bandwidth. A low-power microcontroller samples the voltage level v_{Gc} using the integrated analog to digital converter (ADC) module and generates communication signals controlling the output signal frequency of the DCO. The

DCO outputs two complementary signals used as PWM signals driving the switching actions of the rectifier. The dead time dt between gate signals is set using a resistor-programmed gate driver. As mentioned above, one of the DCO outputs is also used as a feedback signal to the PFD, completing the closed-loop synchronization control.

4.3.2 Small-signal Power Stage Model

To examine the stability of the synchronization loop, an analytical approach is developed in [39] to model the response of the sensed signal phase to the dynamics of the rectifier switching actions. An extended model is presented in this section, where the dead time between rectifier switching states is taken into account. Also, an extra auxiliary parameter, i.e. t_2, is included in the model, to model the reverse conduction of GaN FETs clamping v_s to v_{rec} at the end of the resonant interval.

The small-signal state vector at sampling points derived using the discrete-time technique [58] has the form

$$\hat{\mathbf{x}}[n+1] = \mathbf{F}\hat{\mathbf{x}}[n] + \mathbf{\Gamma}\hat{\phi}_1[n] + \mathbf{\Lambda}\hat{\phi}_2[n], \tag{4.10}$$

where $\hat{\mathbf{x}}[n+1]$ is the state deviation responding to perturbations in the previous state $\hat{\mathbf{x}}[n]$, control parameter $\hat{\phi}_1[n]$, and auxiliary parameter $\hat{\phi}_2[n]$. Since the input vector $\mathbf{u}(t)$ remains unchanged during each interval, inputs are not perturbed and not included in (4.10). Coefficient matrices $\mathbf{F}, \mathbf{\Gamma}$, and $\mathbf{\Lambda}$ are

$$\mathbf{F} = (e^{\mathbf{A}_3 t_3} e^{\mathbf{A}_2 t_2} e^{\mathbf{A}_1 t_1} \mathbf{X}_0)\mathbf{I}_{HC}, \tag{4.11}$$

$$\mathbf{\Gamma} = e^{\mathbf{A}_3 t_3} e^{\mathbf{A}_2 t_2}((\mathbf{A}_1 - \mathbf{A}_2)\mathbf{X}_1 + \mathbf{B}_1\mathbf{u}_1 - \mathbf{B}_2\mathbf{u}_2)\frac{T_s}{2\pi}, \tag{4.12}$$

$$\mathbf{\Lambda} = e^{\mathbf{A}_3 t_3}((\mathbf{A}_2 - \mathbf{A}_3)\mathbf{X}_2 + \mathbf{B}_2\mathbf{u}_2 - \mathbf{B}_3\mathbf{u}_3)\frac{T_s}{2\pi}. \tag{4.13}$$

To model the reverse conduction, the response of $v_s(t)$ to perturbations is also analyzed at the end of the dead time. Because only the linear equivalent circuit is modeled during the dead time in interval II, the FET drain-to-source voltage can take on spurious negative values if t_2 is not constrained to the correct value based on the large-signal transition to reverse conduction. To model this behavior, a constraint equation, $\sigma = 0$, is included in the model, where σ is generally a vector of constraint equations. In this case, only one constraint is included: the value of $v_s(t)$ at the end of t_2 is equal to V_{rec}, assuming the voltage drop on FETs is negligible,

$$\begin{aligned}\sigma(t_1, t_2) = \ & \mathbf{C}_{v_s}(e^{\mathbf{A}_2 t_2} e^{\mathbf{A}_1 t_1}\mathbf{X}_0 + e^{\mathbf{A}_2 t_2}\mathbf{A}^{-1}(e^{\mathbf{A}_1 t_1} - \mathbf{I})\mathbf{B}_1\mathbf{u}_1 \\ & + \mathbf{A}^{-2}(e^{\mathbf{A}_2 t_2} - \mathbf{I})\mathbf{B}_2\mathbf{u}_2) - V_{rec} = 0,\end{aligned} \tag{4.14}$$

where $\mathbf{C}_{v_s} = [0\ 0\ 0\ 1\ 0]$ is used to select the desired state, v_s, from the state vector. When this constraint holds, during every period, $v_s(t)$ at the end of t_2 stays fixed at V_{rec} due to the reverse conduction of the FETs. The small-signal model of (4.14) is then,

$$\hat{\sigma}[n+1] = \mathbf{C}_{v_s}(\mathbf{F}'\hat{\mathbf{x}}[n] + \mathbf{\Gamma}'\hat{\phi}_1[n] + \mathbf{\Lambda}'\hat{\phi}_2[n]) = 0, \tag{4.15}$$

where

$$\mathbf{F}' = \frac{\partial\sigma}{\partial x} = \mathbf{C}_{v_s} e^{\mathbf{A}_2 t_2} e^{\mathbf{A}_1 t_1}, \tag{4.16}$$

$$\mathbf{\Gamma}' = \frac{\partial\sigma}{\partial\phi_1} = \mathbf{C}_{v_s} e^{\mathbf{A}_2 t_2}((\mathbf{A}_1 - \mathbf{A}_2)\mathbf{X}_1 + \mathbf{B}_1\mathbf{u}_1 - \mathbf{B}_2\mathbf{u}_2)\frac{T_s}{2\pi}, \tag{4.17}$$

$$\mathbf{\Lambda}' = \frac{\partial\sigma}{\partial\phi_2} = \mathbf{C}_{v_s}((\mathbf{A_2} - \mathbf{A_3})\mathbf{X_2} + \mathbf{B_2}\mathbf{u_2} - \mathbf{B_3}\mathbf{u_3})\ \frac{T_s}{2\pi}. \tag{4.18}$$

Using the generalized state-space modeling technique [58], the linearized constraint equation (4.14) and small-signal model (4.10) are combined to obtain the equivalent small-signal form of the state vector

$$\hat{\mathbf{x}}[n+1] = \mathbf{F_{eq}}\hat{\mathbf{x}}[n] + \mathbf{\Gamma_{eq}}\hat{\phi}_1[n], \tag{4.19}$$

where

$$\mathbf{F}_{eq} = \mathbf{F} - \mathbf{\Lambda}(\mathbf{\Lambda}')^{-1}\mathbf{F}', \tag{4.20}$$

$$\mathbf{\Gamma}_{\mathrm{eq}} = \mathbf{\Gamma} - \mathbf{\Lambda}(\mathbf{\Lambda}')^{-1}\mathbf{\Gamma}' \tag{4.21}$$

Then, the $\hat{\phi}_1[n]$ to $\hat{\mathbf{x}}[n+1]$ transfer function is

$$G_{x\phi_1}(z) = \left(\left(z\mathbf{I} - \mathbf{F}_{eq}\right)^{-1}\mathbf{\Gamma}_{eq}\right). \tag{4.22}$$

which incorporates the impact of the transistor reverse conduction and dead time during switching transitions.

4.3.3 Inherent Zero-Crossing Feedback Model

When the control parameter ϕ_1 is perturbed, small-signal states are propagated through the entire switching period, causing a deviation in the zero-crossing point t_z of $v_{cs}(t)$. Thus, to model the synchronization loop dynamic behavior, the transfer function from the control perturbation $\hat{\phi}_1[n]$ to the sensed phase deviation $\hat{\phi}_z$[n+1] is derived by following the modeling framework in [39].

$$G_{\phi_z,\phi_1}(z) = \mathbf{C}_{v_{cs}}\left(\mathbf{H}G_{x\phi_1}(z) + \mathbf{J}\right)\frac{2\pi}{T_s\left(-\dot{v}_{cs,z}\right)}. \tag{4.23}$$

where

$$\mathbf{H} = e^{\mathbf{A}_3(t_z - t_2 - t_1)} e^{\mathbf{A}_2 t_2} e^{\mathbf{A}_1 t_1} \mathbf{I}_{HC}, \tag{4.24}$$

$$\mathbf{J} = -e^{\mathbf{A}_3(t_z - t_2 - t_1)} e^{\mathbf{A}_2(t_2)} ((\mathbf{A_1} - \mathbf{A_2})\mathbf{X}_1 + \mathbf{B_1}\mathbf{u_1} - \mathbf{B}_2\mathbf{u}_2) \frac{T_s}{2\pi}. \tag{4.25}$$

$\dot{v}_{cs,z}$ is the linearized slope of $v_{cs}(t)$ at the zero-crossing point t_z

$$\dot{v}_{cs,z} = \mathbf{C}_{v_{cs}}(\mathbf{A}_3\mathbf{X}_z + \mathbf{B}_3\mathbf{u}_3), \tag{4.26}$$

where $\mathbf{X}_z$ is the steady-state state vector at t_z and $\mathbf{C}_{v_{cs}} = [1\ 0\ 0\ 0\ 0]^T$.

4.3.4 Synchronization Loop Dynamics

Fig. 4.14 shows a block diagram of the complete small-signal model of the synchronization loop, including the dynamics of the power stage. The loop gain of the synchronization loop is

$$T_{sync}(z) = \left(-1 - G_{\phi_z,\phi_1}(z)\right) K_{PFD} G_c(s) K_{ADC} K_{DCO} \left(\frac{-2\pi}{s}\right)\left(\frac{1}{N}\right), \tag{4.27}$$

where $\left(-1 - G_{\phi_z,\phi_1}(z)\right)$ presents the effective change in the input phase difference ϕ_{PFD} at the PFD resulting from ϕ_1 perturbation. The PFD gain is calculated by averaging the maximum CP output current over one period

$$K_{PFD} = i_{cp,max}/2\pi. \tag{4.28}$$

The gain of the ADC integrated into the microcontroller is the ratio between the digital output range and the input voltage level range

$$K_{ADC} = ADC_{out,range}/ADC_{in,range}. \tag{4.29}$$

The DCO gain depends on the operating frequency f_s and is linearized at steady state

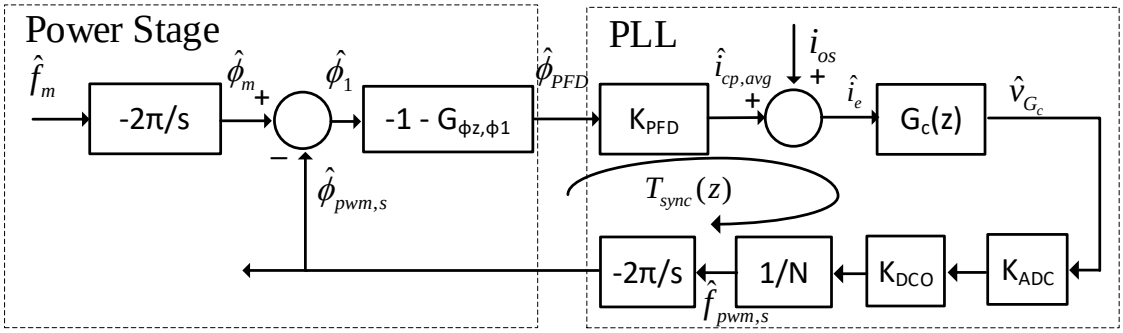

Fig. 4.14. Block diagram of the synchronization loop including the converter dynamics.

$$K_{DCO} = \frac{f_{DCO}[n+1] - f_{DCO}[n]}{DCO_{in}[n+1] - DCO_{in}[n]}, \tag{4.30}$$

where $DCO_{in}[n]$ is the digital input value of the DCO setting the output frequency $f_{DCO}[n]$ to the steady-state operating frequency f_s, which is nearly 6.78 MHz in this application.

The 1/*N* gain in Fig. 4.14 models the frequency divider integrated into the PFD chip, which is used to reduce the feedback signal frequency. The fraction $-2\pi/s$ is the frequency-to-phase conversion gain in radians. The negative sign indicates the inverse correlation between $\hat{f}$ and $\hat{\phi}$. For reference, negative $\hat{\phi}$ value implies the deviation of the corresponding signal to the left and vice versa.

4.3.5 Compensator Design

The bode plot of the uncompensated loop gain $T_{sync,un}$ has a high phase margin of 90° and low bandwidth of 630 Hz. A compensator is required to keep the steady-state phase error at zero and increase the bandwidth for a faster response while maintaining an acceptable phase margin. Also, the compensated bandwidth must be at least a decade below

the ADC rate and f_s to sufficiently attenuate the impact of nonlinear sampling behaviors and switching noise on the control. Therefore, the control bandwidth and phase margin are targeted at 10 kHz and 45°. Bode plots of $T_{sync,un}$ and T_{sync} are shown in Fig. 4.15.

Fig. 4.16 shows the circuit of the compensator, which is a combination of an integral and a lead compensator. The integrator is used to convert the error signal i_e into v_{Gc} which is the reference to adjust the output frequency to bring the error down to zero. However, the pole in the integrator reduces the phase margin by 90°, causing instability. Thus, the lead compensator is added to increase the phase margin to 45°. The general transfer function of the compensator is obtained based on the circuit,

$$G_c(s) = \frac{\hat{v}_{G_c}}{\hat{\imath}_{cp}} = G_{c0}\frac{1+\frac{s}{2\pi f_z}}{s\left(1+\frac{s}{2\pi f_p}\right)}, \tag{4.31}$$

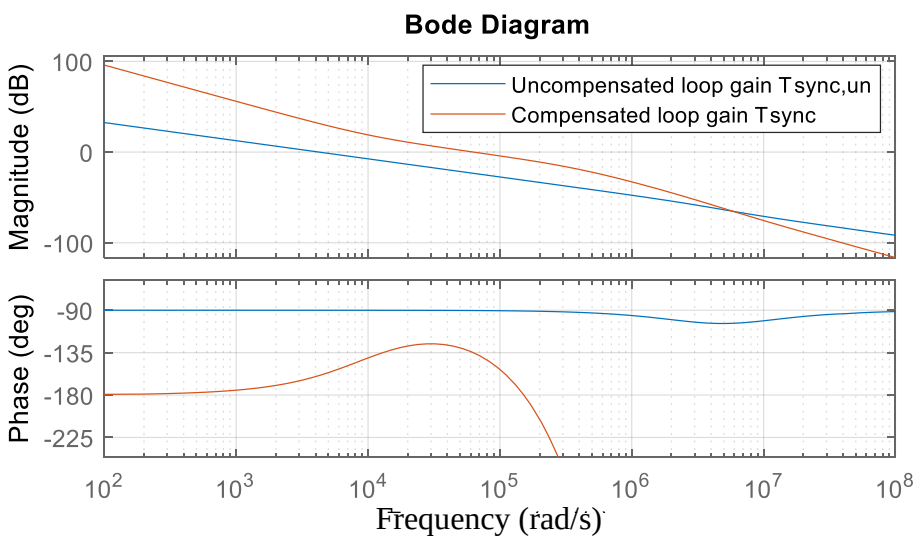

Fig. 4.15. Bode plots of $T_{sync,un}(z)$ and $T_{sync}(z)$.

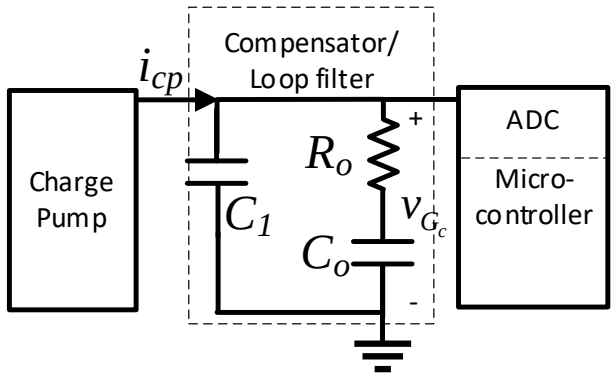

Fig. 4.16. Compensator circuit schematic.

which has one zero and two poles. The compensator phase θ_{com} at the crossover frequency f_c is the difference between the desired phase margin $\theta_{desired}$ and the uncompensated phase margin $\theta_{T_{sync,un}}$

$$\theta_{com} = \theta_{desired} - \theta_{T_{sync,un}} - \theta_{delay} + \frac{\pi}{2}, \tag{4.32}$$

where $\pi/2$ and $-\theta_{delay}$ are also added to compensate for the phase margin reduction due to the integrator and delay in PLL components. To realize the calculated compensator phase, the pole and zero frequencies are

$$f_z = f_c \sqrt{\frac{1 - \sin(\theta_{com})}{1 + \sin(\theta_{com})}}, \tag{4.33}$$

$$f_p = f_c \sqrt{\frac{1 + \sin(\theta_{com})}{1 - \sin(\theta_{com})}}. \tag{4.34}$$

Then the compensator dc gain is

$$G_{c0} = \frac{s\left(1 + \frac{s}{2\pi f_p}\right)}{T_{sync,un}(j\omega_c)\left(1 + \frac{s}{2\pi f_z}\right)}, \tag{4.35}$$

where $T_{sync,un}(j\omega_c)$ is the uncompensated loop gain at the desired crossover frequency. With the full compensator transfer function being derived, compensator component values are calculated and listed in Table 4.1. Finally, a compensator is accomplished to increase the control speed to 10 kHz and keep the synchronization loop stable with a phase margin of 45°.

4.3.6 Dynamic Control of the Rectifier Input Phase

In order to regulate the equivalent load impedance in real-time, a rectifier phase control scheme is proposed to adjust the rectifier phase angle dynamically. As previously mentioned in Section 4.3, the reference and feedback signals fed to the PFD are locked in phase and separated by a phase offset ϕ_{os}. The rectifier input phase is adjusted when ϕ_{os} is changed. ϕ_{os} is controlled by injecting or withdrawing a current i_{os} at the compensator input. To maintain the zero i_e, which is the sum of i_{os} and i_{cp}, the PLL controller

Table 4.1. Compensator and compensated loop gain parameter values.

Parameters	**Symbol**	**Value**
Compensator parallel capacitance	C_1	0.16 μF
Compensator series resistance	R_0	16.24 Ω
Compensator series capacitance	C_0	6.12 μF
Loop gain crossover frequency	f_c	10 kHz
Loop gain phase margin	ϕ_{PM}	45°

modifies ϕ_{os} to compensate for i_{os}. Fig. 4.17 shows the implementation of the auxiliary current i_{os} by connecting an external resistor R_{os} between the general purpose input/output (GPIO) pin of the microcontroller and the compensator input. For instance, when the GPIO pin is set high at 3.3 V, R_{os} becomes a pull-up resistor, allowing the current i_{os} to be injected to the compensator, and vice versa. The amount of i_{os} is

$$i_{os} = \frac{S_{MSP}V_{dd} - V_{Gc}}{R_{os}}, \tag{4.36}$$

where S_{MSP} is a binary variable indicating the state of the GPIO pin, $V_{dd} = 3.3$ V is the supply voltage of the IC, and V_{Gc} is the steady-state voltage of the compensator.

For each R_{os}, there are only two available i_{os} values from low and high GPIO states. To add more controlling points, a digital variable ADC_{offset} is introduced to the control algorithm programmed in the microcontroller, as shown in Fig. 4.18. The gain $1/M$ presents the number of bits truncated from the ADC_{out} for noise filtering purpose. The

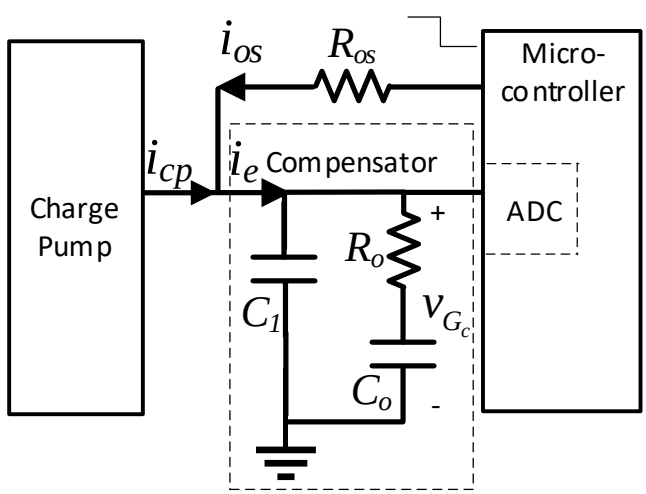

Fig. 4.17. Implementation of the phase control scheme.

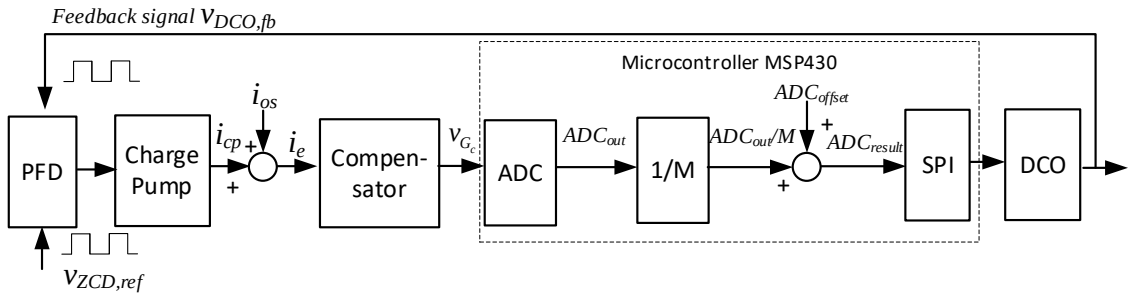

Fig. 4.18. Block diagram of the phase angle control scheme.

ADC_{offset} and ADC_{out}/M values are combined, resulting in ADC_{result} used to determine the DCO ouput frequency.

In steady-state, due to the presence of a stable, closed-loop integral compensator, the ADC_{result} is nearly constant at the value that sets the DCO output frequency to be 6.78 MHz. It means that the variable $ADC_{offset} = ADC_{result} - ADC_{out}/M$ shifts the steady-state value of ADC_{out}, equivalently altering the compensator steady-state voltage level V_{Gc}

$$V_{Gc} = \frac{(ADC_{result} - ADC_{offset})M}{K_{ADC}}. \tag{4.37}$$

Phase offset between the sensed signal v_{cs} and feedback signal v_{DCO} is

$$\phi_{os} = \frac{-i_{os}}{K_{PFD}}. \tag{4.38}$$

The relation between ϕ_{os} and ADC_{offset} are obtained from (4.36),(4.37), and (4.38)

$$\phi_{os} = \frac{(-S_{MSP}V_{dd}K_{ADC} + M\left(ADC_{result} - ADC_{offset}\right))}{K_{ADC}K_{PFD}R_{os}}. \tag{4.39}$$

Equation (4.40) shows that ϕ_{os} and ADC_{offset} are inversely proportional, and each ADC_{offset} value results in a different ϕ_{os} value. Fig. 4.19 shows that the control range of ϕ_{v_s,i_s} can be expanded or reduced by changing R_{os}. Therefore, using the additional digital parameter ADC_{offset} provides the ability to control ϕ_{os}, which effectively controls the rectifier input phase ϕ_{v_s,i_s} with high-resolution and wide control range.

4.4 Summary

Steady-state operating conditions and waveforms of the rectifier are modeled using discrete-time state-space techniques. The power loss model is provided to calculate the rectifier efficiency in the process of finding the highly-efficient operating point and selecting optimal power components. In the optimization process, for each FET being evaluated, L_r is the sweeping parameter by iterating its number of turns on a single coil.

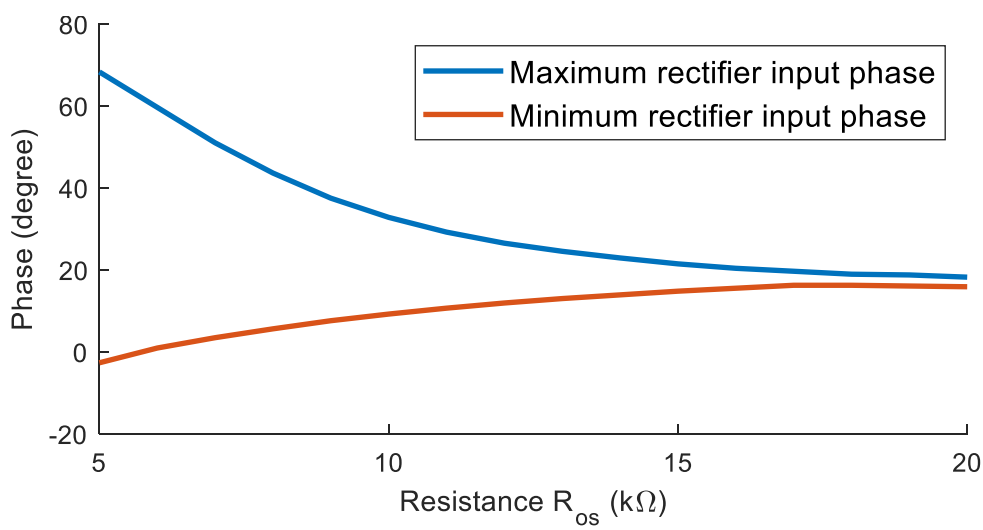

Fig. 4.19. Analytical control range of ϕ_{v_s,i_s} with varying R_{os}.

Generally, the efficiency increases at higher L_r due to reduced current i_{Lr}, resulting in lower core and conduction loss. L_r is also limited by the rectifier input phase that must be small. Utilizing the efficiency trend and the input phase constraint, the optimal operating point yielded from each FET is found.

The principle of the compact and low-cost synchronization control network based on PLL techniques is described. The tuning capacitor voltage is sensed, which has immunity to the switching noise, leading to robust synchronization. The previous study in [39] proposes a modeling framework addressing the inherent feedback in the PLL synchronization loop by but neglects the rectifier dead time. Improved from that model, this work successfully accounts for the transient time and reverse conduction of GaN devices in the ZVS operation. Based on the analyzed control loop gain, an analog compensator is designed to increase the control bandwidth and stabilize the control loop. Furthermore, the dynamic rectifier impedance control utilizing the rectifier phase angle is proposed for matching impedance in real-time.

Chapter Five

EXPERIMENTAL VERIFICATION

Experimental setups of the entire WPT system used to validate open-loop and closed-loop operation of the synchronous active rectifier are shown and described in this chapter. PCB layout design strategies used to minimize parasitic elements and component selection are also discussed. Finally, the end-to-end efficiency of the entire open-loop WPT system is measured to validate the low-loss power stage design.

5.1 Rectifier Prototype

5.2.1 Power Stage PCB Layout

Fig. 5.1 shows the prototype of the proposed 40W 6.78 MHz synchronous active rectifier. The control system is implemented on the same board with the rectifier due to the compact synchronization control design. Prototype parameter values and component numbers are listed in Table 5.1 and Table 5.2, respectively.

Table 5.1. Prototype circuit parameters.

Parameters	Symbol	Value
Receiver coil inductance	L_s	3.78 µH
Secondary tuning capacitance	C_s	150 pF
Receiver coil resistance	R_s	1.024 Ω
Resonant tank inductance	L_r	2 µH
Transmitter coil inductance	L_p	16.194 µH
Primary tuning capacitance	C_p	53 pF
Transmitter coil resistance	R_p	1.05 Ω
Coupling coefficient	k	0.1952

Table 5.2. Prototype component numbers.

Component	Part
GaN FET	EPC2007C
Gate driver	LMG1210
PFD	ADF4002
Microcontroller	MSP430F5172
DCO	LTC6903
Buck converter	LMR14030
Inductor core	T44-17

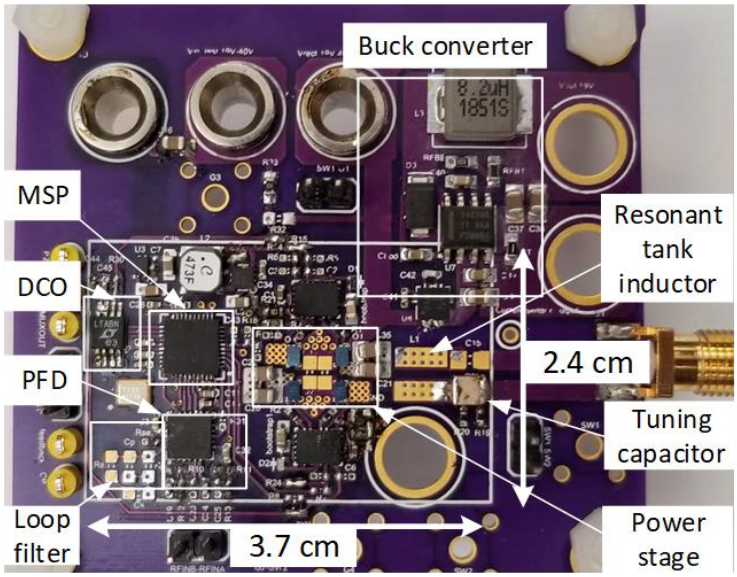

Fig. 5.1. Synchronous rectifier prototype.

At high switching frequencies, reducing parasitic elements in the PCB layout is critical to prevent ringing and overshoot at the switch node voltages. The PCB layout is designed to minimize the parasitic inductance in the converter circuitry. Also, the power stage layout is designed to be symmetrical to ensure the same impedance of the two power current paths, resulting in symmetrical waveforms.

Fig. 5.2 is the 3D model of the symmetrical rectifier power stage layout in Altium Designer. Fig. 5.3 shows each layer of the power stage layout (4 layers). The high side transistors Q_1 and Q_2 are controlled by one half-bridge gate driver, while the low side transistors Q_3 and Q_4 are driven by a second gate driver. Each side has its own decoupling capacitors that are connected to an output voltage bus on the third layer (Fig. 5.3c) and a ground plane on the second layer (Fig. 5.3d). An example color-coded current path is drawn in Fig. 5.4 and described as follows. The current flows from the resonant tank down to the bottom layer through vias, and back to the top layer before reaching the first switch node. It then flows through Q_1 to the decoupling capacitors and the ground plane on the second

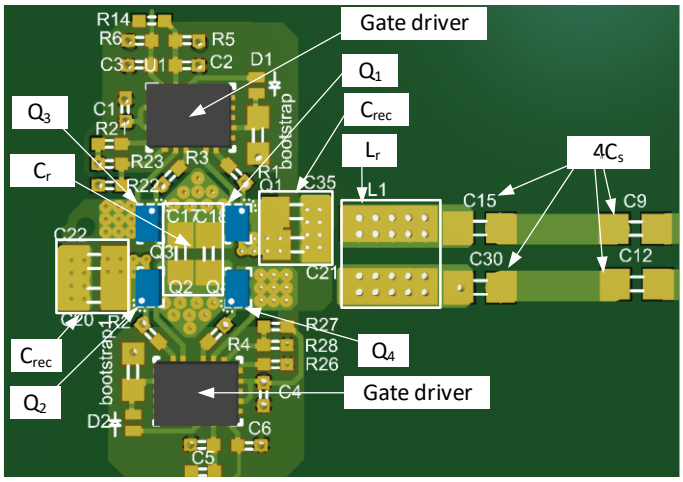

Fig. 5.2. 3D model of the rectifier power stage layout in Altium Designer.

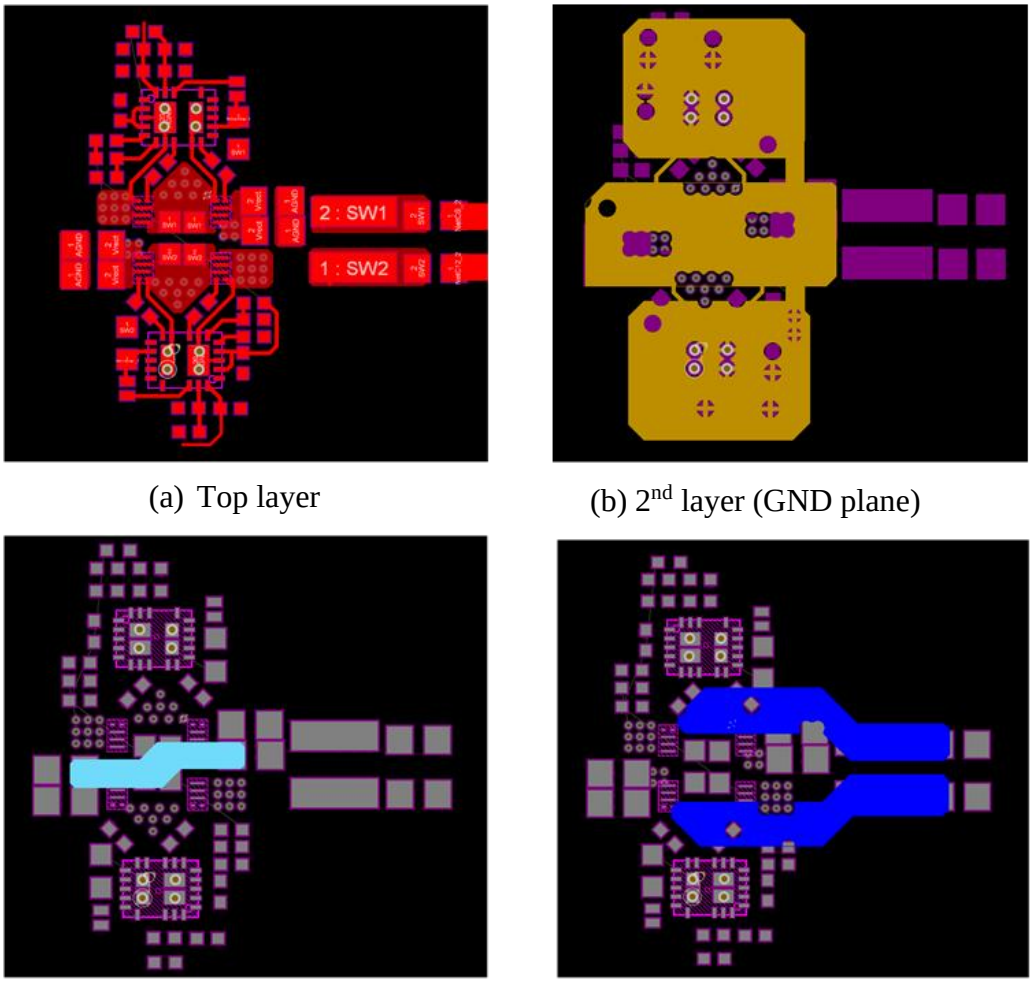

(a) Top layer

(b) 2nd layer (GND plane)

(c) 3rd layer (V_{rec})

(d) Bottom layer

Fig. 5.3. Power stage layout in different layers

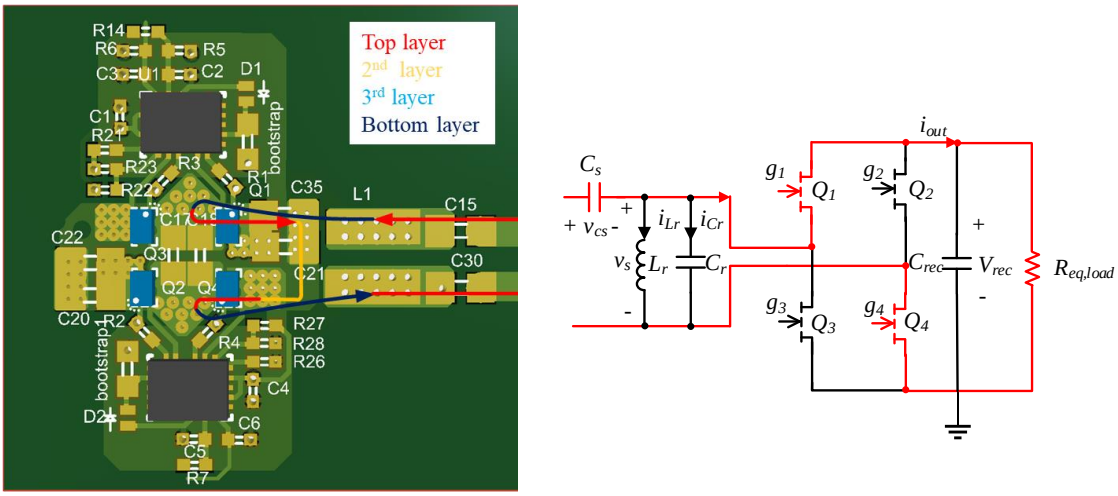

(a) (b)

Fig. 5.4. (a) Color-coded example power current path in the 3D PCB layout, and (b) circuit schematic with the same current path.

layer. The current then goes back to the top layer, then flows to the low-side switch node through Q_4. Finally, it reaches the resonant tank completing the power loop.

Because GaN devices are sensitive to overvoltage at the gate terminal, measures must be taken to reduce the parasitic inductance in the gate driving signal path. Thus, gate drivers are placed in close proximity with the GaN devices, and small resistors are added to the signal path to mitigate ringing and overshoot. Furthermore, the gate driver's ground plane is separated from the power stage ground to reduce switching noise. Fig. 5.5 shows the rectifier waveforms in open-loop at full power of 40 W with minimal ringing.

5.2.2 Component Selection

As chosen in Section 4.2, four EPC2007C GaN FETs are used as switches for the full-bridge rectifier. They have low on-resistance R_{on}, low parasitic capacitance C_{oss}, high

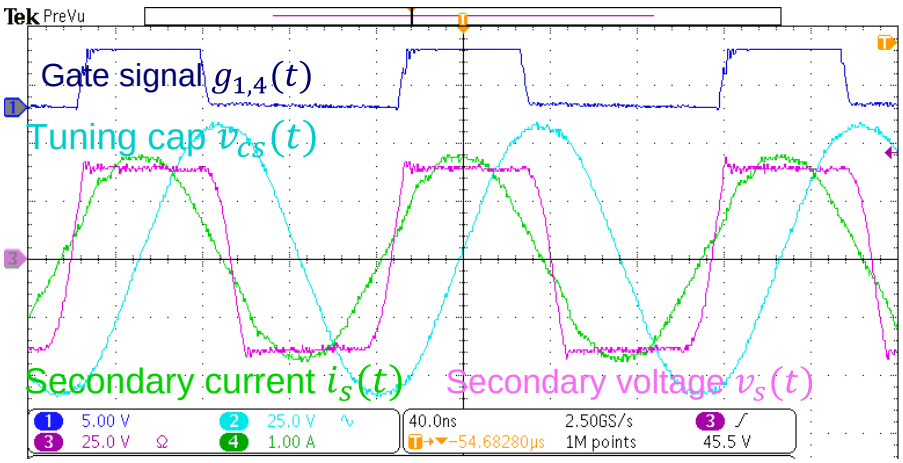

Fig. 5.5. Symmetrical rectifier waveforms at full load with minimal ringings and overshoot.

allowable conducting current, and high blocking voltage up to 100V [59]. Also, the total charge required to turn on the device Q_g is relatively low, reducing the gate loss.

The LMG1210 half-bridge gate driver from Texas Instruments is selected because of its advantages at high frequencies. First, using half-bridge gate drivers is beneficial for reducing space and part count compared to using single gate drivers such as LM5114 and UCC27611. Second, the LMG1210 can drive GaN FETs at up to 50 MHz [60], which is much higher than the required operating frequency of 6.78 MHz. Third, the LMG1210 offers an extremely low switch-node capacitance of 1pF, reducing the power loss dissipated on the switch-node capacitance. Experimentally, the LMG1210 consumes less than 0.244 W while driving four GaN FETs, whereas the LM5113 half-bridge gate drivers dissipate nearly 4W (2 W per driver) [61]. Also, the LM5114 utilizes an external bootstrap capacitor allowing the designer to optimize the capacitance value depending on the converters. Finally, one of the most important features of this gate driver that enables the proposed

synchronization approach in this thesis is the ability to operate in the PWM mode: it can take a reference signal and generate two complementary driving signals with a dead time programmed by an external resistor. Without this feature, the DCO would need to generate four PWM signals and control the dead time, which complicates the synchronization control design. Note that the rectifier dead time is pre-configured based on the model and stays fixed during the entire operation.

The ADF4002 frequency synthesizer consists of a low noise PFD, CP, and programmable frequency divider N. The PFD can detect the phase difference of signals up to 104 MHz, satisfying the frequency requirement [62]. Also, a ZCD module integrated into the ADF4002 is used to extract the phase of the sensed signal $v_{cs}(t)$ and generate a reference signal. However, the maximum differential voltage at the ZCD inputs is limited to only 600 mV. Therefore, a pair of parallel Schottky diodes connected in the opposite polarity is added between ZCD inputs to prevent the overvoltage.

The MSP430F5172 microcontroller is low-cost, compact, and powerful enough to execute necessary commands in the control system. The internal clock signal can be digitally boosted up to 25 MHz, allowing fast operations, which is crucial in this 6.78 MHz application [63]. Furthermore, the integrated 10-bit ADC module is leveraged to sample the voltage level from the compensator The MSP430F5172 supports the SPI communication protocol used to control the external DCO.

The final component in the synchronization control is the LTC6903 DCO. It consumes low power and requires no external components, resulting in size and component

count reduction. The LTC6903 is capable of outputting two complementary signals whose frequency is controlled by the microcontroller through the standard SPI interface [64].

5.2 Experimental Open-loop Operation

In order to validate the rectifier power stage model, an open-loop 6.78 MHz WPT system shown in Fig. 5.6 is set up for reading waveforms and measuring efficiency. The target specifications of the designed WPT system and equipment used in the open-loop test are listed in Table 5.3 and Table 5.4, respectively.

The primary side of the system is composed of a dc voltage source, half-bridge inverter, impedance matching network, and transmitting coil, as designed in [11]. The circuit schematic of the inverter is shown in Fig. 5.7. A resonant tank inductor is added between the inverter switch node and the ground to ensure ZVS operation at full load.

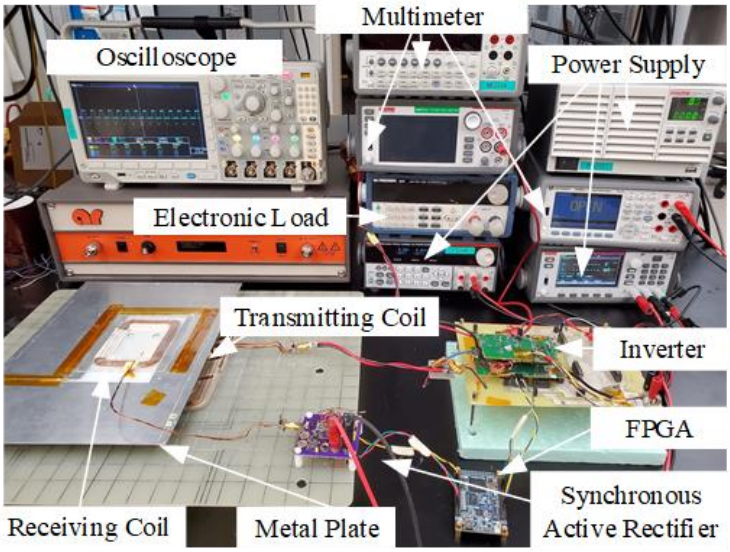

Fig. 5.6. Experimental setup of the open-loop test.

Table 5.3. Specifications of the WPT system.

Parameters	**Symbol**	**Value**
Operating frequency	f_s	6.78 MHz
Output power	P_o	40 W
Rectified voltage	V_{rec}	40 V
Output voltage	V_o	19 V
Transmitter input voltage	V_g	110 V

Table 5.4. Equipment part numbers in the open-loop setup.

Equipment	**Part number**
FPGA	Cyclone IV EP4CE22F17C6N
DC power source	KEITHLEY 2260B-800-4
Electronic load	BK Precision 8600
Oscilloscope	MDO3104

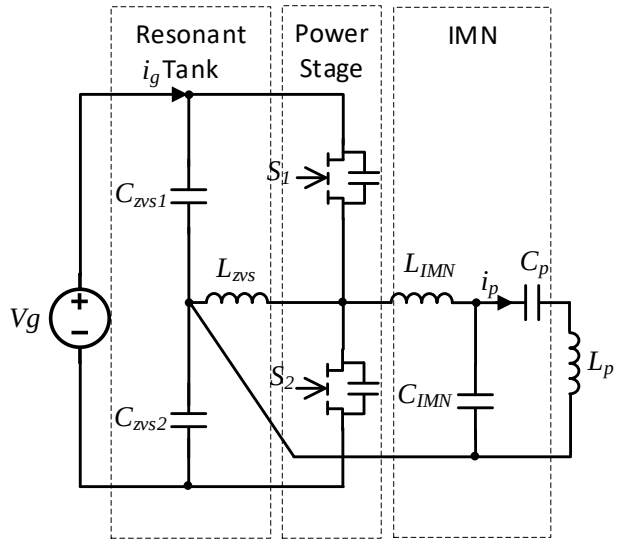

Fig. 5.7. Circuit schematic of the ZVS half-bridge inverter.

Supplying power to the inverter is a dc voltage source whose output voltage is adjusted to change the transmitter current's peak level. The transmitting coil is designed to achieve a high Q and distribute the magnetic flux evenly on the charging surface. It is separated from the receiving coil by 2 cm.

The secondary side is composed of a receiving coil, the proposed full-bridge active rectifier, an auxiliary power source, and an electronic load. Compared to the transmitting coil, the receiving coil is much smaller so that it can be integrated into consumer electronics and designed to achieve a high Q. As discussed in Section 4.1, the receiving coil is placed at the center of the slot-cut metal plate to mitigate the destructive effect of the eddy currents on the magnetic flux flowing through the coil. The synchronization control of the active rectifier is temporarily shut down, allowing it to operate open-loop. The rectifier output bus is connected to the electronic load, which is set in the constant resistance mode.

Although the system is operating open-loop, the synchronization between transmitter and receiver switching actions is still required to ensure a stable operation. A simple synchronization scheme is shown in Fig. 5.8, which employs an FPGA to control both the inverter and rectifier. The FPGA is programmed to generate two pairs of complementary PWM signals at 6.78 MHz. The first pair of PWM signals with adjustable dead time is fed to half-bridge gate drivers of the inverter. The second pair of PWM signals are connected to the rectifier's gate drivers. The dead time of the rectifier is set by an external resistor connected to the gate driver and stays constant throughout the operation. The phase shift between primary and secondary driving signals can be adjusted by the FPGA, which effectively changes the rectifier input phase. As a result, the synchronization between the rectifier and the inverter is accomplished. It is important to notice that this synchronization technique is only used for testing purposes because the wired connection between two sides is prohibited in practical WPT systems.

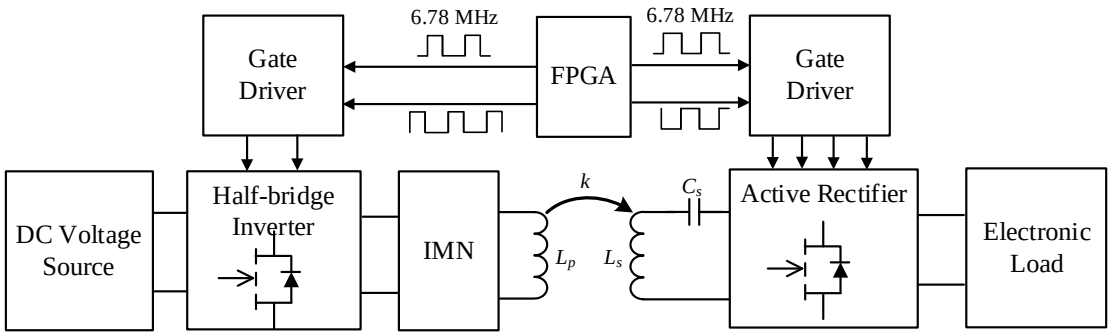

Fig. 5.8. Block diagram of the synchronization scheme in open-loop operations.

5.3 Experimental Open-loop Results

Open-loop experimental and modeled rectifier operating waveforms are shown in Fig. 5.9. The experimental waveforms are well-matched with the modeled ones, confirming the accuracy of the model of the steady-state operation using discrete-time state-space techniques. Note that the amplitude of the experimental $v_{cs}(t)$ is divided by 4 by using a series of four capacitors to reduce the stress on differential input terminals of the ZCD.

The measured power loss at full load is compared to the predicted value to validate the power loss model. The output power is calculated from the output voltage and current, which are measured by using precise multimeters in Kelvin connections. There are two approaches to measure the input power.

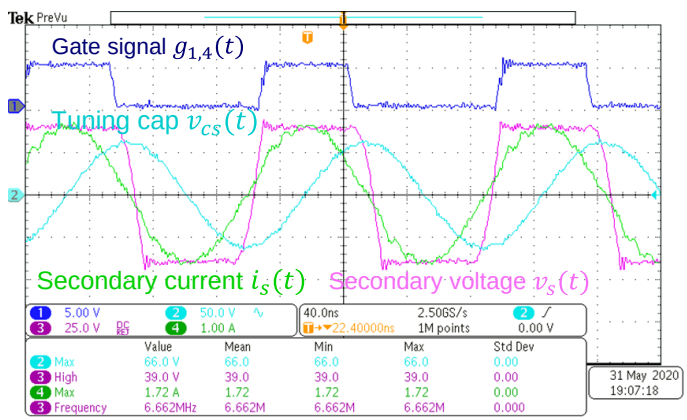

(a)

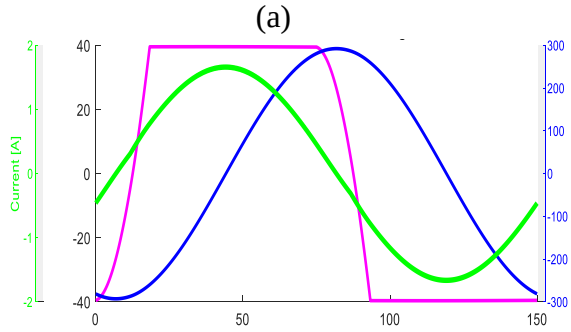

(b)

Fig. 5.9. (a) Open-loop experimental rectifier waveforms, and (b) modeled waveforms.

It is difficult to measure the input ac power from $v_s(t)$ and $i_s(t)$ waveforms because of the measurement error caused by non-ideal factors such as the mismatched dead time, harmonic contents, probe delays are non-negligible at 6.78 MHz. Thus, the input dc power at the inverter voltage source is measured to eliminate non-ideal factors in ac measurements, improving the measurement accuracy. Now the experimental power loss includes the loss of the entire open-loop WPT system, meaning the more complex power loss model of the entire WPT system has to be examined and compared with the experimental data. Also, the power loss of the WPT system using a diode rectifier at similar operating conditions is measured to validate the power loss model further and showcase the benefit of the active rectifier in increasing the efficiency.

Similar inverter waveforms from two WPT systems are presented in Fig. 5.10, confirming that these tests are conducted at the same operating condition. Fig. 5.11 shows the comparison between the measured and analytical power loss breakdown of two WPT systems at 40 W. illustrates the calculated and measured power loss breakdown of these two systems. Although there is a discrepancy between the model and measurement caused by parasitic elements, the power loss reduction is well predicted in the model. Using the designed active rectifier significantly reduces the total loss by nearly 1.75 W, which is 4.36% of the output power.

The open-loop WPT setup is also utilized to carry out experiments that validate the transfer function $G_{\phi_z,\phi_1}(z)$ derived in Section 4.3. More specifically, the experimental step response of the sensed signal phase ϕ_z to the perturbation of $0.001(2\pi)$ in the control parameter ϕ_1 is compared with modeled ones. In order to acquire the experimental step

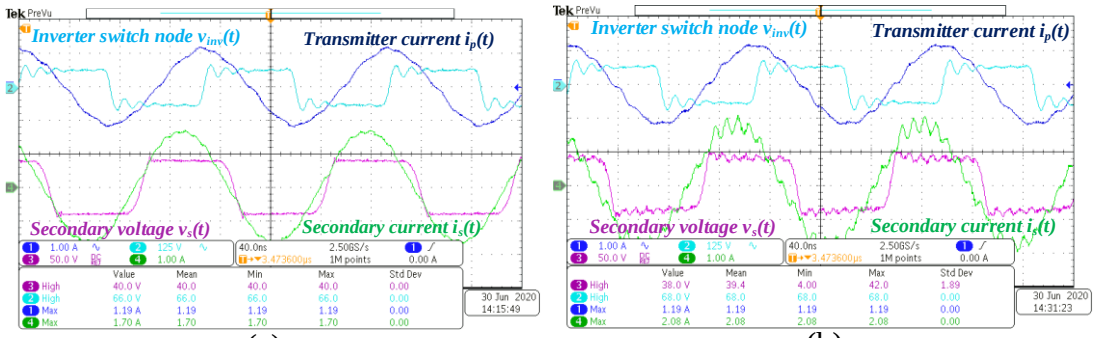

(a) (b)

Fig. 5.10. Waveforms from the open-loop WPT systems using (a) an active rectifier, and (b) a diode rectifier.

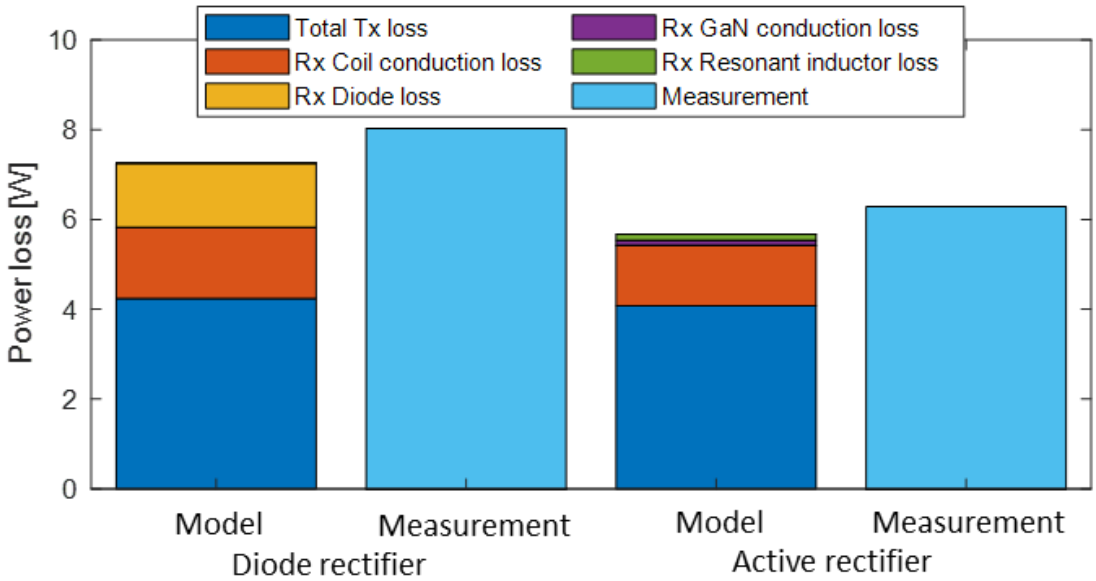

Fig. 5.11. Power loss breakdown comparison of WPT systems consisting of a synchronous active rectifier and a diode rectifier.

response, waveforms at the perturbed point are captured in the oscilloscope and imported to MATLAB for extracting phase values ϕ_z. Then they are plotted over a number of periods. As shown in Fig. 5.12, the experimental result is well-matched with the step response extracted from the analytical small-signal model, Simulink model, LTspice model. It has better accuracy compared with the model developed in the previous work [39]. Therefore, the transfer function $G_{\phi_z,\phi_1}(z)$ derivation is confirmed to be valid and accurate.

5.4 Experimental Closed-loop Operation

In this section, the closed-loop operation of the entire WPT system, where the active rectifier switching actions are synchronized with the inverter operation without using wire connections, is demonstrated. In other words, the rectifier input phase is regulated at a constant value when the synchronization is established. This section focuses on

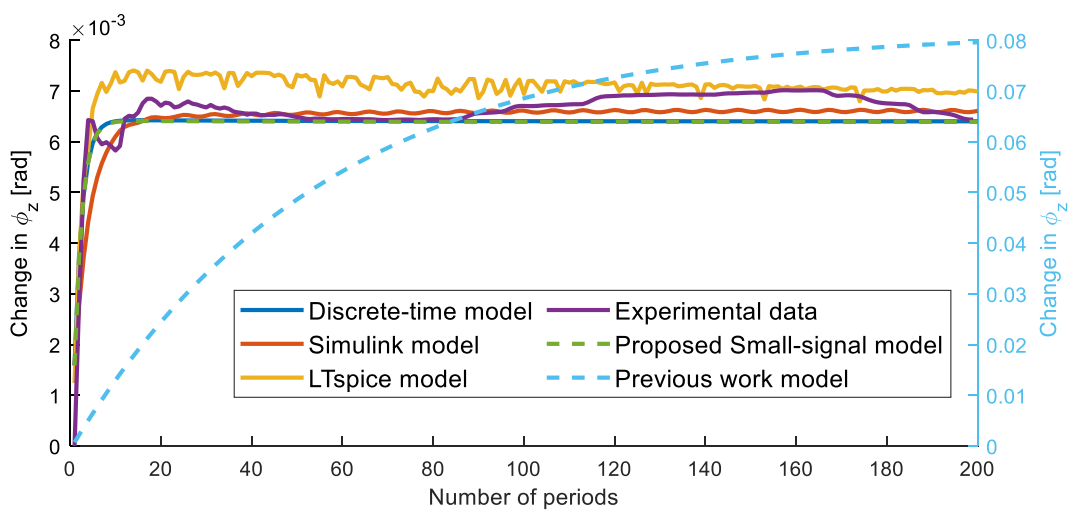

Fig. 5.12. Comparison of step response of G_{ϕ_z,ϕ_1} between experimental results with different models, including previous work [39].

synchronizing the rectifier at steady state, meaning it regulates the input phase at a pre-defined value. The dynamic input phase control is discussed in the next section.

The experimental setup and block diagram of the complete WPT system in closed-loop operation are shown in Fig. 5.13, and Fig. 5.14, respectively. The main difference from the open-loop setup is the removal of the FPGA's connection with the rectifier. Since there is no communication channel between the transmitter and receiver, the synchronization between them is accomplished by using the proposed control network on the secondary side. The synchronization components on the receiver are turned on to sense the secondary tuning capacitor voltage $v_{cs}(t)$ and control the rectifier switching actions instead of using driving signals from the FPGA.

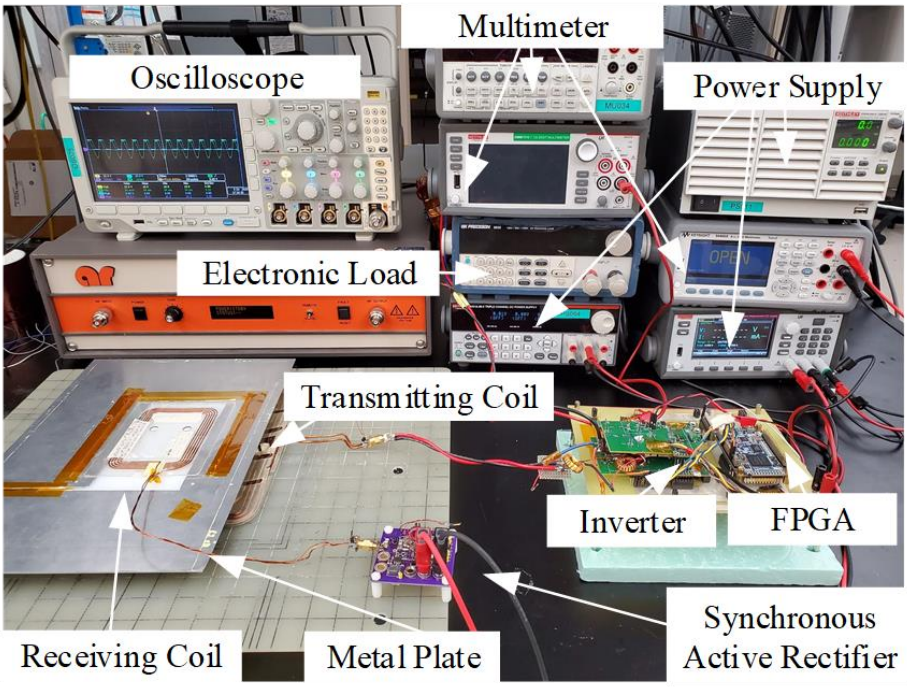

Fig. 5.13. Closed-loop experimental setup.

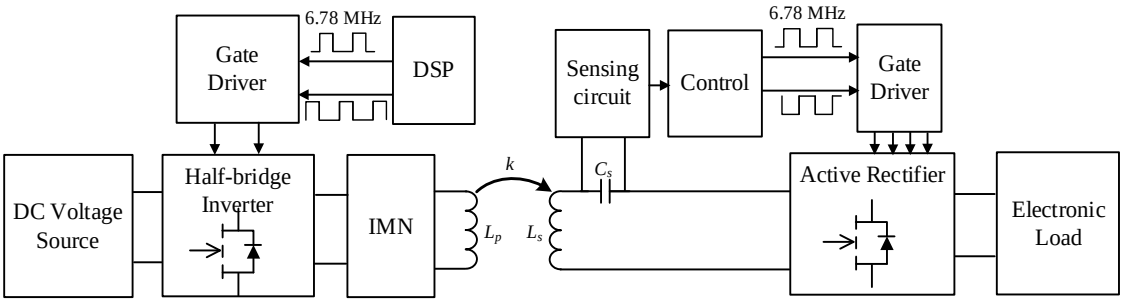

Fig. 5.14. Block diagram of the closed-loop setup.

In closed-loop, rectifier operating waveforms at full load of 40 W are captured by the oscilloscope and displayed in Fig. 5.15, which have a good agreement with open-loop and modeled waveforms. To demonstrate stable synchronization, the value of ϕ_{v_s,i_s} is extracted from v_s and i_s waveforms using MATLAB, and plotted across the number of periods in Fig. 5.16. The rectifier phase angle ϕ_{v_s,i_s} is well regulated to be nearly constant with an average phase offset of 15°, which is predicted by the model. The subtle jitter in ϕ_{v_s,i_s} resulting in an RMS error of 0.3° is caused by the quantization limit in ADC and DCO. Due to the robustness of the designed control, the rectifier is synchronized at a low output power of 0.02W, as shown in Fig. 5.17.

5.5 Dynamic Control of the Rectifier Input Phase

In this section, several experiments are conducted to validate the proposed control scheme of the rectifier input phase ϕ_{v_s,i_s}. In the first experiment, a 10 kΩ R_{os} is selected, the state of the GPIO pin is initially set high ($S_{MSP} = 1$), and ADC_{offset} is gradually decreased from 700 to 529, which effectively increases the compensator voltage level V_{Gc} from 0.75 V to 3 V. In this configuration, the current i_{os} is injected to the compensator

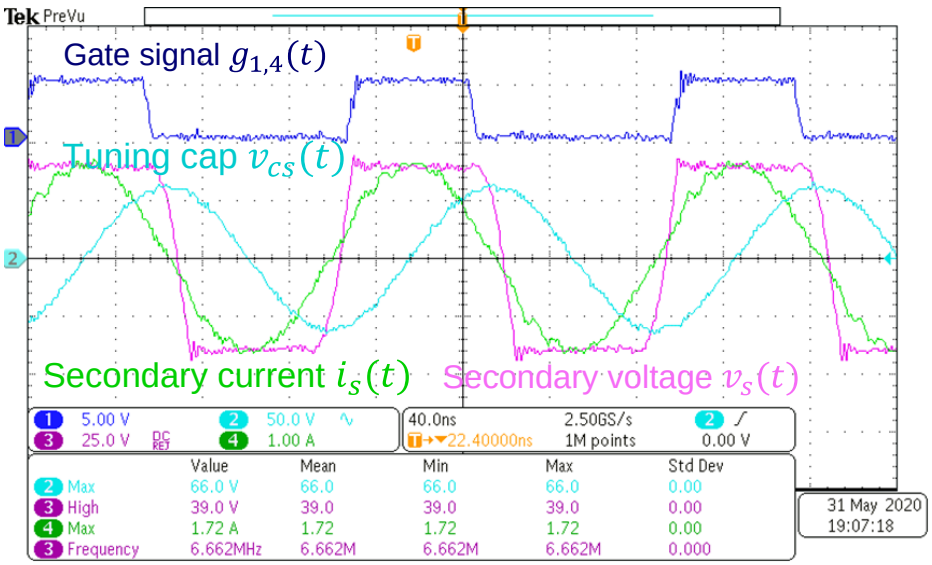

Fig. 5.15. Experimental rectifier waveforms in closed-loop operation at full load (40W).

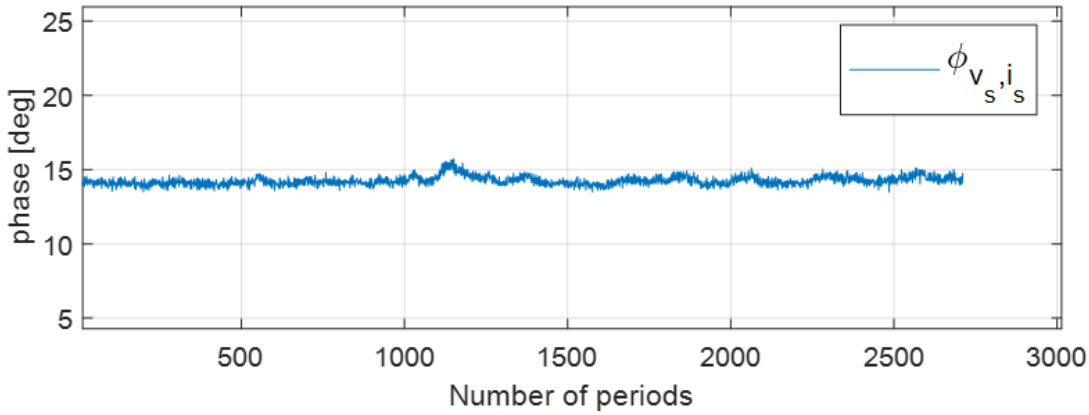

Fig. 5.16. Experimental rectifier input phase showing the synchronization at 40 W.

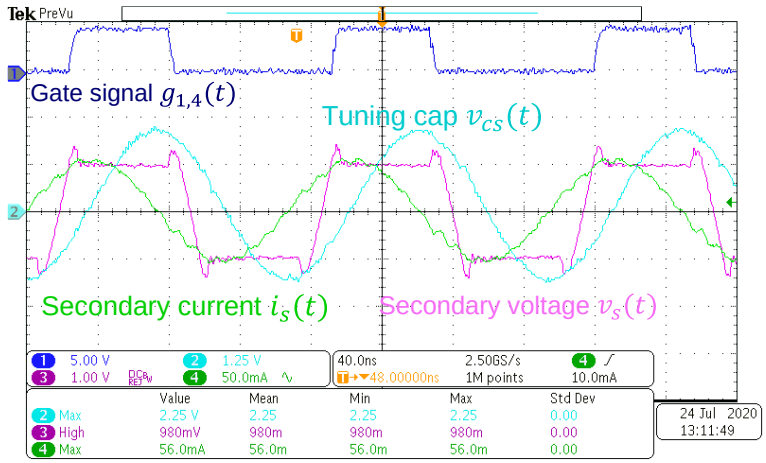

(a)

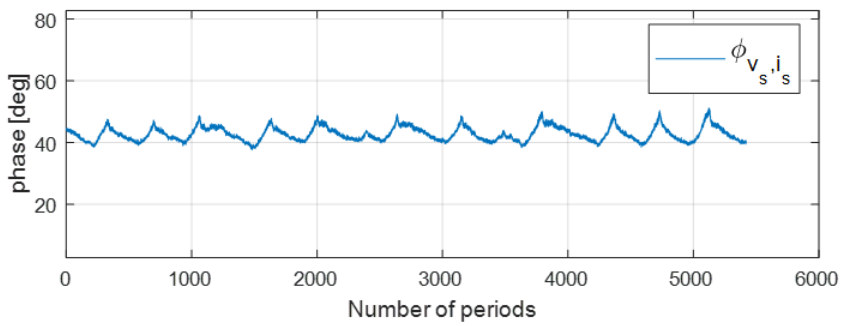

(b)

Fig. 5.17. Experimental closed-loop (a) operating waveforms and (b) rectifier input phase showing the synchronization at 0.02W.

input, resulting in the reduction of ϕ_{v_s,i_s} from the originally designed value, 15°. Once V_{Gc} reaches 3 V, the microcontroller toggles the GPIO pin from high to low ($S_{MSP} = 0$) and ADC_{offset} is again decreased from 700 to 529. In contrast to the previous configuration, i_{os} is now withdrawn from the compensator input, increasing ϕ_{v_s,i_s} from the originally designed value The measured and analytical ϕ_{v_s,i_s}values at each testing point are plotted in Fig. 5.18.

Although there is a discrepancy as ϕ_{v_s,i_s} is shifted further away from 15°, the analytical model tracks well the trend of ϕ_{v_s,i_s} over the entire range of ADC_{offset}. For each selected R_{os}, there are approximately 344 controllable ϕ_{v_s,i_s} values, corresponding to 344 ADC_{offset} points, which confirms the high-resolution control approach. In this experiment, ϕ_{v_s,i_s} spans a wide range from 0° to 26°, which can be increased further by selecting a smaller R_{os}. In another experiment, this testing process is repeated with various R_{os} values to validate the controllability of the ϕ_{v_s,i_s} range by using R_{os}. The measured and analytical ϕ_{v_s,i_s} ranges are plotted over R_{os} values in Fig. 5.19.

These experimental results prove that the control range of ϕ_{v_s,i_s} can be modified by using different R_{os} values, and they are inversely proportional. For instance, when R_{os} is equal to 5 kΩ, ϕ_{v_s,i_s} can be controlled from -25° to 40°. Therefore, the designed rectifier is validated to have the dynamic impedance regulation capability for wide loading conditions.

5.6 Summary

An open-loop setup of the entire WPT system is used to carry out experiments used to validate the power stage design and power loss model. In order to synchronize the

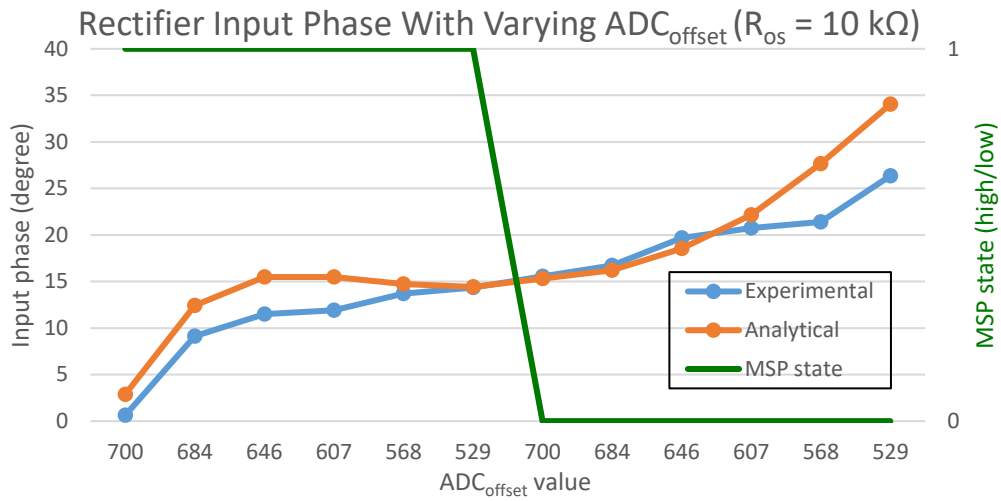

Fig. 5.18. Comparison of the experimental and analytical ϕ_{v_s,i_s} in the phase control.

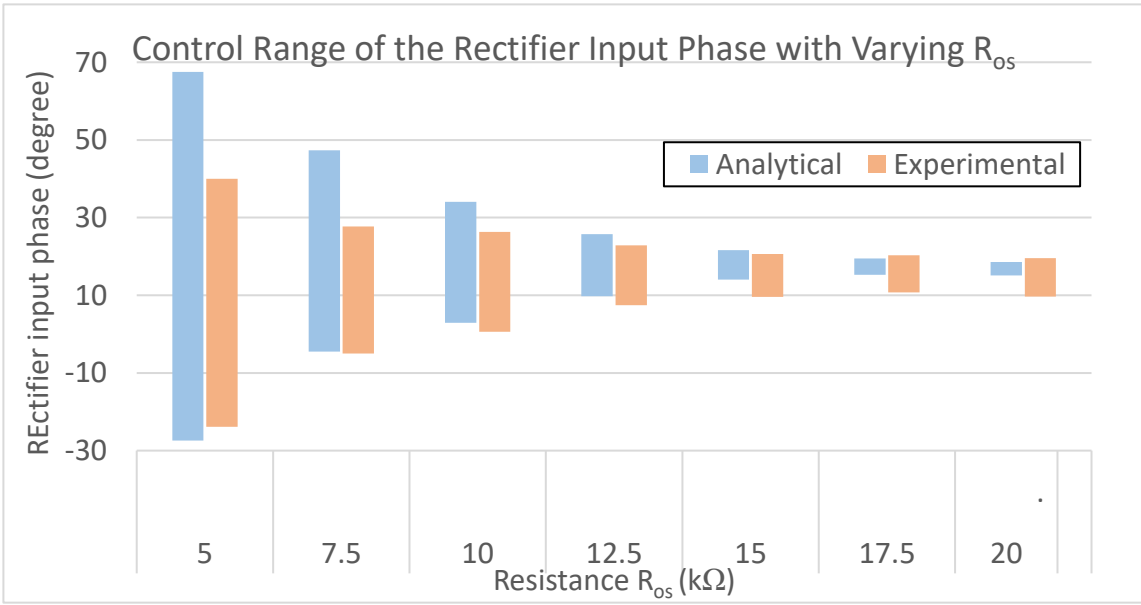

Fig. 5.19. Control range of ϕ_{v_s,i_s} with different R_{os} values.

rectifier during open-loop operation, an FPGA is employed to output synchronous PWM signals driving both the inverter and rectifier. Due to the difficulty in measuring the input ac power at high frequency, the end-to-end efficiency is evaluated by taking accurate measurements of the dc power. By comparing measured and modeled power loss of the entire system, the low-loss power stage design of the rectifier is validated. The system efficiency is also compared to that of a diode rectifier to demonstrate its benefit in reducing the loss.

In closed-loop experiments, the designed control system is used to synchronize the rectifier switching actions without bulky additional sensing hardware or communication channels. In steady-state, the experimental data show the stable rectifier input phase at the expected value of 15° with a low jittering of 0.3° (RMS). The rectifier is synchronized even at a low output power of 0.02W, confirming the robustness of the synchronization design. Also, the proposed control can dynamically adjust the rectifier input phase, enabling the dynamic impedance matching capability of the rectifier over a wide range of loading conditions.

Chapter Six

CONCLUSIONS AND FUTURE WORK

6.1 Conclusions

6.1.1 Wireless Power Receiving Unit for AA-Battery-Powered Devices

Motivated by the lack of WPT adoption in low power consumer electronics, especially the ones powered by standard AA batteries, a compact wireless AAPRU prototype is developed. This PRU is designed in a form factor of standard AA batteries so that it can be used to replace them and power existing household electronic devices. The AAPRU prototype is composed of four main components: 1) receiving coils, 2) power management circuit, 3) EMI shield, and 4) inner and outer housings. The AAPRU is intended to be placed flat on the surface and rotated around its longitudinal due to the cylindrical shape. If a single coil is used, there would be 2 angles where the induced voltage is zero. Thus, receiving coils are constructed in the dual-coil structure, where two identical rectangular coils are perpendicular to each other and share the same longitudinal axis. This configuration ensures the non-zero induced voltage at any rotational angle. The multiphase voltage-doubler diode rectifier is modeled with the parasitic diode capacitance taken into account since its reactive load is not negligible at 6.78 MHz. The accuracy of the analysis is validated by comparing modeled waveforms with experimental waveforms. Inner and outer housings used to protect inner components and support the overall shape are 3D printed. Finally, a flexible ferrite sheet is employed to redirect the magnetic flux to pass through receiving coils without penetrating the PCB. The experimental data show a fully

functional prototype that can be used to replace AA batteries and power existing consumer electronics.

6.1.2 Frequency Synchronous Active Rectifier

In resonant WPT systems, the impedance mismatch occurs and degrades the overall efficiency due to varying coil coupling and variable load. The impedance control technique utilizing the phase angle of the active rectifier is investigated. According to the literature, the PLL-based synchronization controller is robust but has never been used for high-frequency active rectifiers. Therefore, the impedance matching approach using the active rectifier with the dynamic impedance-regulation controller utilizing PLL techniques is investigated. Also, the analytical model for the synchronization loop dynamics is improved in term of accuracy.

6.1.2.1 Receiving Coil and Metal Housing

Since the PRU is required to be integrated inside existing consumer electronics, the metal housing of some devices introduces a challenge in the PRU design. A window is cut at the center of the housing to allow the magnetic flux to bypass the housing and flow through the coil enclosed area. However, this approach does not sufficiently mitigate the destructive effect of eddy currents on the desired magnetic flux. An approach addressing this issue is investigated: a small slot running from the central window to the outer edge is cut out of the metal housing. Validated by the simulation, this technique not only alleviates the detrimental phenomenon from the eddy current but also increases the coil coupling by changing the eddy current direction.

6.1.2.2 Power Stage Model and Design

The active rectifier is designed to achieve ZVS to reduce the switching loss which is proportional to f_s. A resonant tank including a hand-made toroidal inductor L_r is utilized to assist with ZVS achievement. Operating waveforms of the rectifier are modeled using a time-varying state-space description. The parasitic elements of various power transistors and passive components such as inductor ac resistance and drain-to-source capacitance are incorporated in the model to improve modeling accuracy. In addition, the resonant interval is also modeled. For the optimization process, the GaN device and L_r are sweeping parameters. The steady-state operating point of the rectifier is acquired using discrete-time state-space techniques. The efficiency at each operating point is calculated to facilitate the component selection process and find the optimal operating condition yielding the highest efficiency. As a result, the EPC2007C GaN FET and 2 μH L_r are chosen as optimal components.

The PCB layout is designed to minimize parasitic elements and ensure the symmetry in operating waveforms. Experimental waveforms exhibit minimal ringing and overshot. In order to validate the power stage design, the end-to-end efficiency of the entire open-loop WPT system is measured and compared to the analytical value. Also, the power loss of the WPT system using a diode rectifier at similar operating conditions is measured to showcase the benefit of the active rectifier in increasing efficiency. Based on the comparison, it is seen that the power loss model accurately predicts the loss reduction of 1.75 W due to the active rectifier. Thus, the high modeling accuracy and low-loss power stage design are verified.

6.1.2.3 Synchronization Control

The phase-locked loops (PLL) technique is employed to synchronize the rectifier operation to the WPT field. The synchronization control is accomplished using commercial components, including a low-cost microcontroller. The secondary-side tuning capacitor voltage v_{cs} is sensed as the reference signal for the synchronization control. v_{cs} is generally 90° of out phase with rectifier switching actions, resulting in high immunity to switching noise. The synchronized feedback signal from the control is also used to drive rectifier switching actions, completing the synchronization loop.

However, any sensed signal on the receiver is dependent on both transmitter and receiver operation, creating inherent feedback from the power stage to the sensed signal v_{cs}. This feedback is analyzed when designing synchronization control. The model developed in this work accounts for the transient time and reverse conduction of GaN devices in the ZVS operation. Based on the analyzed control loop gain, an analog compensator is designed to increase the bandwidth to 10 kHz for a faster response and maintain a phase margin of 45° for stabilization. Experimental results in closed-loop show the stable synchronization control in a full range of output power, from 0.02 W to 40 W.

To compensate for a wide range of loading conditions, an input phase control scheme is utilized to enable the dynamic impedance matching capability. It employs an external resistor connected between the compensator input and microcontroller's GPIO pin to inject or withdraw an amount of current i_{os}. A digital variable is added to the control algorithm to regulate the steady-state value of the compensator voltage level, which effectively changes i_{os}. Then the synchronization control automatically adjusts the rectifier

input phase to compensate for i_{os}. As a result, the equivalent load impedance is controlled dynamically by changing ADC_{offset} values. Experimental data validate the feasibility, wide range, and high resolution of the proposed control scheme. Therefore, the designed synchronous active rectifier is highly efficient in terms of reducing loss and compensating for wide loading conditions by dynamically changing its input phase.

6.2 Future Work

During the process of completing this thesis, further research directions have been identified to improve the current design.

As mentioned in the literature review, the rectified voltage V_{rec} along with ϕ_{v_s,i_s} is used to control X_{rec} and R_{rec} separately. V_{rec} can be controlled by adjusting the duty cycle of either the active rectifier or the voltage regulator at the output [20]. In the current design, the duty cycle of the rectifier is set by an external resistor connected to the gate driver and stays fixed during the entire operation. Another control scheme is required to adjust the rectifier duty cycle dynamically, improving the impedance matching ability of the rectifier. This additional control scheme will be investigated further in the next project.

After the power stage design and control of the synchronous active rectifier are validated through experiments, the last step is to integrate it into existing consumer electronics. The final version of the PCB without test points must be designed to fit in those devices. For laptops with metal housing, the approach mentioned in Section 4.1 is utilized to ensure the strong coupling between coils. For monitors, since the base generally has enough space for receiving coil, the receiver has to be placed in the monitor body, far away

from the receiving coil. A long wire required to connect them might have large parasitic elements that must be taken into account when designing the tuning network.

LIST OF REFERENCES

[1] X. Lu, P. Wang, D. Niyato, D. I. Kim, and Z. Han, "Wireless Charging Technologies: Fundamentals, Standards, and Network Applications," *IEEE Communications Surveys & Tutorials,* vol. 18, no. 2, pp. 1413-1452, 2016.

[2] H. Hu and S. V. Georgakopoulos, "Wireless power transfer in human tissue via Conformal Strongly Coupled Magnetic Resonance," in *IEEE Wireless Power Transfer Conference (WPTC),* 2015, pp. 1-4.

[3] T. Akin, K. Najafi, and R. M. Bradley, "A wireless implantable multichannel digital neural recording system for a micromachined sieve electrode," *IEEE Journal of Solid-State Circuits,* vol. 33, no. 1, pp. 109-118, 1998.

[4] A. P. Sample, D. T. Meyer, and J. R. Smith, "Analysis, Experimental Results, and Range Adaptation of Magnetically Coupled Resonators for Wireless Power Transfer," *IEEE Transactions on Industrial Electronics,* vol. 58, no. 2, pp. 544-554, 2011.

[5] N. Derrick Wing Kwan, Q. D. Trung, Z. Caijun, and S. Robert, "The Era of Wireless Information and Power Transfer," in *Wireless Information and Power Transfer: Theory and Practice*: Wiley, 2019, pp. 1-16.

[6] S. M. R. C. P. Ltd, "Wireless Power Transmission - Global Market Outlook (2018-2027)," Report 01/2020 2020. Research and Markets

[7] X. Lu, P. Wang, D. Niyato, D. I. Kim, and Z. Han, "Wireless Networks With RF Energy Harvesting: A Contemporary Survey," *IEEE Communications Surveys & Tutorials,* vol. 17, no. 2, pp. 757-789, 2015.

[8] "Introudction to the Power Class 0 Specification," Accessed on: June 2020Available: https://www.wirelesspowerconsortium.com/

[9] S. Y. R. Hui, "Magnetic Resonance for Wireless Power Transfer [A Look Back]," *IEEE Power Electronics Magazine*, vol. 3, no. 1, pp. 14-31, 2016.

[10] K. Sealy. (July 28). *Frequency Choice*. Available: https://airfuel.org/blog/frequency-choice/

[11] J. Li and D. Costinett, "Comprehensive Design for 6.78 MHz Wireless Power Transfer Systems," in *IEEE Energy Conversion Congress and Exposition (ECCE)*, 2018, pp. 906-913.

[12] Y. Akuzawa, K. Tsuji, H. Matsumori, Y. Ito, T. Ezoe, and K. Sakai, "A 95% efficient inverter with 300-W power output for 6.78-MHz magnetic resonant wireless power transfer system," in *IEEE MTT-S International Microwave Symposium*, 2015, pp. 1-3.

[13] M. R. Basar, M. Y. Ahmad, F. Ibrahim, and J. Cho, "Resonant inductive power transfer system for freely moving capsule endoscope with highly uniform magnetic field," in *IEEE Industrial Electronics and Applications Conference (IEACon)*, 2016, pp. 393-397.

[14] H. Kim *et al.*, "Coil Design and Measurements of Automotive Magnetic Resonant Wireless Charging System for High-Efficiency and Low Magnetic Field Leakage," *IEEE Transactions on Microwave Theory and Techniques*, vol. 64, no. 2, pp. 383-400, 2016.

[15] M. Fu, H. Yin, M. Liu, Y. Wang, and C. Ma, "A 6.78 MHz Multiple-Receiver Wireless Power Transfer System With Constant Output Voltage and Optimum Efficiency," *IEEE Transactions on Power Electronics,* vol. 33, no. 6, pp. 5330-5340, 2018.

[16] H. Yin, M. Fu, M. Liu, J. Song, and C. Ma, "Autonomous Power Control in a Reconfigurable 6.78-MHz Multiple-Receiver Wireless Charging System," *IEEE Transactions on Industrial Electronics,* vol. 65, no. 8, pp. 6177-6187, 2018.

[17] *A4WP Wireless Power Transfer System Baseline System Specification (BSS),* vv 1.3, 2014.

[18] L. Jiang and D. Costinett, "A GaN-Based 6.78 MHz Single-Stage Transmitter with Constant Output Current for Wireless Power Transfer," in *IEEE PELS Workshop on Emerging Technologies: Wireless Power Transfer (Wow),* 2018, pp. 1-6.

[19] T. C. Beh, M. Kato, T. Imura, S. Oh, and Y. Hori, "Automated Impedance Matching System for Robust Wireless Power Transfer via Magnetic Resonance Coupling," *IEEE Transactions on Industrial Electronics,* vol. 60, no. 9, pp. 3689-3698, 2013.

[20] A. Berger, M. Agostinelli, S. Vesti, J. A. Oliver, J. A. Cobos, and M. Huemer, "A Wireless Charging System Applying Phase-Shift and Amplitude Control to Maximize Efficiency and Extractable Power," *IEEE Transactions on Power Electronics,* vol. 30, no. 11, pp. 6338-6348, 2015.

[21] W. X. Zhong and S. Y. R. Hui, "Maximum Energy Efficiency Tracking for Wireless Power Transfer Systems," *IEEE Transactions on Power Electronics,* vol. 30, no. 7, pp. 4025-4034, 2015.

[22] E. Bou, R. Sedwick, and E. Alarcon, "Maximizing efficiency through impedance matching from a circuit-centric model of non-radiative resonant wireless power transfer," in *IEEE International Symposium on Circuits and Systems (ISCAS)*, 2013, pp. 29-32.

[23] Y. Lim, H. Tang, S. Lim, and J. Park, "An Adaptive Impedance-Matching Network Based on a Novel Capacitor Matrix for Wireless Power Transfer," *IEEE Transactions on Power Electronics*, vol. 29, no. 8, pp. 4403-4413, 2014.

[24] S. Y. R. Hui, W. Zhong, and C. K. Lee, "A Critical Review of Recent Progress in Mid-Range Wireless Power Transfer," *IEEE Transactions on Power Electronics*, vol. 29, no. 9, pp. 4500-4511, 2014.

[25] M. Chen and G. A. Rincon-Mora, "Accurate, Compact, and Power-Efficient Li-Ion Battery Charger Circuit," *IEEE Transactions on Circuits and Systems II: Express Briefs*, vol. 53, no. 11, pp. 1180-1184, 2006.

[26] H. Qiu, Y. Narusue, Y. Kawahara, T. Sakurai, and M. Takamiya, "Digital Coil: Transmitter Coil with Programmable Radius for Wireless Powering Robust Against Distance Variation," in *IEEE Wireless Power Transfer Conference (WPTC)*, 2018, pp. 1-4.

[27] N. Y. Kim, K. Y. Kim, J. Choi, and C. Kim, "Adaptive frequency with power-level tracking system for efficient magnetic resonance wireless power transfer," *Electronics Letters*, vol. 48, no. 8, pp. 452-454, 2012.

[28] J. Park, Y. Tak, Y. Kim, Y. Kim, and S. Nam, "Investigation of Adaptive Matching Methods for Near-Field Wireless Power Transfer," *IEEE Transactions on Antennas and Propagation,* vol. 59, no. 5, pp. 1769-1773, 2011.

[29] F. Wenzhen, Z. Bo, and Q. Dongyuan, "Study on frequency-tracking wireless power transfer system by resonant coupling," in *IEEE 6th International Power Electronics and Motion Control Conference*, 2009, pp. 2658-2663.

[30] J. Kim, D. Kim, and Y. Park, "Analysis of Capacitive Impedance Matching Networks for Simultaneous Wireless Power Transfer to Multiple Devices," *IEEE Transactions on Industrial Electronics,* vol. 62, no. 5, pp. 2807-2813, 2015.

[31] J. Liu, Y. Zhao, C. Xu, and X. Wang, "One-side automated discrete impedance matching scheme for wireless power transmission," in *IEEE Wireless Power Transfer Conference (WPTC)*, 2017, pp. 1-4.

[32] S. Cochran and D. Costinett, "Modeling a 6.78 MHz synchronous WPT rectifier with reduced THD," in *IEEE 18th Workshop on Control and Modeling for Power Electronics (COMPEL)*, 2017, pp. 1-8.

[33] S. Cochran and D. Costinett, "Frequency Synchronization and Control for a 6.78 MHz WPT Active Rectifier," in *IEEE 19th Workshop on Control and Modeling for Power Electronics (COMPEL)*, 2018, pp. 1-7.

[34] C. Zhao, Z. Wang, J. Du, J. Wu, S. Zong, and X. He, "Active resonance wireless power transfer system using phase shift control strategy," in *IEEE Applied Power Electronics Conference and Exposition - APEC*, 2014, pp. 1336-1341.

[35] R. Mai, Y. Liu, Y. Li, P. Yue, G. Cao, and Z. He, "An Active-Rectifier-Based Maximum Efficiency Tracking Method Using an Additional Measurement Coil for Wireless Power Transfer," *IEEE Transactions on Power Electronics*, vol. 33, no. 1, pp. 716-728, 2018.

[36] Z. Rui, D. T. Gladwin, and D. A. Stone, "Phase shift control based Maximum Efficiency Point Tracking in resonant wireless power system and its realization," in *IECON 2016 - 42nd Annual Conference of the IEEE Industrial Electronics Society*, 2016, pp. 4541-4546.

[37] D. J. Thrimawithana, U. K. Madawala, and M. Neath, "A Synchronization Technique for Bidirectional IPT Systems," *IEEE Transactions on Industrial Electronics*, vol. 60, no. 1, pp. 301-309, 2013.

[38] X. Liu, N. Jin, D. Ma, and X. Yang, "A Simple and Effective Synchronization Technique for Wireless Power Transfer System," in *IEEE Wireless Power Transfer Conference (WPTC)*, 2018, pp. 1-4.

[39] S. Cochran and D. Costinett, "Discrete Time Synchronization Modeling for Active Rectifiers in Wireless Power Transfer Systems," in *20th Workshop on Control and Modeling for Power Electronics (COMPEL)*, 2019, pp. 1-8.

[40] H. F. Lund, *The McGraw-hill recycling handbook*. McGraw-Hill, Incorporated, 1993.

[41] A. Bernardes, D. C. R. Espinosa, and J. S. J. J. o. P. S. Tenório, "Recycling of batteries: a review of current processes and technologies," vol. 130, no. 1-2, pp. 291-298, 2004.

[42] N. Owano. (2018, July). *Forever Battery a compelling talking point at CES*. Available: https://techxplore.com/news/2018-01-battery-compelling-ces.html

[43] J. M. H. Lee, S. C. L. Yuen, W. J. Li, and P. H. W. Leong, "Development of an AA size energy transducer with micro resonators," in *2003 IEEE International Symposium on Circuits and Systems (ISCAS)*, 2003, vol. 4, pp. IV-IV.

[44] *College Physics Textbook Equity Edition*. Openstax College, 2016, pp. p811-p835.

[45] N. Ugle, T. K. Bhuiya, R. Dapkar, D. M. Shinde, and S. Bagchi, "Design and Comparison of Rectangular, Square and Hexagonal RF Coils For 1.5T MRI System," in *9th International Conference on Computing, Communication and Networking Technologies (ICCCNT)*, 2018, pp. 1-4.

[46] G. Grandi, M. K. Kazimierczuk, A. Massarini, and U. Reggiani, "Stray capacitances of single-layer solenoid air-core inductors," *IEEE Transactions on Industry Applications*, vol. 35, no. 5, pp. 1162-1168, 1999.

[47] W. C. Johnson, "Transmission lines and networks," p. 58, 1950.

[48] P. Dowell, "Effects of eddy currents in transformer windings," in *Proceedings of the Institution of Electrical Engineers*, 1966, vol. 113, no. 8, pp. 1387-1394: IET.

[49] A. Eroglu, "Complete Modeling of Toroidal Inductors for High Power RF Applications," *IEEE Transactions on Magnetics*, vol. 48, no. 11, pp. 4526-4529, 2012.

[50] T. Ibuchi and T. Funaki, "Validation of the air-core inductor copper loss model for high-frequency power conversion applications," in *International Symposium on Electromagnetic Compatibility*, 2013, pp. 561-566.

[51] M. Fu, T. Zefan, M. Liu, C. Ma, and X. Zhu, "Full-bridge rectifier input reactance compensation in Megahertz wireless power transfer systems," in *IEEE PELS Workshop on Emerging Technologies: Wireless Power (2015 WoW)*, 2015, pp. 1-5.

[52] J. Li, "Wireless Power System Design for Maximum Efficiency," Master, University of Tennessee, 2018.

[53] S. Yang, J. Narayan, J. Rosenfeld, K. Stevens, and P. Chewning, "Chassis Design for Wireless-Charging Coil Integration for Computing Systems," ed: Google Patents, 2016.

[54] *PLECS The Simulation Platform for Power Electronic Systems*. Available: https://www.plexim.com/plecs

[55] D. Costinett, R. Zane, and D. Maksimovic, "Discrete time modeling of output disturbances in the dual active bridge converter," in *IEEE Applied Power Electronics Conference and Exposition - APEC*, 2014, pp. 1171-1177.

[56] "T44-17 datasheet," in *Iron Powder Cores*, ed: Micrometals, 2019.

[57] Y. Jiang *et al.*, "A Novel Synchronization Technique for High Frequency Rectifier in Wireless Power Transfer," in *10th International Conference on Power Electronics and ECCE Asia (ICPE 2019 - ECCE Asia)*, 2019, pp. 974-978.

[58] J. G. Kassakian, M. F. Schlecht, and G. C. Verghese, *Principles of power electronics*. Graphis, 2000, pp. 300-360.

[59] "EPC2007C – Enhancement Mode Power Transistor," ed: EPC, August, 2019.

[60] "LMG1210 200-V, 1.5-A, 3-A half-bridge MOSFET and GaN FET driver with adjustable dead time for applications up to 50 MHz," ed: Texas Instrument, November, 2018

[61] S. P. Cochran, "A GaN-Based Synchronous Rectifier with Reduced Voltage Distortion for 6.78 MHz Wireless Power Applications," Master's Thesis, University of Tennessee, 2017.

[62] "Phase Detector/Frequency Synthesizer ADF4002 Datasheet," ed: Analog Devices.

[63] "MSP430F51x2, MSP430F51x1 Mixed-Signal Microcontrollers," ed: Texas Instruments, August, 2010.

[64] "LTC6903/LTC6904 datasheet," ed: Linear Technology, March, 2012.

VITA

Phuc Tran Hoang Pham goes by Peter Pham. He was born and raised in Vietnam. He moved to the U.S. and continued his study as a senior student in high school. He enrolled in a community college in Washington State for two years, then transferred to the University of Tennessee to get his Bachelor's degree in electrical engineering. During his undergraduate studies, he received multiple scholarships, won several academic competitions, and actively involved with the research center, CURENT, for electrical engineering students. He graduated summa cum laude with a 4.0 GPA in 2018 with the "top graduate" award.

Continuing his Master's program at the University of Tennessee, Peter works under two great power electronics professors, Dr. Leon Tolbert and Dr. Daniel Costinett. During his graduate studies, he was nominated and became a leader for the lab committee at CURENT. He also received several awards for his leadership skills. For his research project, he has been focusing on designing high-frequency WPT applications using wide bandgap devices.